THESIS FOR THE DEGREE OF DOCTOR OF PHILOSOPHY

Dynamical properties of metal halide and oxyhydride perovskites

Insights from inelastic neutron scattering

RASMUS LAVÉN

Department of Chemistry and Chemical Engineering
CHALMERS UNIVERSITY OF TECHNOLOGY
Gothenburg, Sweden 2023

Dynamical properties of metal halide and oxyhydride perovskites
Insights from inelastic neutron scattering
RASMUS LAVÉN
ISBN 978-91-7905-853-1

Doktorsavhandlingar vid Chalmers tekniska högskola
Ny serie nr 5319
ISSN 0346-718X

Department of Chemistry and Chemical Engineering
Chalmers University of Technology
SE-412 96 Gothenburg
Sweden
Telephone: +46 (0)31-772 1000

Cover:
Imaginary part of the dynamic susceptibility measured using inelastic neutron scattering on a powder sample of $CH_3NH_3PbI_3$ in the orthorhombic (100 K) and tetragonal (170 K) phases. The bottom panel illustrates the crystal structures for these two phases.

Chalmers Digitaltryck
Gothenburg, Sweden 2023

Dynamical properties of metal halide and oxyhydride perovskites
Insights from inelastic neutron scattering

Rasmus Lavén
Department of Chemistry and Chemical Engineering
Chalmers University of Technology

Abstract

This thesis concerns investigations of the dynamical properties of two classes of energy-relevant materials, namely metal halide and oxyhydride perovskites, using neutron scattering techniques. These two classes of materials share the same aspect of a perovskite-type crystal structure but are different in terms of their functional properties and concomitant promise for various technological applications.
Regarding the metal halide perovskites, these materials are of large interest for use in, *e.g.*, next-generation solar cells and light-emitting diodes. In this thesis, the studies on these types of materials focused on elucidating the nature of organic cation and lattice dynamics in the hybrid organic-inorganic systems $FA_{1-x}MA_xPbI_3$ (MA = methylammonium and FA = formamidinium), BA_2PbI_4 and PEA_2PbI_4 (BA = butylammonium and PEA = phenethylammonium), and the all-inorganic perovskite $CsPbI_3$, by using a wide variety of quasielastic and inelastic neutron scattering techniques. For $FA_{1-x}MA_xPbI_3$, a key result is that MA-doping of $FAPbI_3$ leads to significantly different cation dynamics, which is directly related to the stabilization of the perovskite crystal structure. Overall, the results showcase the importance of organic cation and lattice dynamics and the couplings between these types of dynamics in this class of materials and highlight the importance of dynamics for an understanding of the properties of metal halide perovskites.
Regarding the oxyhydride perovskites, these materials are of interest because of their hydride ion conductivity. Here, the studies focused on elucidating the dynamical properties of hydride ions in the perovskite materials $SrVO_2H$ and $BaTiO_{3-x}H_y$, using quasielastic neutron scattering techniques. For $SrVO_2H$, the results showed the presence of a correlated jump diffusion mechanism, with an enhanced jump rate for backward jumps, which slows down the long-range diffusion, and localizes hydride ions in the vicinity of a particular vacancy. For $BaTiO_{3-x}H_y$, a faster diffusion process was observed, which can be explained by the relatively larger amount of anion vacancies in this material, which promotes diffusion. The vibrational dynamics of hydride ions were further studied in $SrVO_2H$. Interestingly, it was found that the V−H and V−O-based phonons are largely influenced by the antiferromagnetic ordering of the material. These results showcase the important couplings between the magnetism and vibrational dynamics which can occur in magnetic oxyhydrides.

Keywords: Metal halide perovskite, oxyhydride, perovskite, quasielastic neutron scattering, inelastic neutron scattering, diffusion, phonon, hydrogen dynamics, hydride ion.

List of papers

This thesis is based on the work contained in the following papers:

Paper I. **Rotational Dynamics of Organic Cations in Formamidinium Lead Iodide Perovskites**
R. Lavén, M.M. Koza, L. Malavasi, A. Perrichon, M. Appel, and M. Karlsson
The Journal of Physical Chemistry Letters **14** 2784–2791 (2023)

Paper II. **Cation Dynamics and Structural Stabilization in Formamidinium Lead Iodide Perovskites**
K. Druzbicki, R. Lavén, J. Armstrong, L. Malavasi, F. Fernandez-Alonso, and M. Karlsson
The Journal of Physical Chemistry Letters **12** 3503-3508 (2021)

Paper III. **Temperature-response of the vibrational dynamics in hybrid lead iodide perovskites**
R. Lavén, M. M. Koza, L. Malavasi and M. Karlsson
In Manuscript

Paper IV. **Vibrational properties of $CsPbI_3$: from harmonic phonons to overdamped relaxations**
R. Lavén, E. Fransson, P. Erhart, G.E. Granroth, F. Juranyi, and M. Karlsson
In Manuscript

Paper V. **Organic Cation Dynamics in the Layered Lead Iodide Perovskites BA_2PbI_4 and PEA_2PbI_4 probed by Quasielastic Neutron Scattering**
R. Lavén, M.M. Koza, N.H. Jalarvo, L. Malavasi, and M. Karlsson
In Manuscript

Paper VI. **Vibrational properties of the layered halide perovskites butylammonium and phenethylammonium lead iodide**
R. Lavén, M.M. Koza, M.R. Jimenez, L. Malavasi, and M. Karlsson
In Manuscript

Paper VII. **Diffusional Dynamics of Hydride Ions in the Layered Oxyhydride $SrVO_2H$**
R. Lavén, U. Häussermann, A. Perrichon, M.S. Andersson, M. Sannemo Targama, F. Demmel, and M. Karlsson
Chemistry of Materials **33** 2967-2975 (2021)

Paper VIII. **Vibrational properties of $SrVO_2H$ with large spin-phonon coupling**
R. Lavén, P.I.R. Moraes, M. Sannemo Targama, M. Karlsson, A.A. Leitão, P.H.B. Brant Carvalho, S.F. Parker, U. Häussermann, and O.Y Vekilova
Physical Review Materials **6**, 024409 (2022)

Paper IX. **Hydride diffusion in oxyhydride barium titanate: insights from incoherent quasielastic neutron scattering**
R. Lavén, H. Guo, U. Häussermann, M. Matsuura, and M. Karlsson
In Manuscript

Contribution report

My contributions to the included papers:

I I was the main responsible for the data collection and analysis of the experimental data. I was the main responsible for writing the paper.

II I was the main responsible for the experimental data collection and analysis of the experimental data. I was the main responsible for writing the experimental parts of the paper.

III I was the main responsible for the data collection and analysis of the experimental data. I was the main responsible for writing the paper.

IV I was the main responsible for the data collection and analysis of the experimental data. I was the main responsible for writing the paper.

V I was the main responsible for the data collection and analysis of the experimental data. I was the main responsible for writing the paper.

VI I was the main responsible for the data collection and analysis of the experimental data. I was the main responsible for writing the paper.

VII I was the main responsible for the data collection and analysis of the neutron scattering data. I was the main responsible for writing the paper.

VIII I was the main responsible for data collection and analysis of the experimental data.

IX I was the main responsible for the data collection and analysis of the neutron scattering data. I was the main responsible for writing the paper.

Contents

List of Acronyms

AFM	Antiferromagnetic
BA	Butylammonium
DFT	Density functional theory
DHO	Damped Harmonic Oscillator
DOS	Density of states
FA	Formamidinium
FWHM	Full width at half maximum
GDOS	Generalized density of states
HOIP	Hybrid organic inorganic perovskite
HWHM	Half width at half maximum
ILL	Institut Laue-Langevin
INS	Inelastic neutron scattering
MA	Methylammonium
MHP	Metal halide perovskite
NPD	Neutron powder diffraction
PEA	Phenethylammonium
PSI	Paul Scherrer Institute
QENS	Quasielastic neutron scattering
SNS	Spallation Neutron Source
TOF	Time-of-flight
vDOS	Vibrational density of states
XRD	X-ray diffraction

Chapter 1

Introduction

Understanding the fundamental relationships between a material's atomic structure and dynamics and its macroscopic properties is a foundation in both physics and chemistry and is also crucial for the rational development of new materials and devices. With respect to the current importance of developing new and optimising/improving present methods for energy conversion and electricity production, it is important to develop new materials which can be used in such energy conversion or storage devices and can improve or optimize their function. Generally, these materials can be classified under the term "energy materials", which simply means materials which show potential for use in some type of energy-relevant application. In order to continue the development of energy materials, it is important to understand, on the atomic scale level, the origin of their beneficial material properties. For crystalline materials, the most obvious and critical property to understand is the crystal structure. However, in many cases, it is not enough to understand just the crystal structure, but also the dynamics of atoms in the crystal structure are of critical importance. In this context, this thesis is focused on increasing the fundamental understanding of the atomic structure and, in particular, atomic dynamics of two classes of energy materials, namely metal halide perovskites (MHPs) and perovskite-type oxyhydrides. Specifically, it is focused on elucidating the dynamical properties such as vibrational dynamics (phonons) and ionic diffusion, which are of critical importance for several interesting and useful properties these materials display. Such properties include optoelectronic response for the MHPs and ionic diffusion for the oxyhydride perovskites, which are relevant for the development of new and environmentally friendly energy technologies.

1.1 Metal halide perovskites

MHPs have recently emerged as efficient materials for use in solar cells [1]. These materials are relatively old and have been known for over 40 years [2, 3], but their promise for energy conversion applications was only demonstrated within the recent 10-15 years [4, 5]. Compared to current technologies, which are mainly based on Si or

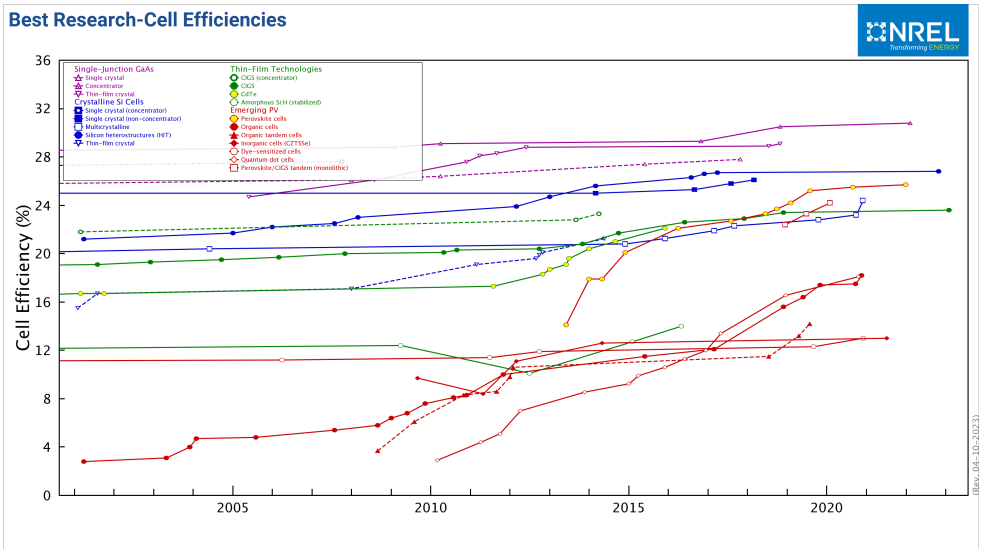

Figure 1.1: Illustration of the development of the power conversion efficiencies for solar cells based on various materials from 2000 to present. The solar cells based on MHPs are shown in yellow colour. Tandem and multi-junction solar cells are not shown in the plot. This plot is courtesy of the National Renewable Energy Laboratory, Golden, CO [8].

other common semiconductors, the main advantage of these MHPs is that they are cheaper and easier to produce. This is important because it could reduce the cost of large-scale solar photovoltaic power plants. Another important property of the MHPs is that they can be easily synthesized as thin films using, *e.g.*, spin-coating or vapour deposition techniques [6], and because of the long carrier diffusion lengths in MHPs [7], they can also operate as a thin film solar cell device.

Since the discovery of "perovskite solar cells" (solar cells based on MHPs), their power conversion efficiency has increased rapidly and is currently similar to the most commonly used Si solar cells, which is shown in Figure 1.1. Still, understanding the detailed structure-property relationships in MHPs is challenging and is, therefore, under ongoing research. The crystal structure of MHPs is based on the perovskite structure, with the general chemical formula ABX_3. Here, A is an organic cation (*e.g.* methylammonium, MA^+ or formamidinium, FA^+) or a large inorganic cation (*e.g.* Cs^+ or Rb^+), B is a divalent metal cation (*e.g.* Pb^{2+} or Sn^{2+}), and X is a halide anion (*e.g.* I^-, Br^-, or Cl^-). These materials exhibit useful optoelectronic properties, which make them suitable for use in photovoltaic devices; such material properties include, for instance, close to optimal electronic bandgap for efficient solar absorption (iodine compounds), long charge carrier diffusion lengths, and low electron-hole recombination rates [9–11]. In devices, the most efficient materials are based on chemically substituted

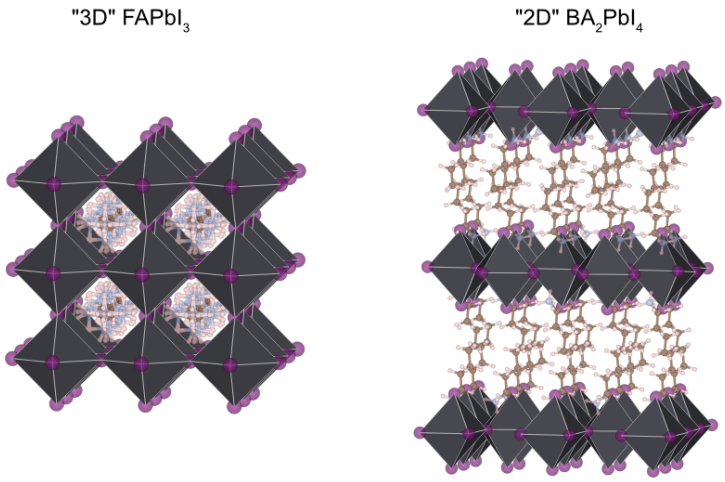

Figure 1.2: Illustration of the crystal structure of "3D" (left panel) and "2D" MHPs (right panel). The organic cation disorder is schematically illustrated as all atomic positions of FA from the symmetry equivalent sites from the O_h site symmetry are drawn. Colour code: I, purple; Pb, black; N, blue; C, brown; and H, pink. The figure was generated using the VESTA software [26].

solid solutions, such as $MA_{1-x-y}FA_xCs_yPbI_{3-z}Br_z$ [12]. Chemical substitutions on the A–site allows for improvement of the stability and performance of the material [13–15], whereas halogen substitutions allow tuning of the electronic bandgap over a broad range of energies [16, 17]. Besides such chemical substitutions, MHPs also exhibit a large degree of structural and dimensional variability. The A–site cage in the MHP structure limits the size of the organic cation to a large degree, but incorporating larger organic cations changes the connectivity and dimensionality of the resulting crystal structure, which is illustrated in Figure 1.2. For larger organic cations, this will create a layered crystal structure with sheets of corner-sharing BX_6 octahedra separated by large organic cations [18]. These layered (or often called two-dimensional (2D)) materials are based on the Ruddlesden-Popper crystal structure of general chemical formula R_2BX_4. The layered MHPs exhibit a larger exciton binding energy, shorter charge carrier lifetimes, and a larger electronic bandgap, which makes them unsuitable for use in photovoltaic devices, but attractive for other applications, such as in light-emitting diodes [19–23]. Furthermore, these layered materials exhibit higher stability compared to the 3D MHPs [18, 24, 25].

Apart from their structural tuneability and versatility, MHPs exhibit distinct characteristics related to their dynamical properties, which are not present in conventional inorganic semiconductors (like Si or GaAs). In hybrid organic-inorganic MHPs, the A-site organic cation is dynamically disordered for temperatures $\gtrsim 150$ K [27, 28]. In addition, the lead halide framework is made from relatively weak ionic bonding and

heavy elements, leading to low phonon energies and intrinsic dynamic disorder even for all-inorganic MHPs [29–32]. The remarkable optoelectronic properties of MHPs have been attributed to various phenomena, which have been discussed in literature [10]. One such phenomenon is the large dynamical fluctuations, which are caused by the intrinsic dynamic disorder of the "soft" lead halide framework and/or organic cation dynamics. These dynamic fluctuations have, *e.g.*, been hypothesized to induce large polaron formation and screening of charge carriers, resulting in defect tolerance, moderate charge carrier mobility, and low recombination properties [30, 33–35]. However, there is still a lack of complete understanding of these phenomena, and several of the proposed microscopic mechanisms require further experimental verification.

1.2 Oxyhydride perovskites

Perovskite-type oxyhydrides are an interesting class of mixed-anion compounds that typically are formed from transition metal oxides when the oxygen anions (O^{2-})are partly replaced by hydride ions (H^-). In similarity with the MHPs, most known transition metal oxyhydrides are based on the perovskite structure or perovskite-like structure, which are of specific concern in this thesis. Figure 1.3 shows, as an example, the crystal structure of $SrVO_3$ and its corresponding oxyhydride $SrVO_2H$, which is formed upon reacting $SrVO_3$ with CaH_2 at around 600 °C [36]. The introduction of hydride ions has been shown to affect several material properties, such as electronic [37] and magnetic [38] properties, and hydride ion conductivity [39–41]. The property of hydride-ion conductivity is of great interest from an application perspective, particularly in the development of new solid-state ionics technologies such as fuel cells and batteries based on oxyhydrides. Although several transition metal oxyhydrides are thought to exhibit hydride-ion conduction, little is known about the underlying atomic-scale diffusion mechanism, partly because of the lack of methods that can probe the sole transport of hydride-ions in a solid material. One particular difficulty with measuring the hydride-ion conductivity is the presence of simultaneous electronic conductivity in many known materials [42]. However, quasielastic neutron scattering (QENS) is a powerful technique for directly probing hydrogen diffusion in solids and has been used to observe hydride-ion diffusion in $LaSrCoO_3H_{0.7}$ [43] and in $BaTiO_{3-x}H_x$ [44]. Recently, pure hydride-ion conductivity was demonstrated in $La_{2-x-y}Sr_{x+y}LiH_{1-x+y}O_{3-y}$ [40]. However, the diffusion mechanism of hydride ions in oxyhydrides remains poorly understood, and the development of superior transport properties in new oxyhydride materials depends on a deeper understanding of this mechanism.

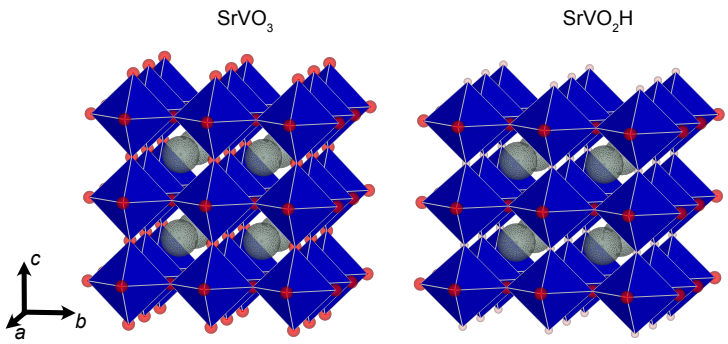

Figure 1.3: Illustration of the crystal structures of $SrVO_3$ (left panel) and $SrVO_2H$ (right panel) [36]. Colour code: Sr, grey; V, blue; O, red; and H, pink. The figure was generated using the VESTA software [26].

1.3 Aim of the thesis

This thesis aims to contribute with a new fundamental understanding of the local structure and dynamical properties and their correlations with the aforementioned important material properties of both MHPs and perovskite oxyhydrides. To this end, a variety of neutron spectroscopy techniques have been used in order to probe atomic correlations in both space and time. For the MHPs, the studies have focused on understanding the organic cation dynamics in the $FA_{1-x}MA_xPbI_3$ system, using both QENS and inelastic neutron scattering (INS) methods. It further reports results on the vibrational dynamics and its temperature dependence in the lead iodide perovskite systems $CsPbI_3$ and $FA_{1-x}MA_xPbI_3$. Lastly, in order to obtain an even more complete picture of organic cation dynamics in MHPs, the studies were extended to include the layered (2D) lead iodide perovskites butylammonium lead iodide (BA_2PbI_4) and phenethylammonium lead iodide (PEA_2PbI_4) – two of most well-studied layered MHPs, which also exhibit some distinct differences in their optoelectronic properties, thus making them good model systems for understanding the effect of organic cation dynamics on the optical and electronic material properties. For the transition metal oxyhydrides, the studies focused on the perovskite systems $SrVO_2H$ and $BaTiO_{3-x}H_y$, and QENS was used to directly measure and characterize the hydride-ion jump diffusion. For $SrVO_2H$, the vibrational spectrum was also fully characterized using INS and indicated an interesting coupling between the magnetic ordering and the phonons in the material.

The thesis is organized as follows. Chapter 2 and 3 introduce the background of MHPs and transition metal oxyhydrides, respectively. Chapter 4 describes the main methods used in this work, and Chapter 5 describes some key experimental considerations in neutron scattering. The major findings of this thesis are summarized

and discussed in Chapter 6, and Chapter 7 provides a conclusion and outlook for future studies.

Chapter 2

Metal halide perovskites

MHPs are under considerable scientific interest because of their useful and interesting optical and electronic properties, with potential applications in photovoltaic (PV) and light emitting devices [1, 22]. For application in solar cells, the most well-studied MHPs are methylammonium lead iodide ($MAPbI_3$, MA = $CH_3NH_3^+$) and formamidinium lead iodide ($FAPbI_3$, FA = $CH(NH_2)_2^+$). Both of these materials and their corresponding solid solutions $FA_{1-x}MA_xPbI_3$ exhibit electronic band gaps near optimal for achieving a high power conversion efficiency in a PV device ($\sim 1.4-1.55$ eV [45]). In addition to the close-to-optimal bandgap, these materials also exhibit several other beneficial properties for solar cells applications, such as long charge carrier lifetimes, low exciton binding energy, low recombination rates, and relatively high tolerance to defects [11]. The main factors limiting the use of these materials in real solar cell devices are their poor long-term stability towards humidity and heat [46, 47], and the toxicity of the lead [48]. However, given the rapidly increasing amount of discovered metal halide perovskites with useful optoelectronic properties, and the large chemical space left to explore, there are most likely many more compounds waiting to be discovered, hopefully with higher stability and without lead. A rational design of such materials is only possible when understanding how their atomic structure and dynamics give rise to their beneficial optoelectronic properties.

The layered lead iodide perovskites are featured by a layered crystal structure of sheets of corner-sharing PbI_6 octahedra separated by the larger organic cations, which is shown in Figure 2.1 (b). This layered structure also gives rise to distinct differences in the optoelectronic properties compared to the $A PbI_3$ perovskites, such as a larger electronic bandgap. This is shown in Figure 2.1 (c), which compares the optical absorption spectra of $MAPbI_3$ to that of the layered lead iodide perovskite BA_2PbI_4 (BA = butylammonium, $CH_3(CH_2)_3NH_3^+$). For $MAPbI_3$, the absorption shows a sharp onset around 1.5 eV, which corresponds to the bandgap. For BA_2PbI_4, there are, in addition, pre-edge peaks below the main absorption peak around 2.6 eV. Those pre-edge peaks correspond to exciton peaks [21] and appear for the layered materials because of their higher exciton binding energy. For $MAPbI_3$, no such exciton peaks

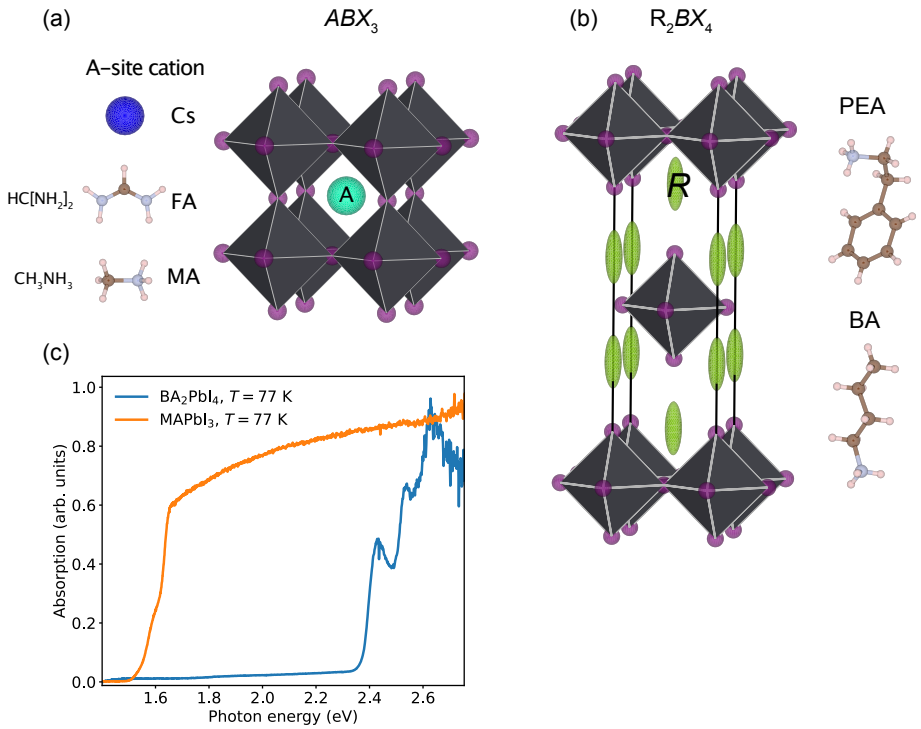

Figure 2.1: Illustration of the crystal structures of (a) 3D lead iodide perovskites and (b) 2D layered lead iodide perovskites. Colour code: I, purple; Pb, black; N, blue; C, brown; and H, pink. The organic cation spacers are illustrated as green ellipsoids in (b). (c) Comparison of the optical absorption spectra measured on powder samples of $MAPbI_3$ and BA_2PbI_4 at 77 K. The spectra have been vertically offset for easier comparison. The data was measured at Chalmers University of Technology.

can be distinguished in the data, which is due to the low exciton binding energy in $MAPbI_3$ [27].

2.1 Structural properties of $A\mathrm{PbI}_3$ perovskites

As mentioned before, MHPs are based on the versatile perovskite structure with the general chemical formula ABX_3. The ideal structure is a simple cubic form with space group $Pm\bar{3}m$, which is generally displayed at sufficiently high temperatures. However, this ideal cubic structure is rarely the ground state, and the perovskites generally display (several) symmetry-lowering phase transitions upon lowering the temperature. Figure 2.2 shows a typical phase behaviour of metal halide perovskites, *i.e.* a high-temperature cubic phase, an intermediate temperature tetragonal phase, and a low-temperature orthorhombic phase. In general, these different phases are

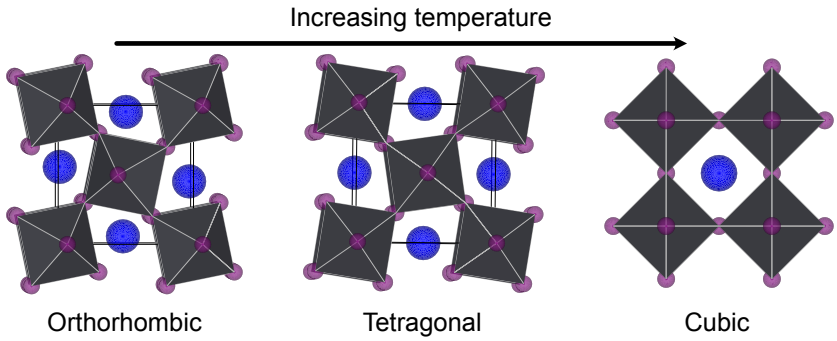

Figure 2.2: Illustration of cubic perovskite structure and typical phases of lower symmetry that often are formed at lower T, by tilting of the lead iodide octahedra. The A-site cation is illustrated as a blue sphere. The solid lines indicate a unit cell. The illustrated distorted phases are those formed by $\mathrm{CsPbI_3}$ [49]. The figure was generated using the VESTA software [26].

formed from the cubic phase by various tilting patterns of the $\mathrm{PbX_6}$ octahedra. However, the details of these phases depend on the detailed chemical composition of the material. In what follows, the structures of the lead iodide perovskites $\mathrm{MAPbI_3}$, $\mathrm{FAPbI_3}$, $\mathrm{FA_{1-x}MA_xPbI_3}$, and $\mathrm{CsPbI_3}$, as have been studied in this thesis, will be discussed in more detail.

2.1.1 Methylammonium lead iodide

Poglitsch and Weber [3] demonstrated in their original report that $\mathrm{MAPbI_3}$ has three distinct crystal structures depending on temperature: a low-temperature orthorhombic phase ($T < 165$ K), a tetragonal phase (165 K $< T <$ 330 K), and a high-temperature cubic phase $Pm\bar{3}m$ ($T > 330$ K). In the cubic phase, the MA cation was found to be dynamically disordered, meaning that the MA cations change orientations dynamically between all unit cell directions [3]. However, some structural details are still under discussion as described in [50], particularly regarding the degree of ordering of MA and the space group assignment of the low-temperature orthorhombic structure. The orthorhombic low-temperature structure was initially solved in the non-centrosymmetric space group $Pna2_1$ by Poglitsch and Weber [3]. Following this work, Baikie *et al.* [51] refined the structure to the centrosymmetric $Pnma$ space group using single crystal x-ray diffraction (XRD). Weller *et al.* [52] provided a more detailed picture of the MA positions and orientations in the tetragonal and orthorhombic phases from structural refinement based on neutron powder diffraction data. In the tetragonal phase, which was solved in the $I4/mcm$ space group, the MA cation was found to be disordered in the ab-plane along four directions directed towards the faces of the distorted $\mathrm{PbI_3}$ framework [52]. In the low-temperature $Pnma$ structure, $\mathrm{MA^+}$ cations are fully ordered, with the $\mathrm{NH_3}$ pointing towards the

distorted square face of the distorted perovskite structure [52]. However, a later study by Druzbicki *et al.* [53] questioned the validity of the $Pnma$ structure to describe the INS data of $MAPbI_3$ at 10 K, which is particularly sensitive to the local environment around the MA cation. Recent studies have also challenged the commonly accepted centrosymmetric $I4/mcm$ model of the room-temperature phase by claiming that the room-temperature tetragonal phase of $MAPbI_3$ is ferroelectric [54]. Breternitz *et al.* [55] further explained the origin of ferroelectricity by describing the tetragonal phase in the polar space group $I4cm$ using single-crystal XRD. The detailed structure of the cubic phase has also been debated, with high-resolution X-ray total and inelastic scattering studies suggesting that the cubic phase comprises small dynamic local tetragonal domains [56]. However, a recent study by Weadock *et al.* [57] disproved this dynamic-domain hypothesis using INS.

2.1.2 Formamidinium lead iodide

The stable phase of $FAPbI_3$ is a non-perovskite hexagonal structure at room temperature (yellow δ-phase $P6_3/mmc$) [58]. This phase has a too large electronic band gap for efficient solar absorption and is thus of little relevance for photovoltaic applications [14, 59]. However, a cubic perovskite structure of $FAPbI_3$ (black α-phase, $Pm\bar{3}m$), with an optimal band gap for solar absorption (around 1.47 eV), is formed when heating above around 410 K [14, 59, 60]. Upon cooling back to room temperature, this cubic perovskite phase is found to be metastable and can be stabilized at room temperature for several days. A progressive transition back to the δ-phase occurs only slowly. Figure 2.3 shows an illustration of the crystal structures of the δ-phase and the cubic perovskite phase of $FAPbI_3$ together with optical absorption spectra for these phases. In the perovskite phase, the optical band gap is around 1.47 eV, and there is a sharp onset of light absorption around this photon energy. For the δ-phase, the optical bandgap is much larger, and the main absorption peak occurs around 3 eV.

Upon cooling the metastable cubic α-phase, a tetragonal β-phase (space group $P4/mbm$) occurs below 285 K, and another tetragonal phase occurs below 140 K (γ-phase) [45, 58, 63, 64]. The structure of the low-temperature γ-phase is still not completely understood. Based on powder XRD data, Fabini *et al.* [63] refined the structure of the γ-phase in a new primitive tetragonal unit cell retaining the $P4/mbm$ symmetry. Later, Chen *et al.* [45] proposed another structure based on a $1 \times 1 \times 6$ supercell of the intermediate tetragonal phase where the FA cation is rotated in small steps around the c-axis. This resulted in a structure with space group $P4bm$. However, recent neutron powder diffraction data reported by Weber *et al.* [58] did not observe any high d-spacing supercell reflections as is predicted by the model by Chen *et al.*. Their results thus indicated a more disordered low-temperature structure, with possibly no long-range order of the FA cation orientations. This structural view based on diffraction studies (probing the time-averaged structure) is also in agreement with previous thermodynamic property measurement [65] and local structure studies [66], which have indicated the formation of an orientational glass of FA below ~ 100 K.

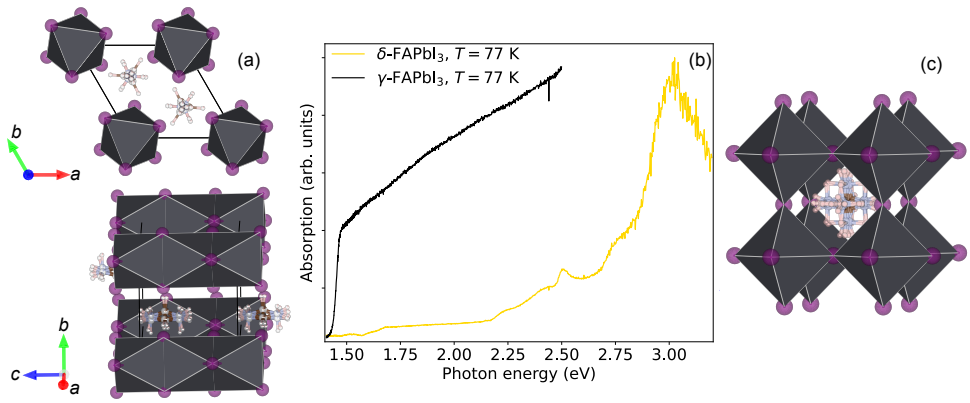

Figure 2.3: (a) Illustration of the hexagonal crystal structure of δ-FAPbI$_3$, viewed along two different directions [61]. (b) Optical absorption spectra of δ-FAPbI$_3$ and perovskite phase FAPbI$_3$ (in γ-phase) measured at 77 K (liquid nitrogen temperature). The spectra have been vertically offset for easier comparison. (c) Structure of cubic α-FAPbI$_3$. Note that in this phase, the FA cation is disordered along all directions of the unit cell [62]. The structural images were generated using the VESTA software [26].

The structures of the two low-temperature phases of FAPbI$_3$ are illustrated in Figure 2.4.

2.1.3 MA$_{1-x}$FA$_x$PbI$_3$ solid solutions

Due to the previously mentioned phase stability problem of FAPbI$_3$, a lot of efforts have recently been focused on the mixed-cation system FA$_{1-x}$MA$_x$PbI$_3$, which has been shown to stabilize the cubic perovskite structure of FAPbI$_3$ at room temperature, even for relatively low concentrations of MA [13, 14]. In addition, these mixed-cation systems show higher stability towards humidity and heat than pure MAPbI$_3$ and are among the materials with the highest power-conversion efficiencies when used in a perovskite photovoltaic device [1, 47, 67, 68]. The phase diagram of FA$_{1-x}$MA$_x$PbI$_3$ solid solutions has been recently studied by Francisco-López *et al.* [69], by Raman scattering and photoluminescence spectroscopy. They obtained the phase diagram as a function of temperature and molar ratio of FA to MA for the FA$_{1-x}$MA$_x$PbI$_3$ system, which is shown in Figure 2.5. The main results are that for low concentrations of FA, the phase behaviour is similar to that of MAPbI$_3$, while for FA concentrations above ca. 0.55, the phase behaviour is similar to that of FAPbI$_3$. Noticeably, for molar ratios of MA to FA close to 0.5, the intermediate temperature phase is completely suppressed, and the phase transition from cubic to the disordered low-temperature γ-phase occurs directly [69].

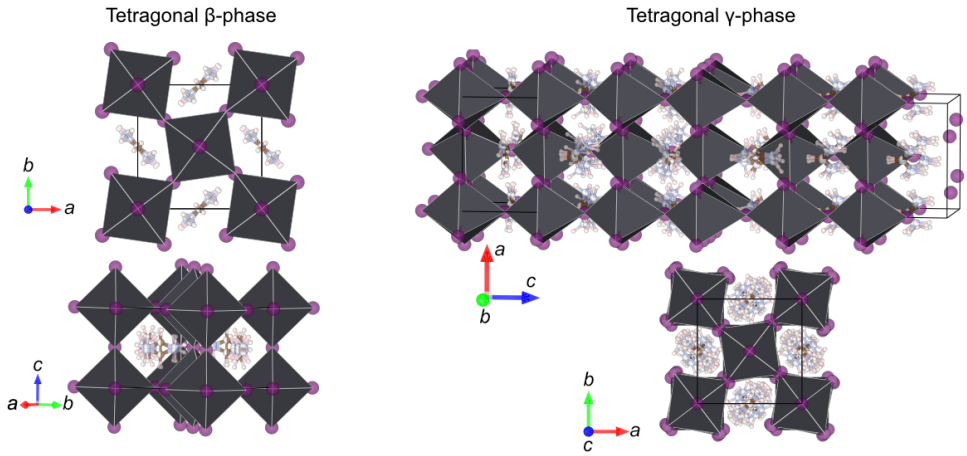

Figure 2.4: Illustration of the crystal structure of the β-phase and γ-phase of $FAPbI_3$ viewed along two different directions. Left panel: Intermediate tetragonal phase of $FAPbI_3$, based on the structural model according to Weber *et al.* [58]. Right panel: Model of the low-temperature γ-phase according to Chen *et al.* [45]. This model is based on a $1 \times 1 \times 6$ expansion of the β-phase model where the FA cation is rotated in increments around the c-axis. I, C, N, and H atoms are depicted as purple, blue, brown, and pink spheres, respectively. The Pb atoms lie within the black octahedra. The images were generated using the VESTA software [26].

Summing up, these previous studies on $FA_{1-x}MA_xPbI_3$ have clearly illustrated the difficulty in obtaining a complete understanding of the structural properties of MHPs. This is especially apparent when comparing results from different experimental methods, for example, crystallographic (diffraction) results versus results from techniques more sensitive to the local or instantaneous structure or when comparing X-ray and neutron scattering data. For X-rays, the light elements present in the organic cations are virtually invisible, but for neutrons, the scattering cross section is large, making their contrast far more apparent when using neutrons. Thus, X-rays mainly "see" the lead halide framework, whilst neutrons are very sensitive to the organic cations. One can further note that the complexity created by the additional rotational degrees of freedom of the organic cations, and the intrinsic dynamic disorder of the lead halide framework in these materials, adds further difficulty for a complete understanding of their structure. This has also been demonstrated in several local structure studies using X-ray and neutron pair distribution function analysis [70, 71], which have shown that even when the time-averaged structure appears cubic, the local structure can be significantly distorted into a local structure which is more similar to the low-temperature distorted perovskite phases. While the atomic structure of a material is critical for understanding its properties, many materials' properties are inherently linked to atomistic dynamics. This is, in particular, true for systems like $FA_{1-x}MA_xPbI_3$, which are highly dynamic at ambient temperature. While

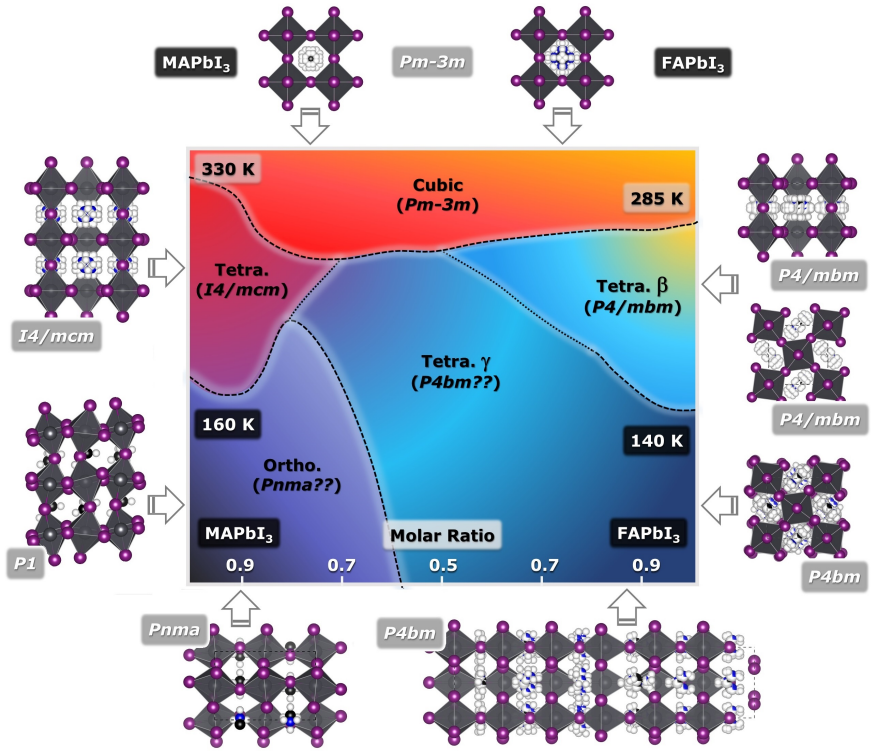

Figure 2.5: Illustration of the structural phase behaviour of the solid solutions $FA_{1-x}MA_xPbI_3$ according to Francisco-López *et al.* [69]. Pure $MAPbI_3$ and $FAPbI_3$ correspond to the left and right edges of the diagram, respectively. Space group assignments that are still not completely solved are marked with question marks. Reprinted with permission from Ref. [50], Copyright (2021) American Chemical Society.

$FA_{1-x}MA_xPbI_3$ has previously mainly been studied by crystallographic techniques, which yield the time-averaged structure, spectroscopic techniques, such as INS, are sensitive to the atomic correlation functions in both space and time and can therefore provide additional information on the local structure and dynamics of the organic cations [50].

2.1.4 Caesium lead iodide

The compound $CsPbI_3$ was first synthesized already in 1893 [72] and its crystal structure was first determined by Möller in 1958 [73, 74]. Similar to the hybrid MHPs, as discussed above, $CsPbI_3$ features several phase transitions and a complex phase-transition behaviour. The tolerance factor [75] of $CsPbI_3$ is in the lower limit of forming a perovskite structure ($t = 0.85$ [76]), and the stable structure of $CsPbI_3$ at room

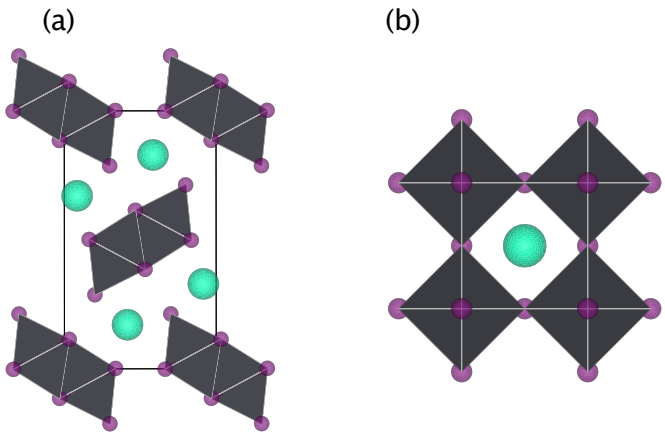

Figure 2.6: Illustration of the crystal structures of $CsPbI_3$ [49, 73, 81], studied in this thesis. (a) The at room temperature stable δ-phase. (b) The cubic α perovskite phase. Cs and I atoms are illustrated as green and purple spheres, respectively. The Pb ions lie within the black octahedra. The image was produced using the VESTA software [26].

temperature is thus an orthorhombic non-perovskite phase ($Pnma$, δ-phase), yellow in colour and with a wide band gap that is unsuitable for efficient solar absorption. This structure is similar to the δ-phase of $FAPbI_3$ and consists of 1D chains of face-sharing PbI_6 octahedra, separated by the Cs cations, see Figure 2.6. A cubic perovskite phase (α-phase, $Pm\bar{3}m$) is formed above around 595 K [73]. Metastable distorted perovskite phases of lower symmetry upon cooling the cubic phase (a tetragonal phase ($P4/mbm$ β-phase) below 554 K, and an orthorhombic phase ($Pnma$, γ-phase) below 457 K) have also been reported [49]. Sutton *et al.* [77] confirmed that the orthorhombic γ-phase could be kinetically trapped at room temperature but found it was only observed under rapid cooling whilst the transformation back to the yellow δ-phase was favoured upon slow cooling or in the presence of moisture, in agreement with earlier reports [74, 78–80]. In a recent study Strauss *et al.* [81] found that the orthorhombic perovskite phase (γ-$CsPbI_3$) could be directly synthesized and kinetically stabilized at room temperature. It was further found that γ-$CsPbI_3$ was stable under oxygen but rapidly converted to the δ-phase upon exposure to moisture.

2.2 Importance of dynamics in $A\mathrm{PbI}_3$ perovskites

That the organic cations in MHPs are highly dynamic was realized already in the original work by Poglitsch and Weber in 1987 [3]. They used millimeter-wave spectroscopy to observe dynamical relaxation on the picosecond timescale in $MAPbX_3$ (X = I, Br, and Cl) and interpreted the results in terms of a dynamic disorder of the MA cations.

In more recent years, the natural question of what is the influence of the organic cation dynamics on the optoelectronic properties of MHPs has emerged. Consequently, the organic cation dynamics in MHPs have been the subject of numerous experimental and computational studies [27, 66, 82–94]. The organic cation dynamics (in particular that of MA, which has an electric dipole) have been hypothesized to play a major role in several material properties, such as, for example, the presence of microscopic or surface ferroelectric domains [82], exciton binding energy [27], and charge recombination rates [33, 95, 96]. An important finding from both experimental and theoretical studies is that the dynamic disorder created by the rotation of the dipolar molecular cation creates polar fluctuations, which can lead to increased separation of the charge carriers, which, consequently, leads to reduced recombination rates [95, 96]. This was further established by Chen *et al.* [45], who measured the recombination rates in all crystallographic phases of $MAPbI_3$ and $FAPbI_3$ and found that phases with higher rotational entropy give rise to longer carrier lifetimes. This observation was confirmed in a recent study by Koda *et al.* [97], which, based on muon spin relaxation techniques, showed that the rotations of MA in $MAPbI_3$ lead to an extension of the photoexcited charge carriers lifetime. However, studies have also shown that such dynamical polar fluctuations also are present for the all-inorganic material $CsPbBr_3$ and might thus be intrinsic to the inorganic sublattice [29, 30]. MHPs have further been argued to belong to the class of materials known as "phonon glass electron crystals", meaning that they show conventional electron dynamics according to the electronic band theory of semiconductors but exhibit "glass-like" phonons [34, 35]. This "crystal-liquid duality" has further been hypothesized to induce large electron polaron formation and screening of charge carriers, leading to defect tolerance, moderate charge carrier mobility, and low radiative recombination properties [33–35]. This behaviour has been argued to be an effect of the weak ionic bonding and relatively large atomic masses of the lead halide frameworks [30] and the organic molecular cation reorientational motions [34]. However, a complete understanding of the nature and effect of the organic cation and perovskite lattice dynamics on the structural and optical properties of MHPs remains in many ways elusive.

For probing the rotational organic cation dynamics in MHPs, a powerful experimental technique is QENS. This is because their dynamics occur at the time and length scales directly accessible to neutron scattering [3, 27], and the large incoherent neutron cross section of hydrogen, which is present in the organic cation ends, makes neutrons sensitive to the self-dynamics of the organic cations. The localized rotational motions of the organic cations have been directly probed in previous studies by QENS for the MA-containing compounds $MAPbI_3$ [27, 82, 83, 87], $MAPbBr_3$ [88, 98], and $MAPbCl_3$ [99, 100]. As a primary example, Chen *et al.* [27] used a group theoretical symmetry analysis of their QENS data to show that for $MAPbI_3$, in the room temperature tetragonal structure and high-temperature cubic phase, the whole MA cation performs rotations of four-fold symmetry around the crystallographic c-axis, whilst in the low-temperature orthorhombic phase, only the three-fold rotations of the methyl and/or ammonia group around the C−N axis persist. Figure 2.7 shows an illustration

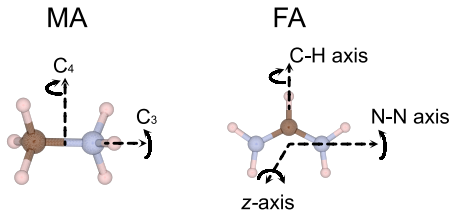

Figure 2.7: Schematic illustration of the various possible rotational modes of MA and FA [10, 27, 101, 102] in lead halide perovskites. Note that FA is a planar molecule. Adapted with permission from Paper I [102].

of these rotational motions. Interestingly, Chen *et al.* [27] could further correlate their results for the MA rotational dynamics to the low exciton binding energy and low charge recombination rate in $MAPbI_3$. The onset of cation reorientations in the tetragonal phase of $MAPbI_3$ was found to occur at the same temperature as a sharp increase in the dielectric function. Since the exciton binding energy is inversely proportional to the dielectric function, this suggested that the activation of full MA rotations in $MAPbI_3$ is related to the lowering of the exciton binding energy in this material [27].

Contrastingly, the cation dynamics in FA-based MHPs have been studied much less than for $MAPbI_3$. A QENS study on $FAPbBr_3$ was recently reported by Sharma *et al.* [101]. They showed that the FA cation performs isotropic rotations for all measured temperatures ($100 - 350$ K), with an increasing fraction of FA cations contributing to the dynamics with increasing temperature. However, Mozur *et al.* [103, 104] have found that the FA cation orientation and dynamics in $FAPbBr_3$ relate to unusual temperature trends in the photoconductivity and that the dynamics are highly dependent on local structural distortions. The FA cation dynamics in $FAPbI_3$ have also been investigated by several experimental techniques [66, 84, 105, 106]. For example, Fabini *et al.* [66] used a combination of nuclear magnetic resonance (NMR), dielectric spectroscopy, and density functional theory (DFT) simulations to show that the FA cation primary reorients around the N...N axis (see Figure 2.7) in all crystallographic phases, with a relaxation time of about 8 ps at RT. In another NMR study by Kubicki *et al.* [84], it was found that at room temperature, the FA cation rotation in $FAPbI_3$ is more than one order of magnitude faster than for MA in $MAPbI_3$, despite the larger size of FA. These results are at variance with the NMR results reported by Fabini *et al.*, who showed that the reorientation rate of MA and FA in $MAPbI_3$ and $FAPbI_3$ are very similar at room temperature [66]. Mishra *et al.* [107] recently reported a comprehensive NMR investigation on the cation rotations in a wide range of MHPs, including $MAPbI_3$, $FAPbI_3$, and $FA_{1-x}MA_xPbI_3$. They showed that the FA correlation times at room temperature for FA cation are lower than 1.5 ps for rotations around all three principal axes (see Figure 2.7) and that

the rotational dynamics in the cubic phase do not change significantly when doping $\mathrm{FAPbI_3}$ with $\mathrm{MA^+}$.

2.2.1 Phonons and phase transitions

Displacive phase transitions are typically described in terms of a "soft phonon", *i.e.* a phonon whose frequency goes to zero at the phase transition and whose dynamic atomic displacements give rise to the distorted crystal structure in the new phase [108, 109]. At the phase transition, these displacements "freeze in" and become static in the lower symmetry phase. This model describes most phase transitions in oxide perovskites [108, 109]. For MHPs, an early INS study on $\mathrm{CsPbCl_3}$ explained the phase transition in terms of a similar soft phonon mechanism [110], which also is in agreement with more recent work on $\mathrm{CsPbBr_3}$ [32]. Lanigan-Atkins *et al.* recently reported that the $\mathrm{PbBr_6}$ octahedra tilting modes, which are related to the structural phase transitions, in $\mathrm{CsPbBr_3}$ are overdamped along the whole $M - R$ branch of the Brillouin zone in the cubic phase [29]. This highly unusual behaviour was further elaborated on in a recent molecular dynamics simulation study by Fransson *et al.* [111], which found that these modes remain overdamped even far above the phase transition temperatures. These overdamped phonon modes give rise to relaxational dynamics of the lead halide octahedra, which can give rise to many different local dynamic structures of lower symmetry in the cubic perovskite phase, which has been shown in recent molecular dynamics simulation studies [112, 113].

For the hybrid MHPs, the situation is even more complex because of the additional degrees of freedom of the organic cations. An INS study of a powder sample of $\mathrm{MAPbBr_3}$ reported a soft-phonon mode whose frequency approached zero towards the orthorhombic-to-tetragonal phase transition [88]. However, more recent studies on $\mathrm{MAPbI_3}$ have found that the orthorhombic-to-tetragonal phase transition is of first-order [114] and is also an order-disorder transition of the MA cation ordering [27]. The tetragonal-to-cubic phase transition in the hybrid MHPs $A\mathrm{Pb}X_3$ (A = MA, FA; X = I, Br) were recently studied in detail by Hehlen *et al.* [115] using INS, Raman scattering, and Brillouin scattering. In particular, they found a very similar phase transition behaviour for all these compounds and could not observe any soft phonon mode, which indicated that the transition is not of displacive character. They further found a slow relaxational component in Brillouin scattering spectra which was assigned to anharmonic dynamics of the cation center of mass in the perovskite structure and was argued to be related to the phase transition mechanism [115]. Taken together, the phase transition mechanisms in MHPs is generally very complex and remain not fully understood. For the hybrid MHPs, the non-spherical geometry and more complex interactions with the lead halide framework of the organic cations add an additional complexity to the problem. This is particularly true for the low-temperature structures where the interactions between the cations and perovskite cage can become frustrated [66], leading to locally disordered structures [58].

2.3 Crystal structures of layered lead iodide perovskites

2.3.1 Phenethylammonium lead iodide

The original work solved the crystal structure of PEA_2PbI_4 in the monoclinic space group $C2/m$ [116], using single-crystal XRD. However, there was some disorder in the relative orientation of the PbI_6 octahedra, indicating potentially a larger unresolved supercell expansion in the *ab* plane. Some later studies have favoured a triclinic structure with $P\bar{1}$ symmetry [117, 118] with 4 chemical formulae per unit cell ($Z = 4$), or another $P\bar{1}$ structure with $Z = 2$ [119], or a lower symmetry monoclinic structure (space group Cc) [120], which all are related to the $C2/m$ structure by a supercell expansion along the directions of the inorganic Pb−I layers. Another study by Song *et al.* further found that PEA_2PbI_4 can exist as two distinct polymorphs [121], one monoclinic and one triclinic, and which exhibit different photoluminescence behaviour. The $Z = 4$ $P\bar{1}$ structure according to Ref. [118] is illustrated in Figure 2.8.

2.3.2 Butylammonium lead iodide

The crystal structure of BA_2PbI_4 is orthorhombic at room temperature with space group *Pbca* and $Z = 4$ [119, 122]. It further undergoes a first-order structural phase transition to an iso-symmetrical (same space group) low-temperature phase, with a large hysteresis in the transition temperatures, around 240 K on cooling and 270 K on heating [122]. In the low-temperature structure, the out-of-plane octahedral tilt angle is relatively large, and the organic cations are less aligned towards the *c*-axis. In the high-temperature phase, the octahedral tilt angle is significantly smaller but non-zero, and the organic cations are more aligned with the long molecular axis parallel with the *c*-axis [119], and there is, in addition, some disorder in the organic cation positions.

2.4 Importance of dynamics in layered lead iodide perovskites

Recent studies of layered MHPs have revealed unusual and interesting interactions between lattice and electronic degrees of freedom [123–130], showing that the vibrational dynamics is directly relevant for understanding the optoelectronic properties of these materials [131]. In addition, dynamical disorder [132–134], organic cation dynamics [135–138], and strong anharmonicity [119, 139] have been shown to influence the optoelectronic properties of the materials. The organic cation dynamics in layered MHPs have been studied experimentally using both NMR and QENS techniques. The first experimental study of the molecular reorientation rates in $PEA_2MA_{n-1}Pb_nI_{3n+1}$ ($n = 1, 2$) was reported in 1996 using NMR [140]. The dynamics of the organic cations have since then been studied in more recent experiments [135, 137, 138, 141–143].

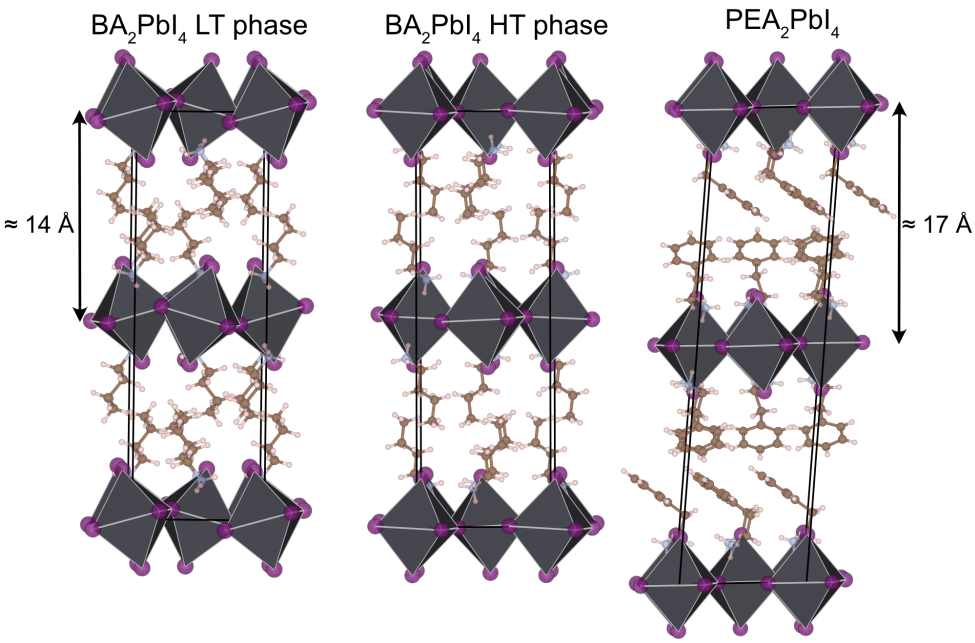

Figure 2.8: Illustration of the crystal structures of BA_2PbI_4 (low and high temperature phases) [119] and PEA_2PbI_4 [118]. The approximate distances between the lead iodide layers for the two materials are indicated. The solid lines indicate a unit cell. The images were generated using the VESTA software [26].

Hu *et al.* [138] recently reported a detailed QENS study of $(C_8H_{17}NH_3)_2PbI_4$ which showed that the type of rotational dynamics depends on the crystallographic phase, with only C_3 rotations of ammonia and methyl groups observed in low-temperature and intermediate-temperature phases, and rotations around the crystallographic *c*-axis and other CH_2 group librations observed in the high-temperature phase. Another QENS study [135] claimed that there is a correlation between those types of organic cation dynamics and broadband luminescence in layered lead bromide perovskites. Dahlman *et al.* [137] reported a detailed NMR study on the organic cation dynamics in PEA_2PbI_4, BA_2PbI_4, and $(C_8H_{17}NH_3)_2PbI_4$. Their results indicated similar dynamics in BA_2PbI_4 and PEA_2PbI_4. In particular, they found that the phenyl ring rotations in PEA_2PbI_4 are relatively slow and occur on timescales between $10 - 100$ μs [137]. However, the exact nature of the probed dynamics in BA_2PbI_4 was not fully understood.

The organic cation dynamics have also been studied using computational techniques. A recent molecular dynamics simulation study showed that even though the BA organic cation is relatively large, the whole organic molecular cation rotates at room temperature in BA_2PbBr_4 [134]. This was further found to induce dynamical potential

fluctuations, similar to as been proposed for the 3D MHPs, that are sufficient to localize the charge carrier wavefunction, thus enhancing the charge carrier lifetimes due to electron-hole separation [134]. Interestingly, it was further found that the potential fluctuations are induced from a motion of the net charge centers of the organic cations and that they are also present in the all-inorganic material Cs_2PbBr_4 [134]. Thus, the presence of organic cations is not solely responsible for the presence of such local polar fluctuations, which is in line with the current understanding of 3D MHPs [30].

Chapter 3

Oxyhydride perovskites

3.1 Structure and properties

Transition metal oxyhydrides are formed by reducing transition metal oxides when the oxide anions (O^{2-}) are partly replaced by hydride ions (H^-). These materials thus belong to the rather rare class of materials called mixed anion compounds, *i.e.* they are based on different anions in the same substructure. One of the first reported transition metal oxyhydrides was discovered by Hayward *et al.* in 2002 [144]. They reported the synthesis of $LaSrCoO_3H_{0.7}$ upon reduction with CaH_2 of the Ruddlesden-Popper phase oxide precursor $LaSrCoO_4$. This material generated a lot of scientific interest, mainly because of the possible novel electronic and magnetic properties that could be introduced with the hydride ions. In addition to this, there were open questions related to the mechanism of hydride-ion insertion into the oxide and the possibility of hydride-ion conduction. Subsequent studies investigated $LaSrCoO_3H_{0.7}$ with respect to magnetic and electronic properties [145] and hydride-ion diffusion [43].

The relatively simple synthesis method developed by Hayward *et al.* [144], "topochemical" reduction with CaH_2 (or other metal hydrides), also provided more opportunities for further discoveries of novel oxyhydride phases upon hydride reduction of transition metal oxides. After this pioneering work, a few other transition metal oxyhydrides were synthesized using the same methods [146, 147]. However, the number of discovered transition metal oxyhydrides so far is still relatively limited. This is because whilst the topochemical reduction of transition metal oxides with metal hydrides can often be performed to form highly reduced oxide phases, such as $LaNiO_2$ [148] or $SrFeO_2$ [149], with unusual transition metal coordination environment, hydride insertion is still relatively rare [150, 151]. In 2012, Kobayashi *et al.* reported the synthesis of $BaTiO_{3-x}H_x$ (with x up to 0.6) [39], which shortly after was followed to include the series $ATiO_{3-x}H_x$ (A = Ba, Sr, and Ca) [42, 152]. This was the first example of an oxyhydride based on the simple cubic perovskite structure. Later on, other perovskite-type oxyhydrides, such as $SrVO_2H$ [36] and $SrCrO_2H$ [153] have been

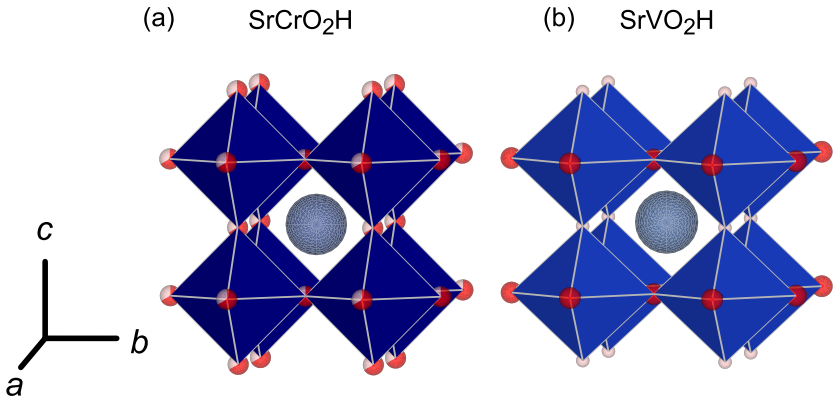

Figure 3.1: (a) Crystal structure of cubic $SrCrO_2H$ according to Ref. [153]. Sr, O, and H atoms are shown as grey, red, and pink spheres, respectively. The Cr ions are inside the dark blue octahedra. The 2/3 red and 1/3 pinked coloured spheres illustrate the structural disorder in the anion substructure. (b) Crystal structure of anion-ordered tetragonal $SrVO_2H$ according to Ref. [36]. The V ions are inside the dark blue octahedra. The images were generated using the VESTA software [26].

reported. Interestingly, even though all of these materials are formed from transition metal oxides with perovskite structures, different cases regarding the anion ordering and concentrations have been encountered. Both $ATiO_{3-x}H_x$ (A = Ba, Sr) [39, 152] and $SrCrO_2H$ [153] display average cubic perovskite structures in which the O^{2-} and H^- anions are completely disordered in a solid solution behaviour [Figure 3.1 (a)]. $CaTiO_{3-x}H_x$ display an orthorhombic distorted perovskite structure, but still with an anion disorder [152]. For $SrVO_2H$, a very different scenario has been observed, where the O^{2-} and H^- anions are perfectly ordered in a tetragonal structure that is related to the cubic perovskite structure [36]. This anion-ordered structure of $SrVO_2H$ is illustrated in Figure 3.1 (b). The anion-ordering stems from the local bonding preference of the V^{3+} cation, where the trans-orientation is preferred for the two locally coordinated H^- [154], and the octahedral coordination is completed by 4 O^{2-} in a square-planar coordination. Both $SrCrO_2H$, with Cr^{3+} d^3 species, and $SrVO_2H$, with V^{3+} d^2 species (Figure 3.2), exhibit antiferromagnetic (AFM) ordering, which remains intact for relatively high temperatures above room temperatures. The Néel temperature of $SrCrO_2H$ is 380 K [153] and above 430 K for $SrVO_2H$ [36, 155]. For both $SrCrO_2H$ and $SrVO_2H$, the AFM structure is of G-type with a 10-atom body-centered tetragonal unit cell that is based on a $\sqrt{2} \times \sqrt{2} \times 2$ expansion of the non-magnetic cell [36, 153]. The AFM structure of $SrVO_2H$ is shown in Figure 3.2(a). For $BaTiO_{3-x}H_x$, the Ti cations are in a mixed Ti^{3+}/Ti^{4+} oxidation state, where only the Ti^{3+} have one remaining d-electron. Consequently, $BaTiO_{3-x}H_x$ does not

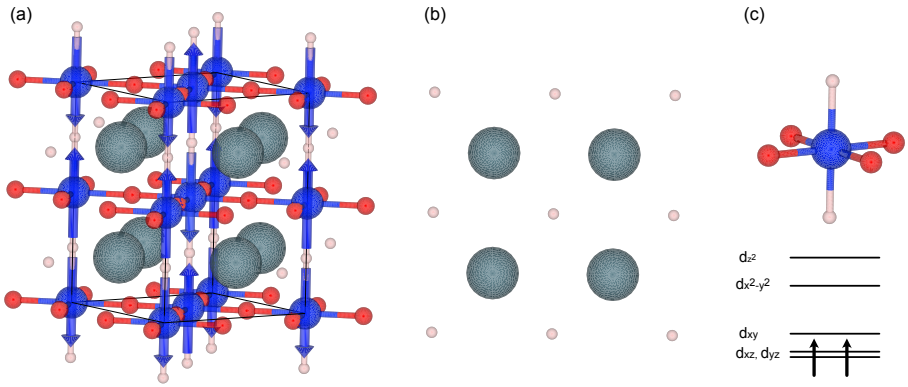

Figure 3.2: Schematic illustrations of the structure of $SrVO_2H$. (a) Illustration of the antiferromagnetic structure of $SrVO_2H$ according to Ref. [36]. Sr, V, O, and H ions are shown as grey, blue, red, and pink spheres, respectively. The antiferromagnetically ordered spins of the V^{3+} cations are illustrated as arrows and lie parallel to the *c*-axis. (b) Illustration of the *ab*-plane of the crystal structure where the hydride-ions lie coordinated to Sr in a square-planar fashion. (c) Local coordination of V by 4 O and 2 H leads to a $(d_{xz}, d_{yz})^2$ electronic state [36]. The images were generated using the VESTA software [26].

show any long-range magnetic ordering but is paramagnetic down to, at least, 5 K [39].

Transition metal oxyhydrides show a variety of interesting and useful properties, including electron transport, mixed ionic-electronic conductivity, magnetic, and catalytic properties [156]. $SrVO_2H$ has been investigated theoretically with respect to electronic and magnetic properties, finding unusually strong magnetic couplings that are dependent on the hydride-ions [38, 157]. Further, a high-pressure XRD study has shown that the hydride-ions in $SrVO_2H$ are extraordinarily compressible and that pressure drives an insulator-to-metal transition [37]. In general, transition metal oxyhydrides allow for interesting magnetic and electronic properties to occur because they may allow access to unusually low oxidation states of the transition metals. Such materials include, for example, the recently discovered 4*d* transition metal oxyhydrides $LaSr_3NiRuO_4H_4$ and $LaSrCo_{0.5}Rh_{0.5}O_3H$ [158, 159] and $LaSrMnO_{3.3}H_{0.7}$ [160] that can be stabilized by high pressure methods.

3.2 Hydride-ion dynamics

3.2.1 Hydride-ion diffusion in perovskite oxyhydrides

The initial study of hydride-ion dynamics in transition metal oxyhydrides was reported in 2006 by Bridges *et al.* [43] by QENS. They observed quasielastic scattering of $LaSrCoO_3H_{0.7}$ for temperatures above 675 K, which is close to the decomposition temperature of the sample material. Analysis of the momentum transfer dependence of the QENS linewidth showed that the diffusion mechanism could be interpreted in terms of vacancy-assisted hydride-ion jump diffusion mechanism, restricted to jumps along the a-axis in the crystal structure. The hydride-ion diffusion was only observed for temperatures near or above the sample decomposition temperature and in conjunction with hydrogen loss, whereas below 675 K, no hydride-ion diffusion was observed on the probed timescales [43]. Later on, the mobility of the hydride-ions was once more demonstrated, for the case of the perovskite oxyhydride $BaTiO_{3-x}H_x$. Gaseous exchange experiments of $BaTiO_{3-x}H_x$ demonstrated the exchange of hydride ions in the material by deuterium (D) and N in the presence of D_2 and N_2 gas, respectively, above 400 °C [39, 161, 162]. This demonstrated that the hydride-ions are mobile in $BaTiO_{3-x}H_x$ at higher temperatures and thus raised questions about possible hydride ion diffusion mechanisms. Following these works, the hydride-ion diffusion in $ATiO_{3-x}H_x$ (A = Ba and Sr) has been studied with several different experimental and computational techniques [44, 163–166]. Tang *et al.* [164] performed gaseous hydrogen release/exchange experiments and first-principles simulations and reported a hydride-ion diffusion mechanism that is highly dependent on the concentration of hydride ions (x), with the simultaneous diffusion of oxygen ions for low x, whereas for $x > 0.4$ only the hydride ions move. The activation energy was found to significantly decrease with increasing x until around $x = 0.4$, after which it was roughly constant. The experimental activation energy, determined from analysis of the gaseous exchange experiment, was, however, determined to be relatively high for both of these processes, in the range of 2–3.85 eV [164]. They further reported the activation of about 1 eV from DFT simulation for nearest neighbour jumps of a hydride ion to an oxygen vacancy [164]. However, in another DFT study, a much lower activation energy of about 0.28 eV was reported for the nearest neighbouring oxygen-vacancy mediated hydride-ion diffusion [165]. The hydride-ion diffusion in $SrTiO_{3-x}H_x$ was also studied using isotope exchange and depth profiling methods combined with density functional theory calculations by Liu *et al.* [166]. Their results showed the presence of a highly correlated long-range transport of hydride-ions that is impeded by slow reorganization of the oxygen sublattice. Interestingly, they could also calculate the correlation factors for this correlated jump-diffusion process and thus relate their measured tracer diffusion coefficient to the self-diffusion coefficient. This is illustrated in Figure 3.3, which shows the measured self-diffusion coefficient and calculated correlation factors of hydride ion diffusion in $SrTiO_{3-x}H_x$ thin films by Liu *et al.* [166]. The hydride-ion dynamics in $BaTiO_{3-x}H_x$ samples characterized by a relatively large concentration of oxygen vacancies was further studied using QENS by Eklöf-Österberg *et al.* [44]. The QENS data showed the presence of a highly temperature-dependent diffusion

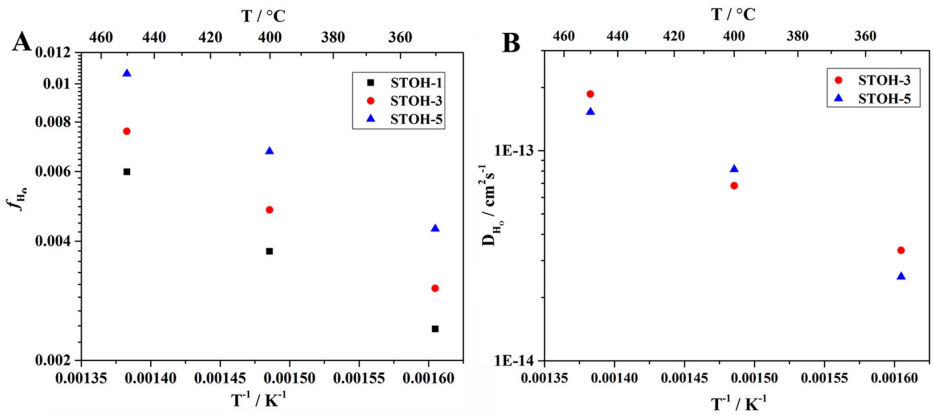

Figure 3.3: Temperature dependencies of (A) the calculated correlation factors and (B) self-diffusion coefficients for hydride ion diffusion in thin films of $SrTiO_{3-x}H_x$ from Liu *et al.* [166]. Reprinted with permission by the American Chemical Society from "Highly Correlated Hydride Ion Tracer Diffusion in $SrTiO_{3-x}H_x$ Oxyhydrides", Journal of the American Chemical Society **141** 4653 (2019), Liu *et al.* [166]. Copyright (2019) American Chemical Society.

mechanism, characterized by jump-diffusion to nearest neighbouring oxygen vacancies at low temperature ($T \leq 250$ K) and with the presence of hydride-ion jumps between next-nearest neighbouring oxygen vacancies at higher temperatures ($T >$400 K). The observed diffusional dynamics were also characterized by a relatively low apparent activation energy on the order of 0.1 eV [44].

3.2.2 Hydride-ion diffusion oxyhydrides with other crystal structures

The recent study by Kobayashi *et al.* [40], which demonstrated pure hydride-ion conductivity in $La_{2-x-y}Sr_{x+y}LiH_{1-x+y}O_{3-y}$, using a solid-state battery built from the oxyhydride, have created further excitement with the aim of developing new solid-state ionics applications based on H^- conduction using oxyhydride materials [167]. Figure 3.4 shows the solid-state battery built from $Ti/La_2LiHO_3/TiH_2$ by Kobayashi *et al.* [40]. La_2LiHO_3 functions as the electrolyte, and the Ti and TiH_2 as electrodes. Upon discharge, they observed, using XRD, the formation of titanium hydride at the Ti anode and the release of H at the TiH_2 cathode to form α-Ti. This experiment thus demonstrated the hydride ion conduction in La_2LiHO_3. Takeiri *et al.* [168] recently reported a similar material, in terms of a new Ruddlesden-Popper phase oxyhydride $Ba_{1.75}LiH_{2.7}O_{0.9}$, with a relatively large amount of hydride-ion vacancies which were found to be ordered at room temperature. Interestingly, they observed a phase transition at higher temperatures ($T >$ 588 K), where the ordering of vacancies is lost. This high-temperature phase was found to be featured by a significant

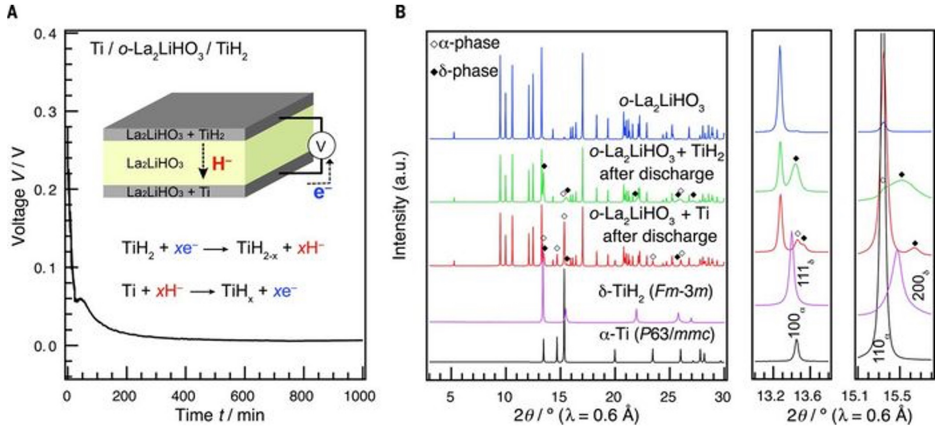

Figure 3.4: (a) Discharge curve for a solid-state battery based on the oxyhydride $La_{2-x-y}Sr_{x+y}LiH_{1-x+y}O_{3-y}$ as a solid electrolyte. (b) XRD patterns of the electrolyte, cathode, and anode materials. From "Pure H^- conduction in oxyhydrides", Science **351** 1314-1317 (2016), Kobayashi *et al.*, DOI: (10.1126/science.aac9185) [40]. Reprinted with permission from The American Association for the Advancement of Science (AAAS). Copyright (2016) AAAS.

hydride-ion conductivity, which was observed using both conductivity measurements and QENS [168]. Those results thus showcase the importance of structure, and in particular, the presence of vacancies and disorder to promote hydride ion diffusion. However, the hydride-ion diffusion mechanisms in oxyhydrides are far from being fully understood. The development of new oxyhydride materials with superior properties is highly dependent on elucidating the mechanism of hydride-ion conductivity further. In particular, it is important to understand the mechanistic details of the diffusion process in terms of timescales, geometry, activation energies, and how this depends on the hydride ion and anion vacancy concentration in the materials. A primary tool for gaining insights into the diffusion mechanism at the atomic scale is neutron scattering, which will be described in the following chapter.

Chapter 4

Methods

4.1 Neutron scattering

4.1.1 General characteristics of neutron scattering

[1]This section gives a brief overview of neutron scattering as an experimental technique used in the condensed matter sciences and follows mainly the references [169–171]. The scattering of cold and thermal neutrons[2] is an important experimental tool with applications over a wide range of science including physics, chemistry, materials science, and biology. Using neutrons as a probe of materials has several advantages, which derive directly from the fundamental properties of neutrons [169]. Neutrons have no electric charge and thus interact directly with the nuclei of the sample material via nuclear interactions. Typically, this means that the neutron can penetrate deep into the sample, ensuring that bulk properties are being probed. In addition, the nuclear interaction varies randomly over the periodic table and also allows for isotope contrast. Of specific concern to this thesis, hydrogen has a very large scattering cross section by neutrons, whilst it is virtually invisible to X-rays. In addition, the de-Broglie wavelength of thermal neutrons is of the order of interatomic spacings in solids. Consequently, neutron diffraction measurements can be performed to obtain information about the atomic structure of materials [169]. Lastly, the energies of thermal and cold neutrons are on the order of $1 - 100$ meV, which is of the same order as the energies of many excitations in solids, such as phonons, magnons (and other magnetic excitations), and crystal field excitations. The measurements of inelastically scattered neutrons thus allow probing also the dynamics of atoms in materials. Lastly,

[1]This chapter is partly based on my Licentiate thesis.

[2]Thermal neutrons refer to neutrons with energies around $10 - 100$ meV, which is similar to the thermal energy at room temperature ($k_{\mathrm{B}}\,T \approx 25$ meV). Cold neutrons refer to neutrons having energies lower than this, around $0.1 - 10$ meV. The term temperature is used because the neutrons produced in a reactor or spallation neutron source are moderated in a medium with a certain temperature. The energy distribution of the moderated neutrons will then be a Maxwell-Boltzmann distribution with a maximum at $3k_{\mathrm{B}}T/2$ with T being the moderator temperature [171].

the neutron has a magnetic moment, making it also sensitive to magnetism [169].

4.1.2 Theoretical description of the scattering process

The measured quantity in a neutron scattering experiment is related to the differential cross section $\mathrm{d}^2\sigma/\mathrm{d}\Omega\mathrm{d}E_\mathrm{f}$, which is proportional to the number of neutrons scattered per time unit into a small solid angle $\mathrm{d}\Omega$ and with final energy between E_f and $E_f + \mathrm{d}E_\mathrm{f}$. This scattering process is illustrated in Figure 4.1 (a).

For a theoretical understanding of the scattering process, consider a neutron characterized by a plane wave with initial wavevector $\mathbf{k}_i$ and energy $E_i = \hbar^2 k_i^2/2m$ incident on a sample, which is scattered *via* the nuclear interaction with the sample into another state with a final wavevector $\mathbf{k}_f$ and energy $E_f = \hbar^2 k_f^2/2m$. m is here the neutron mass and $\hbar$ is the reduced Planck constant. The scattering data is typically expressed in terms of the wavevector transfer[3] $\mathbf{q}$ and the energy transfer E, defined as, $\mathbf{q} = \mathbf{k}_i - \mathbf{k}_f$, and $E = E_i - E_f$. From this, one sees that $\mathbf{q}$ and E are not independent variables because the neutron energy depends on its wavevector. The magnitude of the wavevector transfer $q = |\mathbf{q}|$, can be expressed as

$$q^2 = |\mathbf{k}_i - \mathbf{k}_f|^2 = k_i^2 + k_f^2 - 2\,k_i\,k_f\,\cos\theta = \frac{2m}{\hbar^2}\left(E_i + E_f - 2\sqrt{E_i E_f}\cos\theta\right), \quad (4.1)$$

where θ is the angle between the incident and final neutron wavevectors [see Figure 4.1 (a)]. From this equation, it is clear that the (q, E) region that can be probed in an experiment is limited and that it depends on the incident neutron energy and the largest scattering angle θ that can be measured. In particular, this will lead to a curved region in (q, E)-space being measured in an experiment. This is illustrated in Figure 4.1 (b), which shows the INS data collected from a powder sample of $MAPbI_3$. Note that the probed region in (q, E) space is not a rectangle but curved. The energy and momentum transfers are given by $E = \hbar\omega$ and $\mathbf{p} = \hbar\mathbf{q}$, respectively, where ω is the angular frequency. Thus, ω or $\hbar\omega$ is often used interchangeably with E, and this will be done for the rest of this thesis.

The interaction between the nuclei in the scattering system and the neutron is of short-range, several orders of magnitude shorter than the neutron wavelength. The neutron-nucleus interaction can be approximated by the so-called Fermi pseudopotential [169]

$$V(\mathbf{r}) = \frac{2\pi\hbar^2}{m}\sum_j b_j \delta(\mathbf{r} - \mathbf{R}_j),$$

where b_j is the so-called neutron scattering length of nucleus j and $\mathbf{R}_j$ is the position vector of nucleus j. The neutron-nucleus interaction is therefore characterized by a single parameter, the scattering length b. b varies randomly with the atomic mass number and depends on the spin state of the neutron-nucleus system. The integrated

[3]The momentum transfer is $\hbar\mathbf{q}$; thus, q is commonly also referred to as the momentum transfer.

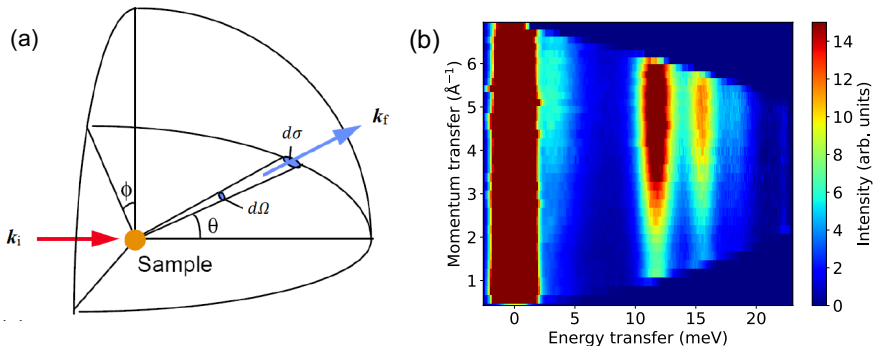

Figure 4.1: (a) Illustration of the scattering geometry in a neutron scattering experiment in real space. Adapted from [169, 172]. (b) INS data of a powder sample of $MAPbI_3$ at 2 K. The data were measured on the IN5 spectrometer at the Institut Laue-Langevin using an incident neutron wavelength of 1.7 Å.

total cross-section of such a potential is $\sigma_{\text{tot}} = 4\pi b^2$, which can be interpreted as an "effective area" of the nuclei which the neutron "sees". An expression for the double differential cross section $\mathrm{d}^2\sigma/\mathrm{d}\Omega\mathrm{d}E_\mathrm{f}$ can be written as [169]

$$\frac{\mathrm{d}^2\sigma}{\mathrm{d}\Omega\mathrm{d}E_\mathrm{f}} = \frac{k_f}{k_i}\frac{1}{2\pi\hbar}\sum_{j,j'} b_j b_{j'} \int_{-\infty}^{\infty} \mathrm{d}t \left\langle \exp\left(-\mathrm{i}\mathbf{q}\cdot\mathbf{R}_{j'}(t=0)\right)\exp\left(\mathrm{i}\mathbf{q}\cdot\mathbf{R}_j(t)\right)\right\rangle \times \exp\left(-\mathrm{i}E\,t/\hbar\right), \tag{4.2}$$

where $\mathbf{R}_j(t)$ is the time-dependent position operator of nuclei j in the Heisenberg picture, and the brackets $\langle\ldots\rangle$ refer to the thermal average[4]. Note that b_j is here the scattering length of nuclei j, which may vary randomly from one nucleus to another because of different nuclear spin states and/or the presence of isotopes. By letting f_i be the relative frequency of the value b_i, the average value of the scattering length can be written as $\overline{b} = \sum_i f_i b_i$. Assuming no correlation between the scattering lengths of different nuclei, one may write [169]

$$\overline{b_{j'}b_j} = (\overline{b})^2, \qquad j' \neq j, \tag{4.3}$$

$$\overline{b_{j'}b_j} = \overline{b^2}, \qquad j' = j. \tag{4.4}$$

By taking the average of the different possible distributions of b_j values in Eq. (4.2), it can conventionally be rewritten in terms of coherent and incoherent neutron scattering

[4]For an operator A the thermal average is given by $\langle A\rangle = \sum_\lambda p_\lambda \langle\lambda|A|\lambda\rangle$, where

$$p_\lambda = \frac{\exp(-E_\lambda/k_\mathrm{B}T)}{\sum_\lambda \exp(-E_\lambda/k_\mathrm{B}T)}$$

is the probability that the scattering system is in the state λ [169].

as

$$\frac{\mathrm{d}^2\sigma}{\mathrm{d}\Omega \mathrm{d}E_\mathrm{f}} = \left(\frac{\mathrm{d}^2\sigma}{\mathrm{d}\Omega \mathrm{d}E_\mathrm{f}}\right)_\mathrm{coh} + \left(\frac{\mathrm{d}^2\sigma}{\mathrm{d}\Omega \mathrm{d}E_\mathrm{f}}\right)_\mathrm{inc}, \tag{4.5}$$

where the coherent and incoherent parts are respectively given by the expressions [169]:

$$\left(\frac{\mathrm{d}^2\sigma}{\mathrm{d}\Omega \mathrm{d}E_\mathrm{f}}\right)_\mathrm{coh} = \frac{\sigma_\mathrm{coh}}{4\pi}\frac{k_f}{k_i}\frac{1}{2\pi\hbar}\sum_{j,j'}\int_{-\infty}^{\infty}\mathrm{d}t\,\langle \exp\left(-\mathrm{i}\mathbf{q}\cdot\mathbf{R}_{j'}(t=0)\right)\exp\left(\mathrm{i}\mathbf{q}\cdot\mathbf{R}_j(t)\right)\rangle$$
$$\times \exp\left(-\mathrm{i}E\,t/\hbar\right), \text{ and} \tag{4.6}$$
$$\left(\frac{\mathrm{d}^2\sigma}{\mathrm{d}\Omega \mathrm{d}E_\mathrm{f}}\right)_\mathrm{inc} = \frac{\sigma_\mathrm{inc}}{4\pi}\frac{k_f}{k_i}\frac{1}{2\pi\hbar}\sum_{j}\int_{-\infty}^{\infty}\mathrm{d}t\,\langle \exp(-\mathrm{i}\mathbf{q}\cdot\mathbf{R}_j(t=0))\exp(\mathrm{i}\mathbf{q}\cdot\mathbf{R}_j(t))\rangle$$
$$\times \exp\left(-\mathrm{i}E\,t/\hbar\right). \tag{4.7}$$

Here, $\sigma_\mathrm{coh} = 4\pi(\bar{b})^2$ and $\sigma_\mathrm{inc} = 4\pi(\overline{b^2} - (\bar{b})^2)$ are the so-called coherent and incoherent cross sections, respectively. It can be seen that the coherent scattering depends on the correlation of the same and different nuclei at different times. The coherent scattering thus contains interference effects of the scattered neutrons (including diffraction). The incoherent scattering, on the other hand, depends only on the correlations of the same nuclei at different times and does not, therefore, contain any interference effects. The incoherent scattering arises due to the random deviations of the scattering lengths from their mean value for each type of nucleus in the sample [169]. It should be noted that even for the incoherent neutron scattering, there is always a coherent superposition of the outgoing neutron waves − it is only the averaging process that leads to a cancellation of the phase factors [171]. Thus, the coherent scattering is the scattering which the same system would give if all scattering lengths were given by the mean value $\bar{b}$, whilst the incoherent scattering is the term one must add to obtain the scattering from the actual system [169]. This separation of the scattering cross section into a coherent and an incoherent part is especially useful for samples containing H because the incoherent cross section of H is 80.26 barn whilst the coherent part is only 1.75 barn [171].[5] Thus, neutron scattering by hydrogen is largely dominated by the self-terms, and the measured inelastic scattering signal can, in most cases, be interpreted in terms of self-dynamics. For neutron diffraction experiments, however, samples containing H can sometimes be problematic because the incoherent scattering gives a large background to the diffraction data. Thus, it is common in diffraction experiments to replace H with deuterium (D) because D possesses the twin advantage of having a much smaller σ_inc and a larger σ_coh. However, for QENS studies, where one probes dynamics and which is of specific concern in this thesis, it is beneficial to have a large incoherent cross-section of the probed atomic species. It should be pointed out that even though this separation of coherent and incoherent terms is useful for many isotopes where one of these terms is considerably larger than the

[5] 1 barn = 1×10^{-24} cm^2.

other, it may still be complicated to interpret for isotopes where the incoherent and coherent cross-sections are similar. That is one probe the sum of the coherent and incoherent scattering, where the coherent contains both self and cross terms, whilst the incoherent contains the self terms only [171].

The double differential cross section can conveniently be written as

$$\frac{\mathrm{d}^2\sigma}{\mathrm{d}\Omega \mathrm{d}E_\mathrm{f}} = \frac{k_f}{4\pi k_i}\left[\sigma_\mathrm{coh} S_\mathrm{coh}(\mathbf{q}, E) + \sigma_\mathrm{inc} S_\mathrm{inc}(\mathbf{q}, E)\right], \tag{4.8}$$

where $S_\mathrm{coh}(\mathbf{q}, E)$ and $S_\mathrm{inc}(\mathbf{q}, E)$ are the coherent and incoherent dynamical structure factors, respectively. As it turns out, the dynamical structure factors are very useful quantities and are what are normally analyzed in neutron scattering experiments. Further, the incoherent and coherent dynamical structure factors are the Fourier transforms in space and time of the self and pair correlation functions $G_\mathrm{s}(\mathbf{r}, t)$ and $G(\mathbf{r}, t)$, respectively [173]. Consequently, the coherent and incoherent scattering gives information about correlations between different nuclei at different times and on self-correlations, respectively.

4.2 Inelastic neutron scattering

Inelastic scattering refers to events where the neutron exchanges energy with the probed material. The neutron can both create and annihilate excitations with energy E, leading to neutron energy loss and gain, respectively[6]. Clearly, the scattering by the annihilation of excitations is heavily dependent on their population, *i.e.* on temperature. The neutrons can scatter by phonons through nuclear interaction or by magnetic excitations via magnetic interactions. In this thesis, only nuclear scattering will be considered. Further, neutrons can interact with particles performing stochastic motions (diffusion or rotation), leading to so-called *quasielastic scattering*, as will be discussed in detail in section 4.3. A schematic sketch of the elastic, quasielastic, and inelastic scattering components, as can be measured in a neutron scattering experiment, is illustrated in Figure 4.2. The inelastic peaks occur at non-zero energy transfer values, and in the case of phonon scattering, they occur at energy transfer values corresponding to the energy of the vibrational motion. Thus INS can be used to study the vibrational dynamics of materials. A particular advantage of INS over the commonly applied Raman and infrared (IR) spectroscopies is that no optical selection rules apply; thus, in principle, all modes are measurable [174] (though their intensity depends on the neutron scattering cross section). In addition, neutron scattering allows measurements of a wide range of wavevectors and can give access to the (neutron cross-section-weighted) vibrational density of states. Below, I will discuss the neutron scattering of phonons (vibrational motions) in more detail.

[6]This is commonly referred to as Stokes and anti-Stokes scattering, respectively.

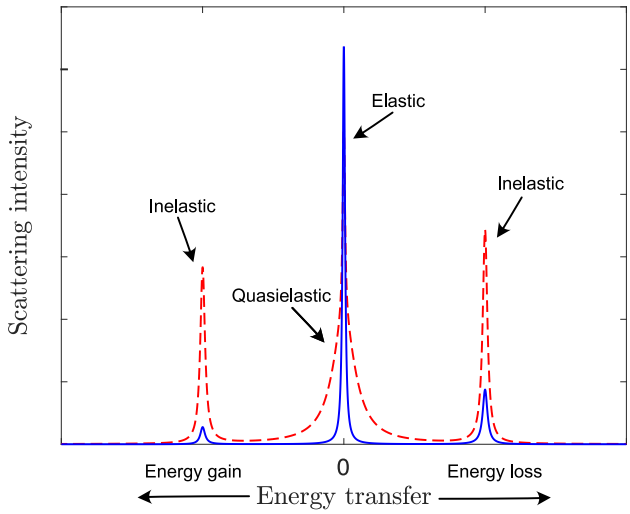

Figure 4.2: Schematic sketch of the elastic, quasielastic, and inelastic scattering components in a neutron scattering experiment. The dashed red and solid blue lines indicate measurements at high and low temperatures, respectively. The quasielastic scattering refers to the broadening of the elastic peak, which occurs at $E = 0$. The inelastic peaks occur at non-zero energy transfer values. The intensities of the inelastic peak at the neutron energy gain side depend heavily on temperature. At low temperatures, only inelastic scattering on the neutron energy loss side can be observed because there is no thermal population of the excitations.

4.2.1 Phonon scattering

In this thesis, most studied materials contain a relatively large amount of H. Because of the large incoherent cross section of H, the coherent scattering can then be neglected, *i.e.* $S(q, E) \approx S_{\text{inc}}(q, E)$. For incoherent scattering by one phonon, it can be shown that the expression for the double differential cross section can be written in terms of the phonon density of states $g(\omega)$ as [175]

$$\left(\frac{\mathrm{d}^2\sigma}{\mathrm{d}\Omega \mathrm{d}E_\mathrm{f}}\right)_{\text{inc}}^{\text{1-phonon}} = \frac{\sigma_{\text{inc}}}{4\pi}\frac{1}{12M}\frac{k_f}{k_i}e^{-2W(q)}q^2\frac{g(\omega)}{\omega}\left[\coth\left(\frac{\hbar\omega}{2k_\mathrm{B}T}\right)\pm 1\right], \tag{4.9}$$

where M is the mass of the vibrating atom, $\omega = E/\hbar$, and $e^{-2W(q)}$ is the so-called Debye-Waller factor. The factor $\coth(\hbar\omega/2k_\mathrm{B}T) \pm 1$ stands for the Bose-Einstein population factor for phonon creation and annihilation, respectively. Thus, for a given q, all modes whose energy satisfies $\hbar\omega = E$ contribute to the scattering. The 1-phonon incoherent scattering is thus proportional to the phonon density of states and can be used to derive a so-called generalized density of states (GDOS) from the

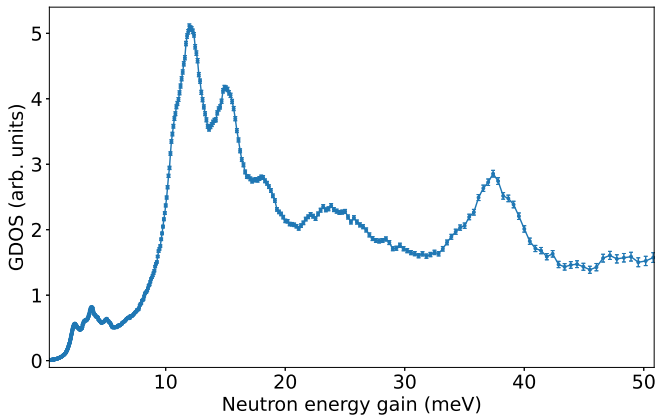

Figure 4.3: GDOS of a powder sample of $MAPbI_3$ at $T = 100$ K, as extracted from neutron time-of-flight data obtained at IN5 at the ILL.

experiment. The GDOS, $G(\omega)$, is a weighted sum and can be written as [175]

$$G(\omega) = \sum_i \frac{\sigma_{\text{inc}}^{(i)}}{4\pi} \frac{1}{M_i} e^{-2W_i(q)} g_i(\omega), \tag{4.10}$$

where the index i refers to the properties of atom i in the unit cell, and the sum runs over all atoms in the unit cell. The difference between the GDOS and the real phonon density of states is that the different atomic contributions in the GDOS are weighted by σ_i/m_i where σ_i and M_i are the scattering cross section and mass, respectively, of atom i [176]. The GDOS also contains the contribution from the Debye-Waller factors, which generally are not known but can, in principle, be calculated according to [176]

$$W_i(q) = \frac{\hbar q^2}{2M_i} \int_0^\infty \frac{g_i(\omega)}{\omega} [2n(\omega) + 1] \mathrm{d}\omega. \tag{4.11}$$

Figure 4.3 shows the GDOS extracted from inelastic neutron scattering of a powder sample of $MAPbI_3$ at $T = 100$ K. Note that because of the large incoherent scattering cross section of H, and the low mass of the MA organic cation compared to Pb and I, the GDOS will be dominated by vibrations related to the organic cation. The GDOS is featured by several sharp peaks corresponding to the molecular librations of the MA organic cation in $MAPbI_3$ [50, 53].

For coherent scattering, there is, in addition, an interference condition on the neutron wavevector (momentum conservation). The coherent one-phonon cross

section is given by [169]

$$\left(\frac{\mathrm{d}^2\sigma}{\mathrm{d}\Omega \mathrm{d}E_\mathrm{f}}\right)_{\mathrm{coh}}^{\text{1-phonon}} \propto \frac{k_f}{k_i}\sum_{s,\tau}\frac{1}{\omega_s}\left|\sum_d \frac{\bar{b_d}}{\sqrt{M_d}}\exp(-W_d)\exp(\mathrm{i}\mathbf{q}\cdot\mathbf{d})(\mathbf{q}\cdot\mathbf{e}_{ds})\right|^2 \times\left[\langle n_s+1\rangle\,\delta(\omega-\omega_s)\delta(\mathbf{q}-\mathbf{k}-\tau)+\langle n_s\rangle\,\delta(\omega+\omega_s)\delta(\mathbf{q}+\mathbf{k}-\tau)\right], \quad (4.12)$$

where $\mathbf{e}_{ds}$ is the phonon polarization vector, $\mathbf{k}$ the phonon wavevector, τ a reciprocal lattice vector, n_s denotes the Bose-Einstein thermal population factor, and the index d runs over all atoms in the unit cell with position vector $\mathbf{d}$. The term with $\langle n_s+1\rangle$ and $\langle n_s\rangle$ describes a phonon creation and annihilation process, respectively. An example of coherent phonon scattering is shown in Figure 4.4, which shows the $S(q,\omega)$ measured on a powder sample of $CsPbBr_3$. $CsPbBr_3$ is almost a purely coherent scatterer, which is reflected in the experimental data, which shows a complex q-dependence of the inelastic scattering. Shown in Figure 4.4 is also the simulated powder averaged $S(q,\omega)$ based on phonon scattering. This was calculated based on the phonon eigenvectors and frequencies from harmonic phonon calculations taken from the Phonon database at Kyoto University [177]. $S(q,\omega)$ was simulated using the OCLIMAX code [178], taking into account both coherent and incoherent scattering, which then can reproduce the experimental data relatively well.

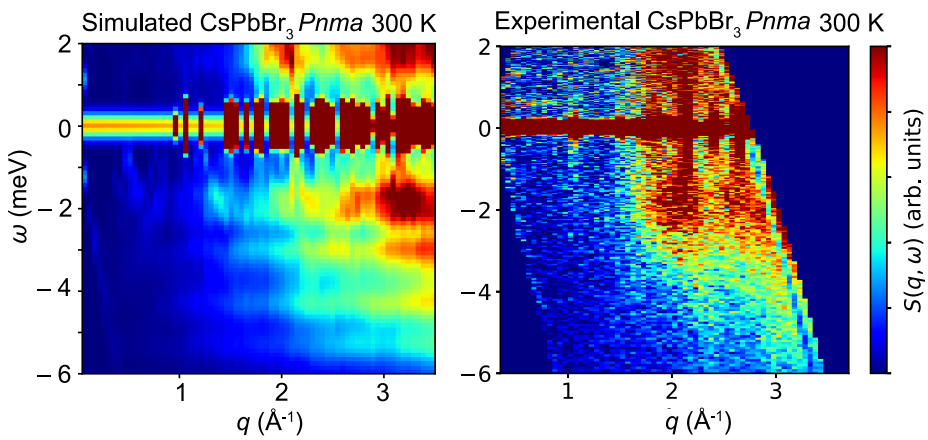

Figure 4.4: (Left panel) Simulated $S(q,\omega)$ from harmonic phonons of $CsPbBr_3$ in the orthorhombic phase (space group *Pnma*). The phonon calculations were obtained from the Phonon database at Kyoto University [177], and $S(q,E)$ (both coherent and incoherent parts) was simulated from the phonon eigenvectors and eigenfrequencies using Oclimax [178]. (Right panel) Experimental $S(q,\omega)$ at $T = 300$ K of a powder sample of $CsPbBr_3$ measured on FOCUS at the PSI using an incident neutron wavelength of 4 Å.

4.2.2 Modelling functions and phonon damping

Phonon scattering is typically described as a damped harmonic oscillator (DHO) model [179]

$$S(q,E) \propto \frac{[n(E)+1]4E\,\Gamma_i/\pi}{(E^2-\omega_i^2)^2+4E^2\Gamma_i^2}, \tag{4.13}$$

where $n(E)$ is the Bose-Einstein population factor, Γ_i is the damping factor, and ω_i is the phonon frequency. This describes a phonon with a lifetime given by the inverse of the damping factor $\tau_i = \hbar/\Gamma_i$. For overdamped modes, one has that the damping factor is larger than the phonon frequency ($\omega_i < \Gamma_i$) [180]. Physically, this means that the phonon will decay before it has completed one oscillation period, and the dynamics can thus no longer be described as a vibration but rather a relaxation. In that case, the spectral function becomes almost indistinguishable from a single Lorentzian centred around zero energy transfer

$$S(q,E) \propto \frac{\gamma}{\gamma^2+E^2}. \tag{4.14}$$

This spectral function describes relaxational dynamics with a relaxational time $\tau = \hbar/\gamma$. The transition from phonon modes to relaxational dynamics is shown in Figure 4.5, which shows the calculated response function of a DHO for various values of the damping factor. For the overdamped harmonic oscillator, the linewidth of the Lorentzian will decrease as the damping factor increases (the other way, as for the underdamped case).

4.2.3 Vibrational spectroscopy

In chemistry and related fields, INS is commonly used as vibrational spectroscopy, similar to the more standard techniques of Raman and infrared (IR) spectroscopy. The main advantage of INS is that there are no optical selection rules, and thus all modes are, in theory, possible to measure. However, one may note that their relative intensity depends strongly on the neutron scattering cross-section. This is illustrated in Figure 4.6, which compares, as an example, the vibrational spectra of $MAPbI_3$ and $FAPbI_3$ measured using INS and IR spectroscopy. As can be seen, there are more modes observed in the INS spectra as compared to the IR spectra. However, one should note that these INS measurements, which were done on the TOSCA spectrometer, are not very sensitive to the higher energy transfer values. TOSCA is designed to measure a broad range of energy transfer values and does so by measuring at specific fixed scattering angles. This leads to that one measure on a line in (q, E) space, and generally, no information on the q-dependence can be obtained. However, higher energy transfer values are measured at higher q and will have a heavily reduced intensity of the Debye-Waller factor contribution. For molecular vibrations, the modes are mostly localized in nature (no phonon dispersion), and thus there is commonly no interesting q-dependence of the scattering signal.

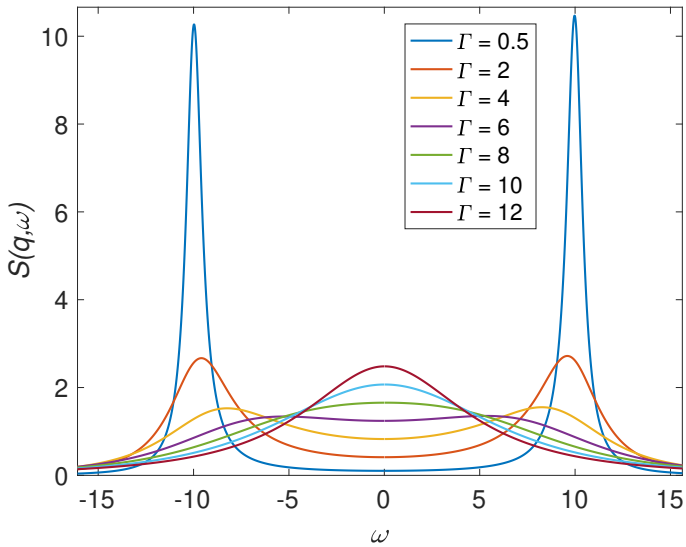

Figure 4.5: The DHO response function plotted for various damping factors, showcasing the transition from underdamped to overdamped phonons. It is plotted with $\omega_i = 10$. Note that $E = \hbar\omega$ and E and ω are used interchangeably herein.

4.3 Quasielastic neutron scattering

Quasielastic neutron scattering (QENS) refers to the broadening of the elastic line which occurs due to interactions between the neutrons and atoms in the sample performing translational and/or reorientational diffusional dynamics on the timescale $\hbar/\Delta E$, where ΔE is the energy broadening [171, 181]. As it turns out, QENS is most easily understood in terms of correlation functions in space and time, and this description is originally due to Van-Hove [173]. In this thesis, most studied materials contain H, and because of the large incoherent cross-section of H, the quasielastic coherent scattering can be safely neglected. Thus, only the incoherent quasielastic scattering is considered in what follows. As seen above, the incoherent neutron scattering is determined by the incoherent dynamical structure factor $S_{\text{inc}}(\mathbf{q}, E)$, which is the Fourier transform in both space and time of the self-correlation function $G_s(\mathbf{r}, t)$. $[G_s(\mathbf{r}, t)\,\mathrm{d}^3 r]$ gives the probability that given a particle at the origin at $t = 0$, the same particle is in the volume $d^3 r$ at position $\mathbf{r}$ and at time t [171]. The Fourier transform in space of $G_s(\mathbf{r}, t)$ yields the self-part of the so-called intermediate scattering function $I_s(\mathbf{q}, t)$, and the Fourier transform of $I_s(\mathbf{q}, t)$ in time yields the dynamical structure factor $S_{\text{inc}}(\mathbf{q}, E)$ which is what is commonly[7] obtained in an (incoherent) QENS experiment.

[7] In neutron spin-echo spectroscopy, one measures the intermediate scattering function $I(\mathbf{q}, t)$, rather than $S(\mathbf{q}, E)$.

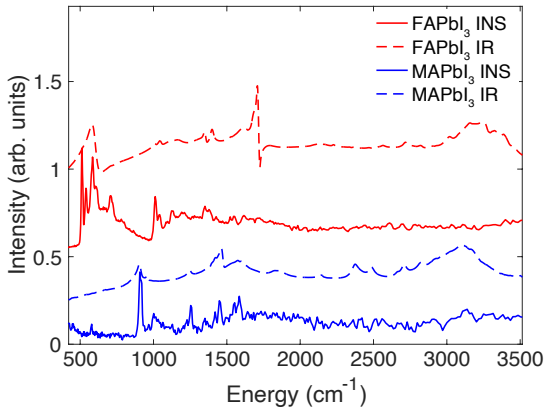

Figure 4.6: INS spectra (measured at 10 K using the TOSCA instrument) [50] and IR absorbance spectra measured at room temperature for $MAPbI_3$ and $FAPbI_3$. The spectra have been vertically separated for clarity.

A useful characteristic of QENS is that it is possible to separate the cases of long-range (translational) and localized (restricted) diffusion. For localized diffusion, there is a finite probability that the particle will be at the original position at $t \to \infty$. This means that $I_s(q,t)$ will have a non-zero value at $t \to \infty$. In turn, after a Fourier transform in time, this leads to a separate elastic component for $S_{\text{inc}}(\mathbf{q}, E)$. The typical behaviour for $S_{\text{inc}}(\mathbf{q}, E)$ and $I_s(q,t)$ for localized and long-range diffusional motions is schematically illustrated in Figure 4.7. These two cases will be discussed separately in what follows.

4.3.1 Long-range translational diffusion

In the macroscopic limit (large distances, corresponding to small q-values in reciprocal space), the self-correlation function obeys the standard diffusion equation $\partial_t G_s(r,t) = D\nabla^2 G_s(r,t)$, with the initial condition $G(r, t=0) = \delta(r)$ and where D is the (self) diffusion coefficient [171]. The solution to this equation can be written as [171]

$$G_s(r,t) = \frac{1}{(4\pi D\,|t|)^{3/2}} \exp(-r^2/4D|t|).$$

The Fourier transform of this function yields the following $I_s(q,t)$ and $S_{\text{inc}}(q,E)$:

$$I_s(q,t) = \exp(-q^2 D|t|) \tag{4.15}$$

$$S_{\text{inc}}(q,E) = \frac{1}{\pi} \frac{\hbar D q^2}{(\hbar D q^2)^2 + E^2}. \tag{4.16}$$

Thus, $S_{\text{inc}}(q,E)$ is a single Lorentzian function with linewidth (HWHM) $\hbar D q^2$. This law is generally true for small q, but for larger q the details of the diffusion mechanism

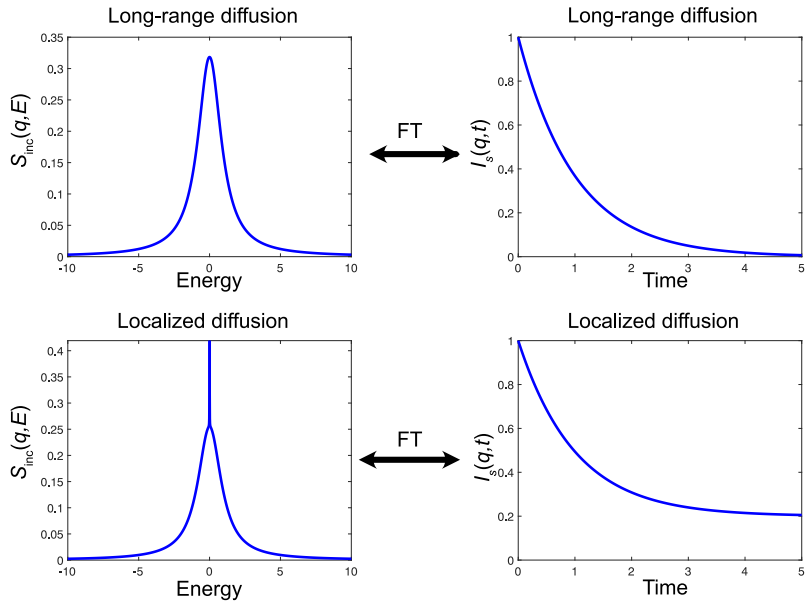

Figure 4.7: Schematic illustrations of the $S_{\mathrm{inc}}(q, E)$ and $I_{\mathrm{s}}(q, t)$ for long-range and localized (restricted) diffusion. The $S_{\mathrm{inc}}(q, E)$ and $I_{\mathrm{s}}(q, t)$ are related by a Fourier transform (FT).

become important. In particular, for jump diffusion in solids, the linewidth at higher q must mimic the jump rate, as will be explained below.

A common model for diffusion on a lattice is the Chudley-Elliot model, which considers jump diffusion in a Bravais lattice where the particle stays a mean residence time τ on a site before an instantaneous jump to a nearest neighbouring site. The results for $I_s(q, t)$ and $S_{\mathrm{inc}}(\mathbf{q}, E)$ are the following [171, 182]

$$I_s(\mathbf{q}, t) = \exp\left[-\frac{t}{N\tau}\sum_{j}^{N}(1 - e^{-\mathrm{i}\mathbf{q}\cdot\ell_j})\right] \tag{4.17}$$

$$S_{\mathrm{inc}}(q, E) = \frac{1}{\pi}\frac{\gamma(\mathbf{q})}{\gamma(\mathbf{q})^2 + E^2}, \tag{4.18}$$

and the linewidth (HWHM) $\gamma(\mathbf{q})$ is in this case given by

$$\gamma(\mathbf{q}) = \frac{\hbar}{N\tau}\sum_{j=1}^{N}\left[1 - e^{-\mathrm{i}\mathbf{q}\cdot\ell_j}\right], \tag{4.19}$$

where the sum runs over all nearest neighbour sites with position vectors ℓ_j with N being the number of nearest neighbours. For small q, Eq. (4.19) gives the macroscopic

limit $\gamma \to \hbar D q^2$. Whilst for larger q, γ approaches the jump rate, $\gamma \to \hbar/\tau$. For studies of polycrystalline samples, no information of the direction of $\mathbf{q}$ can be obtained, and it is then common to approximate the powder averaged scattering signal by using an isotropic average over all directions of $\gamma(\mathbf{q})$. The jump length is then assumed identical for all sites and thus becomes an "effective" quantity d. The isotropically averaged linewidth then becomes [171, 182]

$$\gamma(q) = \frac{\hbar}{\tau}[1 - j_0(q\,d)], \tag{4.20}$$

where $j_0(x) = \sin(x)/x$ is the zeroth-order spherical Bessel function. Still, it should be noted that this is only approximately correct and, in principle, the powder average should be performed over the whole $S_{\mathrm{inc}}(\mathbf{q}, E)$ [171].

4.3.2 Localized diffusion

Localized diffusion can also be studied using QENS. This can, for example, be localized rotational/reorientational motions of molecules or molecular groups in solid phases, as is studied in Papers I and V of this thesis. For localized (or restricted) diffusion, there is a finite probability that the particle is present at the original position when $t \to \infty$. This means that $I_s(q, t)$ will not decay to zero, but to a finite value, for $t \to \infty$. After the Fourier transform, this yields an intrinsic elastic component in $S_{\mathrm{inc}}(q, E)$, see Figure 4.7. The relative intensity of this elastic component is commonly referred to as the elastic incoherent structure factor (EISF), and the q-dependence of the EISF can be used to gain information on the spatial geometry of the localized dynamics. The EISF is the limit of $I_s(q, t)$ as $t \to \infty$ and can be calculated as [171]

$$\mathrm{EISF} = \frac{1}{N^2}\left|\sum_{j=1}^{N} e^{\mathrm{i}\mathbf{q}\cdot\mathbf{r}_j}\right|^2, \tag{4.21}$$

where $\mathbf{r}_j$ $j = 1, \ldots N$ is the sites the particle can visit. Consequently, the EISF for jump rotation over any arrangement of discrete sites can be calculated [171, 181]. For powder samples, the results obtained from Eq. (4.21) have to be spatially averaged over all directions.

Experimentally, the EISF can be estimated by determining the ratio of elastic to elastic plus quasielastic scattering intensity *i.e.*

$$\mathrm{EISF} = \frac{I_{\mathrm{el}}}{I_{\mathrm{el}} + I_{\mathrm{qe}}},$$

where I_{el} and I_{qe} is the elastic and quasielastic scattering intensity, respectively. A common "model-free" approach for determining the geometry of localized motions by

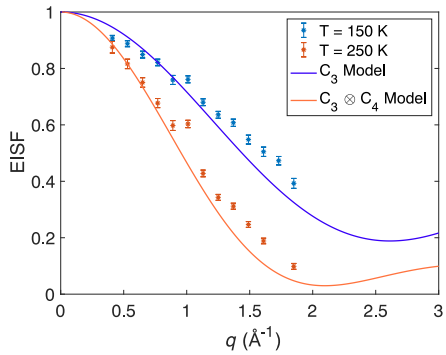

Figure 4.8: EISF of $MAPbI_3$ at 150 K and 250 K from QENS data obtained on the IN6 spectrometer at the ILL. The Figure is reprinted with permission from Paper I [102].

QENS is thus to fit the QENS data to a model function of the following form

$$S(q,E) \propto \left[I_{\mathrm{el}}\,\delta(E) + \sum_i I_{\mathrm{qe}}^{(i)}\,\mathcal{L}(E;\gamma_i) \right] \circledast R(q,E) + \mathrm{bkg}(q,E), \tag{4.22}$$

where the Dirac delta function ($\delta(E)$) describes the elastic scattering with intensity I_{el} and where one or several Lorentzian functions $\mathcal{L}(E;\gamma_i)$ with linewidth (HWHM) γ_i describes the quasielastic scattering, with total intensity $I_{\mathrm{qe}} = \sum_i I_{\mathrm{qe}}^{(i)}$. $\mathrm{bkg}(q,E)$ is a background function that usually is described as a linear function of energy. The elastic and quasielastic parts are convoluted by the function $R(q,E)$, which describes the instrument resolution function. The fraction of elastic scattering can then be derived as a function of q, which can then be compared to different jump-diffusion models describing localized diffusion. An example of this approach is shown in Figure 4.8, which shows the EISF of $MAPbI_3$ extracted from QENS fitting at 150 K and 250 K. The data is compared to two different models. The C_3 model describes the three-fold rotation of the methyl and ammonia groups around the C−N axis. The $C_3 \otimes C_4$ describes a combined C_3 rotation of the methyl/ammonia groups and a four-fold rotation of the whole MA molecule, as was described by Chen *et al.* [27]. As can be seen, the data in the orthorhombic phase at 150 K is in good agreement with the C_3 model. The data at 250 K, however, is manifested by a larger portion of quasielastic scattering (smaller EISF values) than what the C_3 model predicts and is in good agreement with the $C_3 \otimes C_4$ model (see Paper I for details) [102].

Chapter 5

Experimental considerations

5.1 Neutron time-of-flight spectroscopy

[1]A common technique for inelastic neutron scattering is neutron time-of-flight spectroscopy. As examples, both IN5 and IN6 at the Institut Laue-Langevin (ILL) located in Grenoble, France, which were used in this thesis, are time-of-flight (TOF) spectrometers. The basic idea in TOF spectroscopy is that the neutron energy is measured by measuring the time it takes for the neutron to cover a well-defined distance. If the time and distance are known, the neutron velocity can be determined, and from the neutron velocity, one can calculate the corresponding energy. There are two types of TOF spectrometers, called direct geometry spectrometers and indirect geometry spectrometers. In a direct geometry spectrometer, the incident energy is fixed, whilst, for an indirect geometry spectrometer, the final neutron energy is fixed. For simplicity, a direct geometry spectrometer is only considered here, which is the most simple technical setup to understand.

In a direct geometry spectrometer, the beam has first to be monochromatized and pulsed (in order to set the incident 'time' of the neutrons). This can be done in several ways. For example, on the TOF spectrometer IN6 at the ILL, diffraction of a well-known single-crystal is used for monochromatizing the beam, which is then pulsed by using a series of rotating disks called choppers. The choppers are made from a neutron-absorbing material with transparent slits that allow the creation of a pulsed beam. Another method is used on the TOF spectrometer IN5 at the ILL, where the beam is both monochromatized and pulsed using disk choppers. After the beam has been pulsed and monochromatized, the time it takes for the neutron to reach the detector can then be used to measure its energy. The wavevector of the scattered neutron is measured by having detectors at different positions, which are translated into various scattering angles. An illustration of the TOF spectrometer

[1]This chapter is partly based on my Licentiate thesis.

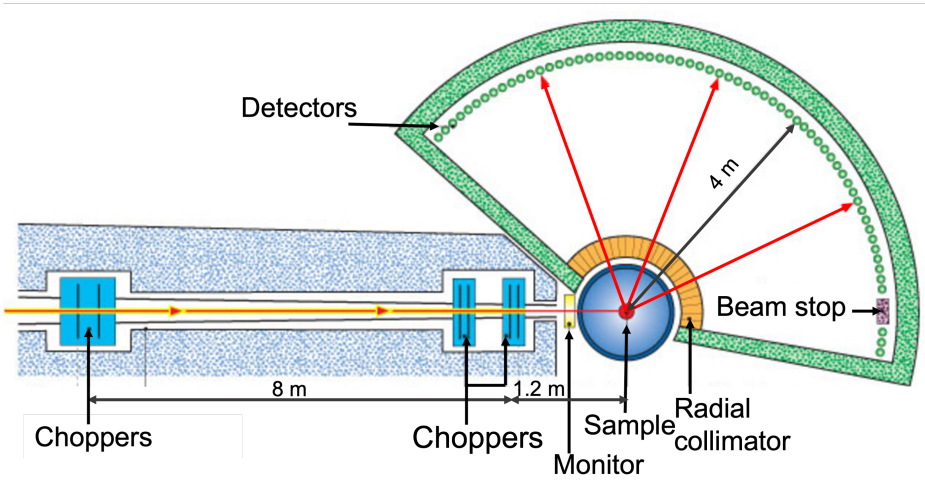

Figure 5.1: Schematic sketch of the direct-geometry time-of-flight spectrometer IN5 at the ILL, Grenoble, France. The figure was adapted from [183], courtesy of the Institut Laue-Langevin.

IN5, which can be considered a prototypical direct-geometry TOF spectrometer, is shown in Figure 5.1

The recorded raw data in a TOF experiment, $N(2\theta, \mathrm{TOF})$, thus contains the number of counted neutrons as a function of their TOF and scattering angle 2θ (Figure 5.2). It is, therefore, necessary to reduce the raw data and apply different corrections in order to obtain the wanted dynamical structure factor $S(q, E)$, which, ideally, is method-independent *i.e.* only contains information of the studied material. In this thesis, the data reduction performed for neutron TOF experiments was done in the following steps. Since the number of counts depends on the measurement time, it was normalized to the monitor count. The neutron monitor is placed before the sample and is essentially a neutron detector with low efficiency, so most neutrons pass through it. The variation in the efficiency of the detectors was accounted for by normalizing to measurements of a vanadium sample. Vanadium scatters almost purely incoherently, $\sigma_{\mathrm{coh}} \approx 0.0184$ barn and $\sigma_{\mathrm{inc}} \approx 5.08$ barn, and the scattering of V is thus roughly isotropic. This normalization is done by integrating the vanadium measurement over time-of-flight channels around the elastic peak and then dividing by this for each detector, *i.e.*

$$N(2\theta, \mathrm{TOF}) \rightarrow \frac{N(2\theta, \mathrm{TOF})}{\int_{\text{elastic peak}} d\mathrm{TOF}\ N_{\mathrm{Vanadium}}(2\theta, \mathrm{TOF})}.$$

Measurements on an empty sample cell should be subtracted in order to remove the scattering from the sample holder and cryostat and possibly from other parts of

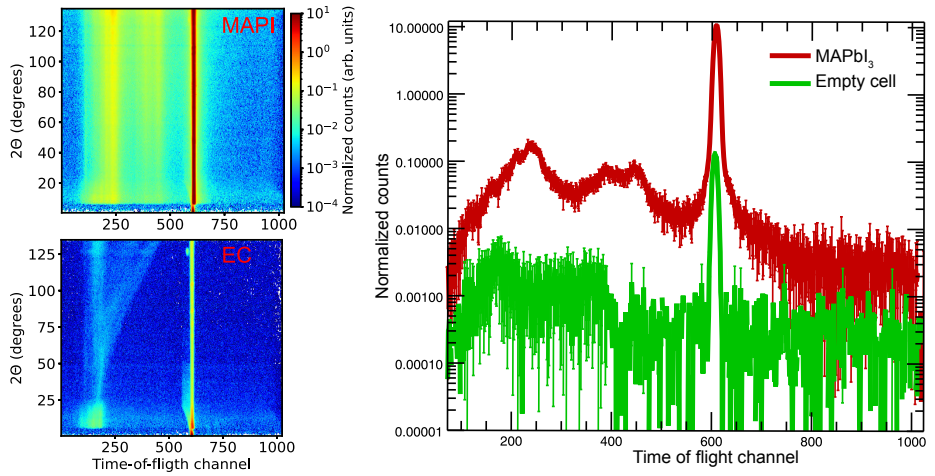

Figure 5.2: Raw time-of-flight data from IN5 measured with an incident neutron wavelength of 5 Å, of $MAPbI_3$ and the empty sample cell (EC) at $T = 100$ K showing the scattering data as a function of scattering angle and time-of-flight channel (time). The right panel shows the time-of-flight spectra for $2\theta = 115°$.

the instrument. The empty cell measurements also need before this subtraction to be normalized to monitor count and a vanadium standard. The neutron detector's efficiency also depends on the neutron energy and corrections for this need to be applied to the data. For the cases of IN6 and IN5, special empirical relations can be used that are implemented in the data analysis software LAMP [184] can be used to do this. The result is then related to the double differential cross section $d^2\sigma/d\Omega d\mathrm{TOF}$ (number of neutrons per time scattered into the solid angle $d\Omega$ and with time-of-flight in the range $d\mathrm{TOF} + \mathrm{TOF}$). This is still measured as a function of the time-of-flight and scattering angle and needs to be converted to the (q, E) domain. The wave vector transfer q is related to the scattering angle and energy transfer according to

$$q^2 = |\mathbf{k}_i - \mathbf{k}_f|^2 = k_i^2 + k_f^2 - 2\,k_i\,k_f\,\cos\theta = \frac{2m}{\hbar^2}\left(E_i + E_f - 2\sqrt{E_i E_f}\cos\theta\right). \quad (5.1)$$

Hence, q depends on both the scattering angle and the energy transfer non-linearly. Therefore one scattering angle does not correspond to one q, but it changes with energy transfer. The TOF instrument thus probes a curved region of the (q, E) space. Figure 5.3 shows an illustration of the data reduction steps in TOF spectroscopy. Note that once converted to the (q, E) domain, the probed domain is curved. The maximum energy loss is roughly 2 meV in this case of 5 Å incident wavelength neutrons and is determined by the incident neutron energy (the neutron cannot lose more energy than it has). In experiments, it is, however, lower than the incident neutron energy because otherwise, the slowest neutrons (those that lose much energy in the scattering process) will overlap with the fastest neutrons in the next neutron pulse. The maximum energy gain is, in principle, unlimited. However, it is, in the

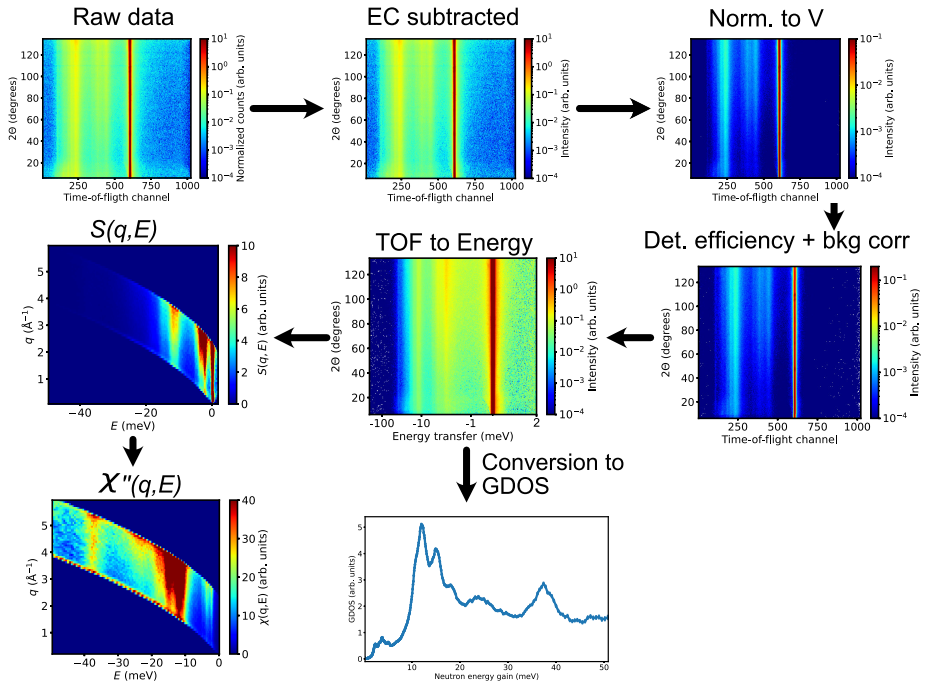

Figure 5.3: Illustration of some data reduction steps for conversion from the raw neutron TOF data to the measured dynamical structure factor $S(q, E)$, the GDOS, or the dynamic susceptibility $\chi''(q, E)$ which is related to the dynamical structure factor by a correction for the Bose population *i.e.* $S(q, E) = (1/\pi)[1 + n(E)]\chi''(q, E)$, where $n(E) = [\exp(E/k_bT) - 1]^{-1}$ denotes the Bose-Einstein population factor. The plot of $\chi''(q, E)$ shows the absolute value of $\chi''(q, E)$, which otherwise is an odd function of energy. The TOF data was taken on a powder sample of $MAPbI_3$ at 100 K using an incident neutron wavelength of 5 Å on IN5 at the ILL. Note that the conversion to the GDOS involves averaging over a certain q-range

same way, limited by the time between neutron pulses so that the fastest neutrons do not overlap with the slowest neutrons in the previous pulse; in Figure 5.3, it is only shown up to -50 meV after conversion to $S(q, E)$. After this treatment, the measured dynamical structure factor $S(q, E)$ is convoluted with the instrumental resolution function $R(q, E)$. For the purpose of QENS analysis, the instrumental resolution function is usually determined by measurements of the sample at a low temperature (2 K) where all dynamics are assumed to be frozen-in (no quasielastic scattering), or by measurements of a vanadium sample which does not exhibit any quasielastic scattering. Further corrections of the data might include multiple scattering corrections and corrections for absorption and self-shielding of the sample.

5.2 Neutron backscattering spectroscopy

Neutron backscattering spectroscopy is a technique which is featured by an extremely high resolution of the energy transfer, normally better or around 1 μeV. The backscattering technique is based on the fact that for Bragg scattering angles close to 90°, the uncertainty in the Bragg scattered wavelength $\Delta\lambda$ becomes very small. This can be seen by differentiating Bragg's law $\lambda = 2d\sin\theta$:

$$\frac{\Delta\lambda}{\lambda} = \frac{\Delta d}{d} + \cot\theta\,\Delta\theta, \tag{5.2}$$

where $\Delta\theta$ is the uncertainty in angle, *i.e.* the divergence of the beam. $\Delta d/d$ is the relative uncertainty in lattice spacing and is mainly related to the quality of the crystal. For $\theta = 90°$ the second term in Eq. (5.2) vanishes, meaning that $\Delta\lambda/\lambda$ is the smallest and is independent, to first order, of the divergence of the beam [185]. The backscattering technique thus uses a Bragg scattering angle close to 90° for the selection and for the analysis of the energy of the neutrons in order to achieve the highest possible resolution [185].

An illustration of the neutron backscattering spectrometer IN16B at the ILL, which has been used in this thesis, is shown in Figure 5.4. The basic operation of this instrument will be described below. First, the neutron velocity band is selected in a velocity selector. The background chopper pulses the beam, which is then deflected onto a Doppler monochromator. The Doppler monochromator consists of high-quality silicon crystals mounted on a so-called Doppler drive, a device allowing the monochromator to move forwards and backwards. 90° Bragg scattering from monochromator crystals selects neutrons with a wavelength of 6.271 Å for Si(111) crystals or 3.275 Å if using the Si(311) crystals [186, 187]. The selected neutron wavelength is allowed to vary by varying the speed of the Doppler drive because the energy of the Bragg scattered neutrons depends on the relative speed of the neutrons and the Doppler drive through the Doppler shift. The Bragg scattered neutrons travel back towards the sample position through slits in the rotating deflector. During this time, the background chopper is closed, allowing it to significantly reduce the background. This leads to a pulsed beam of neutrons, with an energy band determined by the Doppler drive frequency. After the neutrons are scattered by the sample, the backscattering condition at the analyzer crystals selects only those neutrons with certain final energy fulfilling the Bragg condition, which then is counted at the detectors [186, 187]. Thus, IN16b can be considered as an indirect geometry spectrometer where the final energy is determined by Bragg scattering of the analyzer crystal, whilst the incident energy is varied in a known way by the Doppler drive.

Depending on how the Doppler drive is set up, different measurement types are possible. If the Doppler drive frequency is set to zero, only the elastically scattered neutrons reach the detector. This mode can be used to measure the elastic intensity as a function of temperature, which can provide information about the mean squared

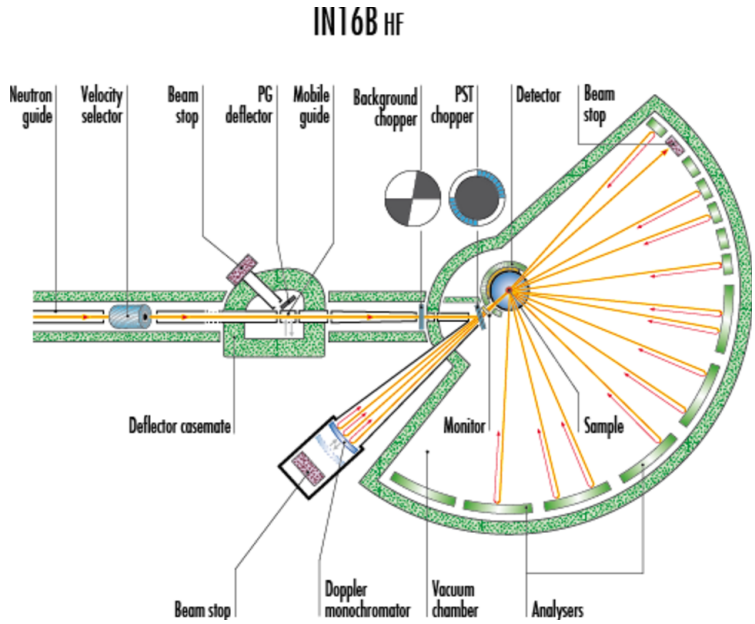

Figure 5.4: Schematic sketch of the IN16B backscattering spectrometer at the ILL, in its high flux configuration. The figure was taken from [187], courtesy of the Institut Laue-Langevin.

displacement of the atoms in the studied material as a function of temperature and qualitative information on relaxational dynamics in the sample (*i.e.* in which temperature range the dynamics is accessible to the instrument timescales). This measurement mode is usually called an elastic fixed window scan. On IN16B, by setting the Doppler drive to follow a certain velocity profile, it is also possible to perform inelastic fixed window scans, where the intensity is recorded at a fixed energy transfer value which is non-zero [188]. For normal QENS measurements, the Doppler drive is moved with a periodic velocity profile, which allows for obtaining an energy spectrum. The maximum accessible energy transfer is typically in the range $10 - 100$ μeV and is determined by the maximum velocity of the Doppler drive.

Chapter 6

Results and discussion

6.1 Metal halide perovskites

This section summarizes and discusses the results on metal halide perovskites, which are reported in Papers I – VI.

6.1.1 Organic cation dynamics in formamidinium lead iodide perovskites (Paper I)

As described in the earlier sections, the rotational organic cation dynamics in MHPs are relevant for their optoelectronic properties [10], and in particular, the organic cation dynamics in FA-based systems are much less understood [66], compared to the more well studied $MAPbI_3$ [27] and $MAPbBr_3$ [88]. To improve the understanding of the organic cation dynamics in $FAPbI_3$, QENS was used in order to directly probe the rotational dynamics of the FA cations on the ns−ps timescales in all three crystallographic phases of perovskite $FAPbI_3$.

Measurements on IN16B with the Si(311) analyzers, probing timescales in the range ~ 20 ps $-$ 300 ps, were performed in order to probe the slow timescale dynamics in the low-temperature tetragonal γ-phase. Figure 6.1 shows the elastic and inelastic fixed window scan (at 4 μeV and 10 μeV) (EFWs and IFWs) data measured upon cooling the cubic perovskite phase of $FAPbI_3$. The elastic scan reveals the onset of organic cation dynamics above around 50 K, and the IFWs show broad peaks between $\sim 75 - 150$ K. The IFWs were fitted to the expression for the expected intensity at an energy E for a single relaxational process following an Arrhenius behaviour of the relaxation time τ,

$$I(E,T) \propto \frac{\tau(T)}{1 + E^2\tau(T)^2/\hbar^2}, \tag{6.1}$$

where $\tau(T) = \tau_0 \exp(E_a/k_B T)$, and E_a is the activation energy of the dynamics [188]. The fits to the data give the temperature dependence of the corresponding quasielastic Lorentzian linewidth (FWHM) γ by $\tau(T) = 2\hbar/\gamma$, which, however, does not agree with the corresponding temperature dependence derived from the fitting of the QENS lineshape. This suggests that the FA cation dynamics in the γ phase are most likely complex and are not well described by a single relaxational process. This is in sharp contrast to the results for $MAPbI_3$, where the agreement between the IFWs and QENS lineshape fitting is much better; see Figure 6.1 (c-d). This supports the current understanding that the organic cation dynamics in the low-temperature orthorhombic phase of $MAPbI_3$ can be described by a single relaxational process related to the 3-fold rotation of the methyl and ammonia groups around the C−N axis [27]. The more complex dynamics observed for $FAPbI_3$ is most likely due to the disordered structure of the low-temperature γ-phase, where the FA cation orientations are believed to be disordered in an orientational glass [58, 66]. These disordered orientations of the FA cations could likely give rise to a distribution of relaxational times and activation energies, which could explain the broad peaks in the IFWs.

Faster timescale dynamics in the $\beta-$ and α-phases of $FAPbI_3$ were probed using neutron time-of-flight spectroscopy on the IN5 instrument. Typical QENS spectra in the $\beta-$ (200 K) and α-phases (300 K), as measured using an incident neutron wavelength of 5 Å together with total fits to the spectra, using two Lorentzian components to describe the QENS, are shown in Figure 6.2 (a). In the α-phase, there is almost no elastic scattering at sufficiently high q, which indicates very fast FA rotations and almost no preferred orientations in this phase. In order to assess the spatial geometry of the dynamics in more detail, the EISF was analyzed. Figure 6.2 (b) shows the EISF of $FAPbI_3$ as a function of temperature compared to different feasible jump models describing localized FA rotations. In the cubic α-phase, the site symmetry of FA is O_h. The most restricted dynamics to preserve this site symmetry is related to 12 sites where the C−H bond of FA can point towards any of the six cube faces and for each of these six orientations, there are two different orientations of the N$\cdots$N axis [62]. Another possibility is that the FA cation performs nearly isotropic rotations in the cubic phase, *i.e.* there are no preferred orientations of the FA cation, which have been suggested in another neutron diffraction study on a deuterated sample of $FAPbI_3$ [61]. Comparing the model calculations to the EISF data, it was found that in the cubic α-phase, at 300 and 350 K, the EISF could be well modelled using a model which describes the FA cation dynamics as isotropic rotations. One may note that the data show a slightly higher fraction of elastic scattering than predicted from the isotropic rotational model. This indicates that the FA rotations are almost, but not fully, isotropic in the cubic phase. In the tetragonal β phase, there is more elastic scattering, and the minimum of the EISF is shifted to slightly higher values of q. This is expected if there are some strongly preferred orientations of the FA cations in this phase. According to the structural model of the β-phase determined by Weber *et al.* [58], the space group is $P4/mbm$, and the site symmetry of the FA cation is D_{2h}, which only allow 2-fold rotations around the three principal

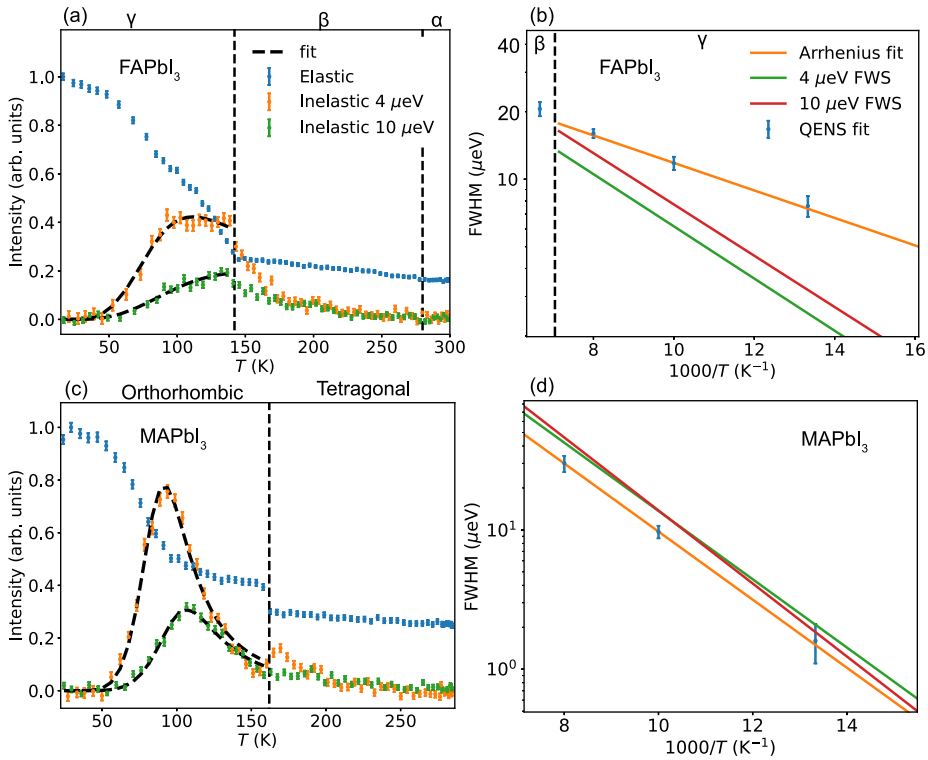

Figure 6.1: (a) Elastic and inelastic fixed window scans of $FAPbI_3$ as measured on IN16B. (b) Quasielastic linewidth (FWHM), as determined from both, fits to the IFWSs and QENS spectra. (c-d) Corresponding data for $MAPbI_3$. The Figures are reprinted with permission from Paper I [102].

axes of FA. It has previously been proposed based on NMR and DFT simulations that the main axis of rotation for FA in $FAPbI_3$ is around the N···N axis [66]. In the structure of β-$FAPbI_3$ by Weber *et al.*, the FA cations are disordered amongst four sites which are related through rotations around the N···N axis [58]. A comparison between the model describing rotations around the N···N axis between the sites from the structural model of Weber *et al.* [58] shows that more QENS was observed than predicted by this model, indicating that there are additional rotational modes present on the probed timescales. Taking into account also a 4-fold rotation about the C−H axis gives a model which is in reasonable agreement with the observed data. This thus indicates that, in the tetragonal β-phase, the FA cation performs rotations between preferred orientations, with the main rotational modes being rotations around the N···N and C−H axes.

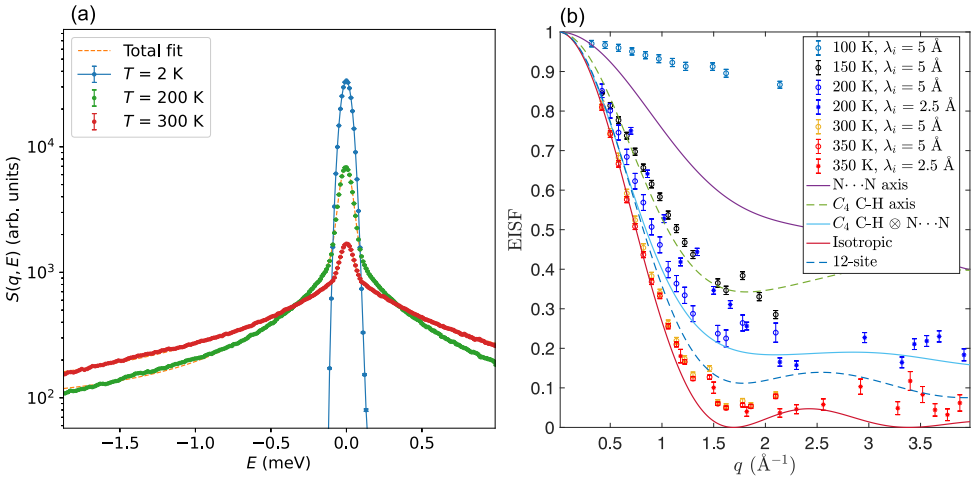

Figure 6.2: (a) Typical QENS spectra of $FAPbI_3$ in the $\beta-$ (200 K) and α-phases (300 K), as measured on IN5 (5 Å neutrons) together with total fits to the spectra, using two Lorentzian functions to describe the QENS. (b)EISF of $FAPbI_3$ as a function of temperature. The data is compared to different jump models describing localized FA cation dynamics around different possible rotational axes. The Figure is adapted with permission from Paper I [102].

The QENS studies were further expanded to include the MA-doped solid solution $MA_{0.4}FA_{0.6}PbI_3$, which was chosen due to the increased stability of the perovskite phase as compared to $FAPbI_3$ [14] and its higher PV device efficiency [189]. The key result for that material is that the rotational dynamics in $MA_{0.4}FA_{0.6}PbI_3$ are relatively similar to $MAPbI_3$ and $FAPbI_3$ at room temperature but that there are significant differences in the lower temperature phase ($\lesssim 150$ K). This is illustrated in Figure 6.3, which shows the determined relaxational time as a function of temperature for $MAPbI_3$, $FAPbI_3$, and $MA_{0.4}FA_{0.6}PbI_3$. In particular, a fast QENS signal was observed at 100 K, which could, based on analysis of the EISF, be assigned to the C_3 rotations of the MA cations. The mean residence time (calculated as $\tau_{C_3} = 3\hbar/\text{HWHM}$ [27]) for the C_3 rotation at 100 K was determined to be around 9 ps, which is about a factor of 50 faster than that of the corresponding dynamics in $MAPbI_3$. This indicates that there is a significant weakening of the interactions between the MA cations and the surrounding Pb-I framework in the mixed-cation systems. The faster dynamics might also be related to the absence of an orthorhombic structure of $MA_{0.4}FA_{0.6}PbI_3$ at low temperatures. These important differences in the organic cation dynamics in the low-temperature phase will be discussed in more detail in what follows.

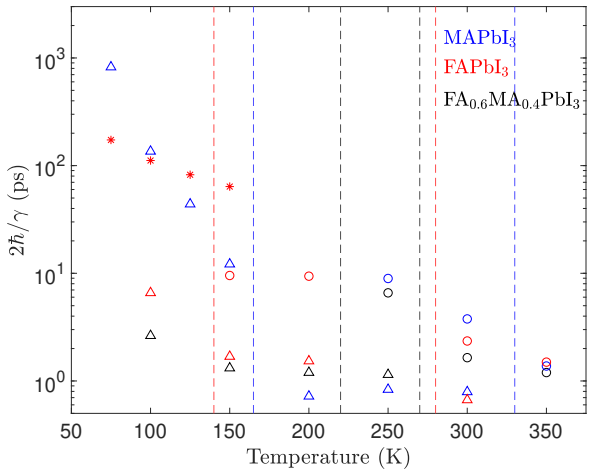

Figure 6.3: $2\hbar/\gamma$ (γ is the quasielastic FWHM), representing an apparent relaxation time of the observed dynamics, as a function of temperature for the different samples ($MAPbI_3$ blue markers, $FAPbI_3$ red markers, and $MA_{0.4}FA_{0.6}PbI_3$ black markers). The dots and triangles represent the faster and slower timescale dynamics in each sample, respectively. For $FAPbI_3$, the asterisks mark the data measured on IN16B. The dashed vertical lines mark approximately the phase transition temperatures for the different samples [69].

6.1.2 Local structure and structural stabilization in formamidinium lead iodide perovskites (Paper II)

As described in the previous chapters, the detailed crystal structure of $FAPbI_3$ is still not completely understood, in particular with respect to the low-temperature γ-phase, which is, however, believed to be locally disordered [58]. Motivated by the lack of understanding pertaining to the structure of the low-temperature phase of $FAPbI_3$ and how the doping of MA allows stabilizing the perovskite structure of $FAPbI_3$, the local structure and vibrational dynamics in $FA_{1-x}MA_xPbI_3$ (x = 0.0, 0.6, 0.9, and 1.0) were investigated by INS combined with first-principles calculations in Paper II [50]. The stable structure of $FAPbI_3$ at room temperature is a non-perovskite hexagonal phase, but a metastable cubic phase can be formed at room temperature via heating above the hexagonal-to-cubic phase transition around 400 K [58, 60, 61]. The INS spectra of $FAPbI_3$ in three different phase compositions are shown in Figure 6.4, for the cases (i) quenched to 10 K from the cubic perovskite phase (tetragonal γ-phase), (ii) in a mixture of perovskite and δ-phase, and (iii) mainly hexagonal δ-phase. The main differences in the INS spectra of the δ-phase and perovskite phase are variations in the intensities of the peaks and the disappearances of some shoulder peaks [cf. Figure 6.4]. In particular, the band between 12 meV and 15 meV grows in intensity, and the low-energy band between $7 - 20$ meV becomes broader in the

tetragonal phase, with no sharp features.

We first discuss the qualitative features of the INS spectra. Figure 6.5 shows the INS spectra of $MA_{1-x}FA_xPbI_3$ for different studied stoichiometries, as measured on TOSCA at $T = 10$ K. For $MAPbI_3$, the INS spectrum is dominated by several sharp peaks in the region below 40 meV. The vibrational dynamics of pure $MAPbI_3$ have already been studied extensively in a previous INS study [53]. The sharp modes below 30 meV mainly involve combinations of MA librations and vibrations of the lead iodide substructure [53]. The peaks above 30 meV are assigned to internal vibrations of MA. Of importance is the intense and sharp peak around ~ 37 meV, which has in a previous INS study been assigned to a torsional mode of the methyl and ammonia group of MA, and its frequency was found to be sensitive to the local structure of MA^+ [53]. Similarly, for $FAPbI_3$, the INS spectrum shows two distinct bands, one below ~ 50 meV and another between 60 - 110 meV. By comparison with the previous INS study of $MAPbI_3$ [53], the lower-frequency band most likely corresponds to combinations of molecular librations of the FA cation and phonons of the inorganic sublattice, whilst the higher-frequency band most likely correspond to internal FA modes. Above 100 meV, a few peaks are seen in the $FAPbI_3$ spectrum. These are also assigned to internal modes of the FA cation.

The spectrum of $FAPbI_3$ shows, compared to $MAPbI_3$, relatively broad peaks in the low energy region of combined molecular librations and inorganic lattice vibrations between $\sim 6-30$ meV. This indicates that the orientations of the FA cations are more disordered at 10 K, as compared to MA in $MAPbI_3$, where the cations arrange in an ordered arrangement [52]. This is in agreement with previous studies by neutron diffraction [58], thermodynamic property measurements [65], and nuclear magnetic resonance [66], which have indicated the formation of an orientational glass of $FAPbI_3$ at temperatures below ~ 100 K. For the mixed-cation materials, the peaks are less well-defined, indicating a more local disorder, as expected. One may note that both the mixed-cation materials show INS spectra that are very similar to that of $FAPbI_3$. This is consistent with the fact that both of these studied mixed-cation materials show the same low-temperature structure as $FAPbI_3$ [69]. A noticeable thing is the large damping of the torsional mode of the methyl and ammonia group of MA in the mixed-cation materials. The $MA_{0.4}FA_{0.6}PbI_3$ sample has a peak at ~ 33 meV, which most likely is the MA torsional mode. Thus, this mode has been shifted to a significantly lower frequency, and the amplitude has been reduced drastically. A similar shift and damping of this peak have been observed by Mozur *et al.* [90] for the case of $MA_{1-x}Cs_xPbBr_3$, where an orientational glass formation of MA was observed at low temperature for relatively low concentrations of Cs. Thus, this indicates that MA is present in disordered local environments in $FA_{1-x}MA_xPbI_3$ with potentially no long-range orientational ordering of either FA or MA. The downshift of the MA torsional mode in $MA_{0.4}FA_{0.6}PbI_3$ is accompanied by a shift to a higher frequency of the band at around 20 meV, which mainly involves librations of FA^+. The frequency shifts of these two modes are highlighted by the dashed lines in Figure 6.5. This

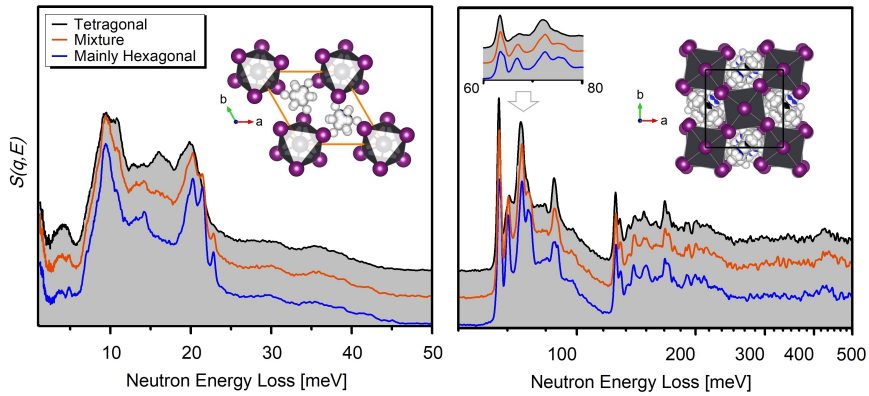

Figure 6.4: INS spectra measured at TOSCA [190] of as-synthesized $FAPbI_3$ (orange curve; a mixture of both perovskite and hexagonal phases); after storage for a period of three months (blue curve; increased phase fraction of the hexagonal phase); and (iii) after annealing at 165°C (black shaded curve; tetragonal phase). The spectra have been normalized and shifted along the vertical axis for clarity, and the spectral range of 60 – 80 meV is given as an inset. The insets show the crystal structures of the low-temperature hexagonal (left) and tetragonal γ-phase (right) phases according to Chen *et al.* [45, 61]. The figure is reproduced with permission from Paper II [50] (Copyright American Chemical Society 2021).

indicates a weakening of the interactions between MA and the surrounding perovskite framework and, at the same time, a corresponding increase in the interactions with FA. In order to understand in even more detail the effect of MA-doping, the INS data was interpreted in combination with results from DFT and *ab-initio* molecular dynamics simulations. The combination of the INS and first principles simulations allowed to further clarify some details about the stabilization of the perovskite structure of $FAPbI_3$ by doping with MA organic cations. In particular, it was found that the hydrogen-bonding interactions of the FA cations and the surrounding lead iodide framework are increased as a result of cage deformation and that this is accompanied by a weakening of the MA interactions with the lead iodide framework. One may hypothesize that these stronger interactions involving the FA cations result in a locking effect, which strongly increases the stabilization of the perovskite structure of $FAPbI_3$ upon doping with MA. This also explains the QENS results, where drastically faster MA cation dynamics in $MA_{0.4}FA_{0.6}PbI_3$ as compared to pure $MAPbI_3$ was observed in the low-temperature phase.

6.1.3 Temperature response of the vibrational dynamics in $FA_{1-x}MA_xPbI_3$ (Paper III)

In the previous section, the vibrational spectra of the $FA_{1-x}MA_xPbI_3$ materials of the ground state (10 K), as obtained using inelastic neutron scattering, were discussed

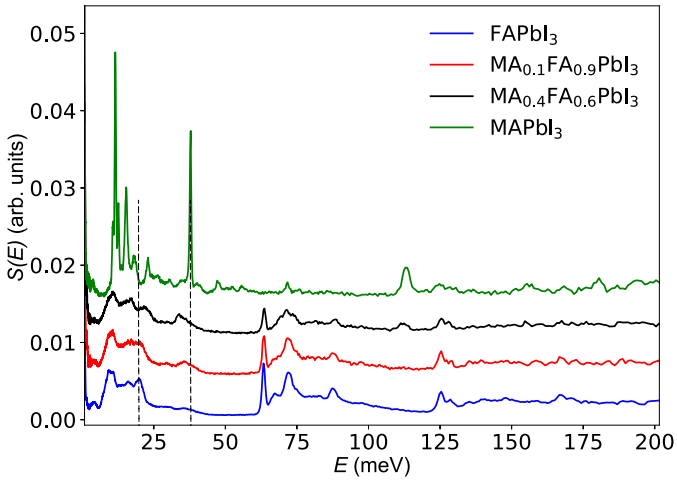

Figure 6.5: INS spectra measured at TOSCA of the series of $FA_{1-x}MA_xPbI_3$ samples measured on TOSCA at 10 K [50]. The spectra have been normalized and shifted along the vertical axis for clarity. The dashed lines indicate the peak positions of the MA torsional mode at 37 meV in $MAPbI_3$ and FA libration mode around 20 meV in $FAPbI_3$ and highlight the frequency shift of these modes for the case of $MA_{0.4}FA_{0.6}PbI_3$.

in detail. However, those results only concern the low-temperature structure of the materials, and upon heating from 10 K, these materials also undergo several phase transitions. In order to clarify how the vibrational dynamics vary as a function of temperature, variable temperature INS measurements were performed on $FA_{1-x}MA_xPbI_3$. These measurements were performed on a direct geometry spectrometer (IN5 or IN6) in order to reduce the suppression from the Debye-Waller factor, which on TOSCA is very high due to the high q values probed at higher energy transfers.

The qualitative behaviour of the dynamic response of $FAPbI_3$ as a function of temperature on the neutron energy gain side is illustrated in Figure 6.6, which shows the imaginary part of the dynamical susceptibility $\chi''(q, E)$. $\chi''(q, E)$ is related to the dynamical structure factor by

$$S(q, E) = (1/\pi)[1 + n(E)]\chi''(q, E),$$

where $n(E)$ denotes the Bose-Einstein population factor [176]. It removes the trivial temperature dependence of $S(q, E)$ coming from the population of excitations. It thus allows to study the interesting part of the temperature dependence of $S(q, E)$. At 100 K, $\chi''(q, E)$ is dominated by several broad optical phonon peaks in the energy range $4 - 25$ meV [Figure 6.6 (a)] [191]. With increasing temperature, these peaks are broadened out, and this is accompanied by an increasing quasielastic scattering, which is seen as the increasing intensity below 3 meV [Figure 6.6]. Note that, as compared

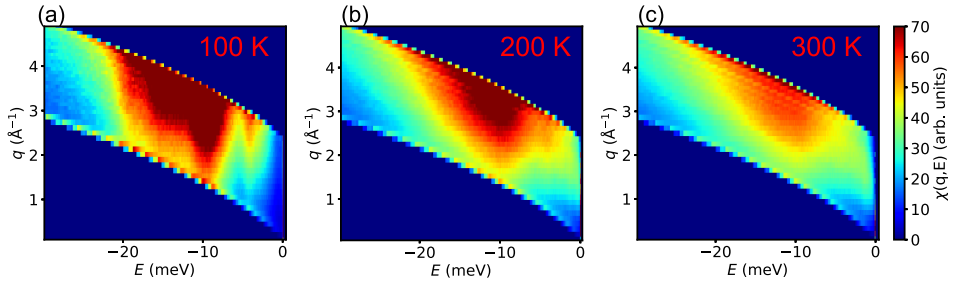

Figure 6.6: Imaginary part of the dynamic susceptibility $\chi''(q, E)$ of $FAPbI_3$ for $T = 100, 200$, and 300 K shown on the neutron energy gain side $E < 0$, measured on IN5 using an incident neutron wavelength of 5 Å. The Figure is adapted from Paper III.

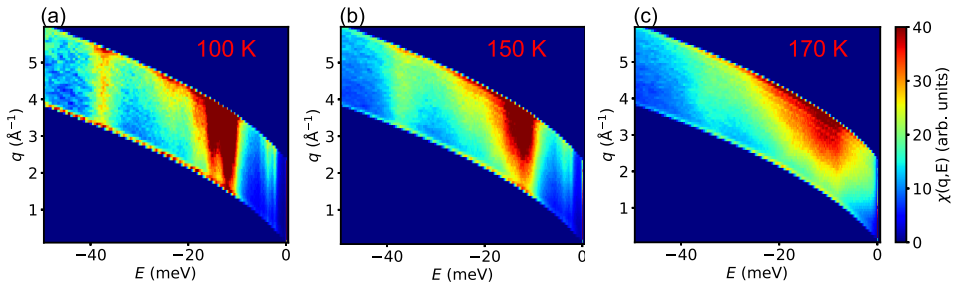

Figure 6.7: Imaginary part of the dynamic susceptibility $\chi''(q, E)$ of $MAPbI_3$ for $T = 100, 150$, and 170 K shown on the neutron energy gain side $E < 0$, measured on IN5 using an incident neutron wavelength of 5 Å. The Figure is adapted from Paper III.

to $MAPbI_3$ [Figure 6.7], which is featured by a gradual increasing broadening of the optical phonons in the orthorhombic phase, which then completely "melts" when the full rotation of the MA cations becomes activated in the tetragonal phase [28], the broadening of the inelastic response of $FAPbI_3$ is more gradual. No drastic changes in the dynamics of $FAPbI_3$ are seen when passing through the phase transition, but the $FAPbI_3$ cation dynamics are seen to gradually increase with increasing temperature. This is in accordance with the different characteristics of the phase transitions in $FAPbI_3$ and $MAPbI_3$. In $MAPbI_3$, the orthorhombic-to-tetragonal phase transition is of first-order character [114], and there is thus a discontinuous change in the vibrational properties, which is directly correlated with the activation of full molecular rotations of MA [27, 28]. For $FAPbI_3$, the data indicates a more gradual variation with temperature, indicating a different character of the phase transition.

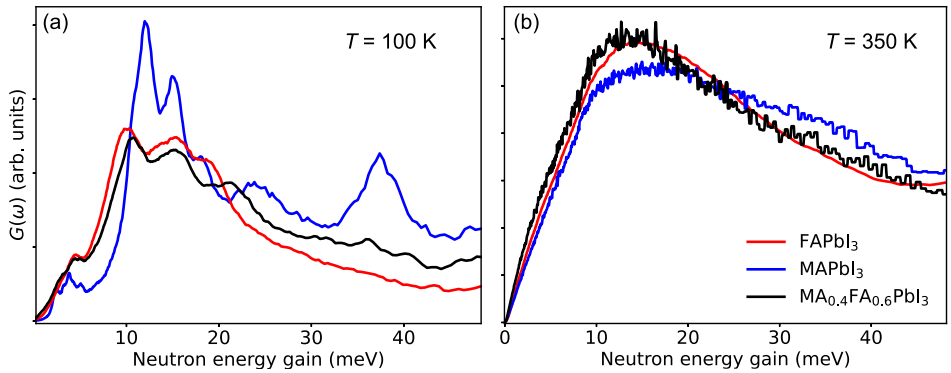

Figure 6.8: GDOS of the $FA_{1-x}MA_xPbI_3$ samples in (a) the low-temperature phase at 100 K and in (b) the cubic phase at 350 K. The measurements were performed on IN5 using an incident neutron wavelength of 5 Å. The figure is adapted from Paper III.

Figure 6.8 (a) shows the GDOS of the $FA_{1-x}MA_xPbI_3$ samples at 100 K in their low temperature phase. As can be seen, there is a slight broadening of the peaks as compared to the TOSCA data presented before, which was measured at 10 K. In particular, the MA torsional mode around 37 meV is significantly broadened for $MAPbI_3$, which most likely is due to the rotation of the methyl and ammonia groups of MA at 100 K [27]. For $MA_{0.4}FA_{0.6}PbI_3$, it is completely reduced to almost no intensity of this mode. This is consistent with the previous QENS data, showing that the methyl/ammonia rotations become significantly faster in the low-temperature phase of the mixed-cation materials. For $FAPbI_3$ and the mixed-cation materials, there is an increasing amount of low-energy modes ($\omega \lesssim 10$ meV) compared to $MAPbI_3$, which could be due to the increasing disorder, which leads to a softening of the force constant, in analogy with the difference between the vDOS in crystals versus glasses [192], which is in accordance with the expected disordered low-temperature structure of $FAPbI_3$ [58] and the mixed-cation compositions [69]. An important result is shown in Figure 6.8 (b), which shows the GDOS of the $FA_{1-x}MA_xPbI_3$ samples in their cubic phase at 350 K. As can be seen, even though there are large differences between the samples in their lower temperature phases, the GDOS of the $FA_{1-x}MA_xPbI_3$ samples displays an almost universal behaviour in their high-temperature phase. In particular, one can note a linear behaviour of the low-energy GDOS. Such a linear behaviour is typical for liquids, which shows an excess of low-energy vibrational modes, compared to the ω^2 behaviour from acoustic phonons of solids [193]. One should note that, due to the large incoherent cross section of H and the low mass of the organic cation compared to Pb and I, we essentially probe the partial vibrational density of states of the organic cation (MA or FA). At 350 K, these are rotating almost isotropically on a timescale on the order of 1 ps. Thus there will be a large number of "instantaneous configurations" of the organic cations, which could give

rise to this excess of low energy modes. One should point out that the quasielastic scattering will give rise to a function of the form $G(\omega) \sim \omega^2/(\gamma^2 + \omega^2)$, which will grow quadratic in ω until the HWHM of the Lorentzian γ and then level out and reach a constant value. However, since the HWHM of the QENS Lorentzian at 350 K is less than about 1 meV [102], the quasielastic scattering should not give a significant contribution to the GDOS in the energy range studied here.

6.1.4 Vibrational properties of $CsPbI_3$ (Paper IV)

As seen above, the hybrid perovskites $FA_{1-x}MA_xPbI_3$ exhibit highly damped vibrational dynamics in their high-temperature cubic phase. For $MAPbI_3$, this is directly correlated with the onset of MA rotations, whilst for $FAPbI_3$, the phonon broadening is more gradual. Earlier studies have, in fact, claimed that HOIPs belong to the class of materials known as "phonon glass electron crystals", meaning that they show 'band-like' charge carrier dynamics and "glass-like" phonons [34, 35, 194]. However, later studies based on Raman scattering [30] and inelastic neutron scattering [29] have also found that there is overdamped phonon dynamics also in the all-inorganic $CsPbBr_3$, meaning that the rotational dynamics is not critical for the forming the highly damped phonons. In order to fully understand the lattice dynamics in lead iodide perovskites and how it varies with temperature, INS studies were also performed on the all-inorganic perovskite $CsPbI_3$.

We focused on the differences between the non-perovskite δ-phase and the cubic perovskite phase, which is formed around 600 K. Figure 6.9 shows the measured dynamical structure factor of δ-$CsPbI_3$ measured at 10 K. The data is compared to the simulated $S(q, \omega)$ based on harmonic phonon calculations. As can be seen, there is a good agreement between the simulated and experimental data. This shows that the lattice dynamics of δ-$CsPbI_3$ can be described in terms of a harmonic picture. Figure 6.10 compares the dynamical structure factor at 550 K in the δ-phase and in the cubic perovskite phase at around 600 K. As can be seen, there is a significant increase in low-energy scattering upon passing through the phase transition, and there is no clear gap between the elastic and inelastic scattering in the cubic phase. For a more detailed analysis of the low-energy scattering in the cubic perovskite phase of $CsPbI_3$, a fitting analysis was performed on $S(q, \omega)$. Figure 6.11 (a) shows the $S(q, \omega)$ of $CsPbI_3$ and $CsPbBr_3$ for the q values corresponding roughly to modulus of the wavevector transfer at $\mathbf{M} = (\frac{3}{2}, \frac{1}{2}, 0)$ r.l.u. For these certain q-values, quasielastic scattering was observed, as shown in Figure 6.11. For $CsPbI_3$ at $q = 1.55$ Å^{-1}, there is a narrow quasielastic scattering peak, which could be modelled using a Lorentzian function with an HWHM of about 0.16 meV. This corresponds to relaxational dynamics with a relaxational time of $\hbar$/HWHM $\simeq$ 4 ps. Comparing our results to the recent INS study on the similar material $CsPbBr_3$ [29], the observed quasielastic scattering is most likely related to overdamped transverse acoustic phonon branch at the M-point. This phonon mode is related to the tilting of the PbI_6 octahedra, and these tilting motions at the M-point give rise to the tetragonal distortions. They are thus associated with the

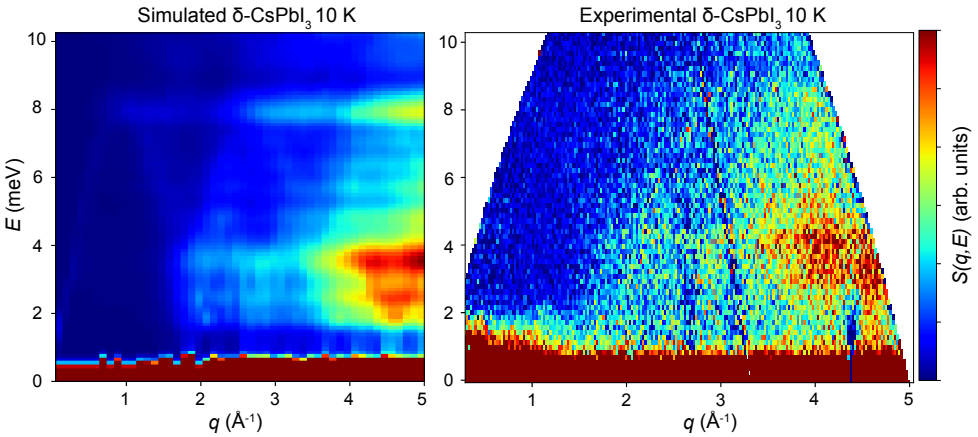

Figure 6.9: (Left panel) Simulated $S(q, E)$ from harmonic phonons of δ-$CsPbI_3$. The phonon calculations were obtained from the Phonon database at Kyoto University [177], and $S(q, E)$ (both coherent and incoherent parts) was simulated from the phonon eigenvectors and eigenfrequencies using Oclimax [178]. (Right panel) Experimental $S(q, E)$ at $T = 10$ K of δ-$CsPbI_3$ measured on ARCS at the SNS using an incident neutron energy of 15 meV. The figure is adapted from Paper IV.

cubic-to-tetragonal phase transition. Quasielastic scattering at the M-point is thus expected near the cubic-to-tetragonal phase transition, which occurs around 550 K [49], based on the soft-phonon model for displacive phase transitions [109]. However, we here observe quasielastic scattering in $CsPbI_3$ at 600 K, which is about 50 K above the expected cubic-to-tetragonal phase transition. These results are in agreement with a recent MD simulation study on $CsPbBr_3$, which shows that these phonon modes become overdamped even relatively far from the phase transition temperatures [111]. For a powder sample of $CsPbBr_3$, we observed a quasielastic scattering with an HWHM of about 0.4 meV is observed at $q = 1.69$ Å^{-1} [Figure 6.11 (b)], corresponding approximately to the modulus of the $\mathbf{M} = (\frac{3}{2}, \frac{1}{2}, 0)$ r.l.u. for cubic $CsPbBr_3$. This is similar to what has been observed at the R-point of $CsPbBr_3$ in another single-crystal INS study [195], and the recent MD simulations [111]. Quasielastic scattering was also observed for some other q values. For $CsPbI_3$ at q =1.65 Å^{-1}, roughly corresponding to the modulus of $\mathbf{R} = (\frac{3}{2}, \frac{1}{2}, \frac{1}{2})$ r.l.u, the relaxational dynamics were found to be slightly faster. It could be fitted using a Lorentzian with an HWHM of about 0.275 meV, corresponding to a relaxational time of 2.4 ps. At the R-point, the overdamped transverse acoustic phonon branch corresponds to the octahedral tilt patterns associated with the tetragonal-to-orthorhombic phase transition [29, 111]. This phase transition is expected to occur around 450 K for $CsPbI_3$ [49]. In the soft phonon model, τ is expected to decrease as the temperature is increased in the cubic phase [111], which is in agreement with that we observe faster relaxational dynamics at the R-point in $CsPbI_3$. Overall, these results show that the octahedral tilting modes are highly overdamped in the cubic phase of $CsPbI_3$, which means that

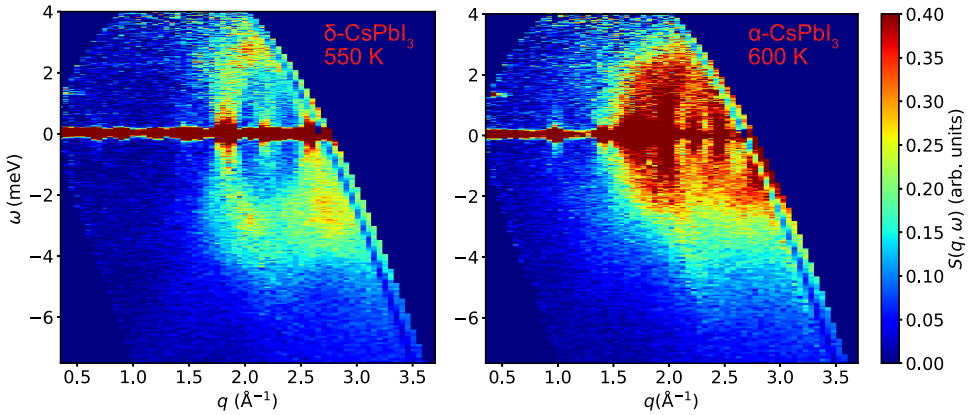

Figure 6.10: Dynamical structure factor $S(q, E)$ of δ-$CsPbI_3$ and $\alpha-CsPbI_3$ measured using FOCUS at the PSI, using an incident neutron wavelength of 4 Å. The figure is adapted from Paper IV.

the structure dynamically fluctuates between tetragonal and orthorhombic distorted phases on the timescale of $\sim 2-5$ ps. This means that the cubic perovskite phase is highly dynamic, and the ideal cubic structure only can provide a qualitative view of the structure of the material.

For the hybrid organic-inorganic perovskites, an additional source of anharmonicity is the rotational dynamics of the organic cations as have been observed using, for example, optical [196, 197] and neutron [27, 82, 83, 101] spectroscopies. The GDOS of $MAPbI_3$, $FAPbI_3$, and $CsPbI_3$ in their high-temperature cubic phases are compared in Figure 6.12 (c). For a direct comparison, the GDOS have been normalized to the same number of vibrational modes in the energy range $0-30$ meV and plotted on a scaled energy axis $\omega/\omega_{\max}$, where $\omega_{\max}$ is the energy for which the GDOS shows a maximum. As can be seen in Figure 6.12 (c), one may note that the GDOS shown here, for both the hybrid and all-inorganic lead iodide perovskites, in many features, resembles the vDOS of a liquid. The vibrational dynamics of liquids are commonly described in terms of a set of instantaneous normal modes (INMs), which is defined by diagonalizing the dynamical matrix for each instantaneous atomic configuration [198]. This gives rise to both harmonic normal modes and modes of imaginary "frequencies", where the imaginary frequencies lead to an exponential decay of the atomic displacements, thus describing relaxational dynamics. The presence of highly anharmonic and overdamped dynamics in MHPs suggests that the INMs picture might be a more accurate representation of their vibrational dynamics compared to a purely harmonic one. Recently, a simple closed-form analytic expression for the vDOS of a liquid has been derived [193], and shortly afterwards was experimentally confirmed [199]. To test how "liquid-like" the vDOS of lead iodide perovskites really is and the claims about "crystal-liquid duality" in MHPs [28, 34, 35, 194, 200], the

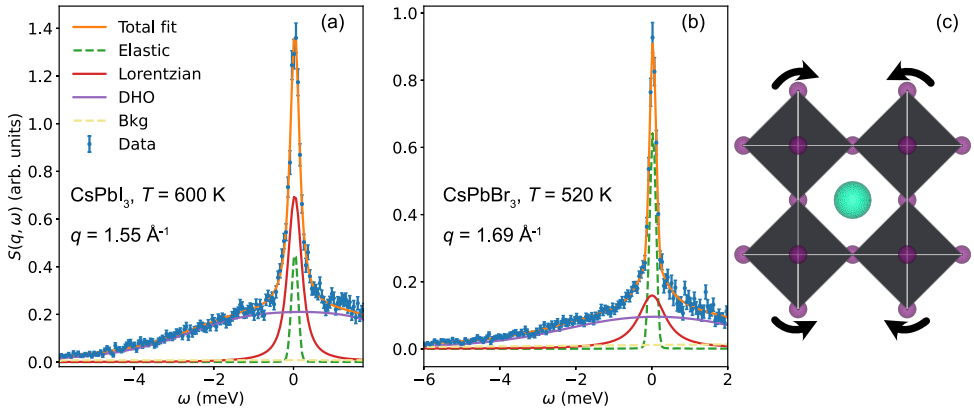

Figure 6.11: (a) Fitting of $S(q,\omega)$ for $CsPbI_3$ in the α-phase at 600 K at $q = 1.55$ Å^{-1} and for $CsPbBr_3$ at 520 K and 1.69 Å^{-1}; these q-values roughly correspond to absolute values of q vectors at the M-point of the cubic Brillouin zone. The data were measured using FOCUS at the PSI, using an incident neutron wavelength of 4 Å. (c) Illustration of the octahedral tilting mode at the M-point. The figure is adapted from Paper IV.

GDOS were fitted to the following expression which describes the vDOS of a general liquid [193, 199]

$$g(\omega) \propto \frac{\omega}{\omega^2 + \gamma_{\text{eff}}^2} e^{-(\omega/\omega_D)^2}, \tag{6.2}$$

where γ_{eff} is an effective relaxation rate of the INMs, and ω_D is a high-frequency Debye cutoff. Figure 6.12 shows the GDOS of $CsPbI_3$, $MAPbI_3$, and $FAPbI_3$ in their high-temperature cubic phases fitted to the liquid vDOS model of Eq. (6.2) using both γ_{eff} and ω_D as fitting parameters. As can be seen, the low-energy GDOS of $CsPbI_3$ cannot be well described by the liquid model, which predicts a linear behaviour at low energies. The low-energy GDOS data of $CsPbI_3$, however, is more similar to the ω^2 Debye-law for crystals, thus indicating that acoustic phonons are still "crystal-like" in the high-temperature perovskite phase. This is consistent with the observed correlations in the momentum transfer dependence of $S(q,\omega)$ and the increased phonon scattering around Bragg peaks. For the hybrid materials, however, the GDOS follows very well a low-energy linear behaviour and can be relatively well described by the liquid model over this energy range. As for the hybrid organic-inorganic materials, the dominant contribution to the GDOS comes from the H atoms in the organic cations. Thus, this indicates that the vibrational dynamics of organic cations in HOIPs are relatively similar to that of a liquid in the high-temperature phases. The difference between the all-inorganic $CsPbI_3$ and the HOIPs can be due to the ps-timescale molecular rotational dynamics. The organic cation dynamics are further coupled to the lead iodide substructure through hydrogen bonding, and its dynamics might thus give rise to many different instantaneous dynamic atomic

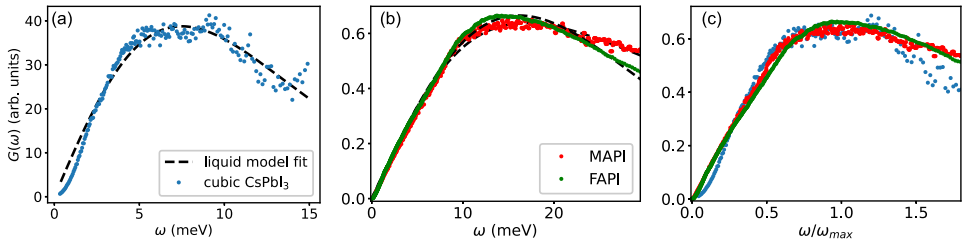

Figure 6.12: GDOS of (a) $CsPbI_3$ and (b) $MAPbI_3$ and $FAPbI_3$ in their high-temperature cubic phases. The data for $CsPbI_3$ is obtained at 600 K, and the data for $MAPbI_3$ and $FAPbI_3$ is taken at 350 K. The GDOS is fitted to the liquid vDOS model of Eq. (6.2) (black dashed lines). (c) Comparison of the GDOS of cubic $CsPbI_3$, $MAPbI_3$, and $FAPbI_3$ plotted on a scaled energy axis $\omega/\omega_{\max}$, where $\omega_{\max}$ is the energy in which the GDOS shows a maximum.

configurations. Some of these configurations are not stable, which will lead to an increase in imaginary modes, which can produce the linear low-energy behaviour of the vDOS [193]. One should, however, point out that well-defined acoustic phonons have been observed experimentally in the cubic phase of the hybrid MHPs near the Brillouin zone center [115, 201, 202]. In the INS experiments, one mainly observes the partial vibrational density of states of the organic cations, which do not have much involvement in the acoustic phonon displacements. As a result, it is likely that the acoustic phonons, which mainly involve displacements of Pb and I, remain well-defined, despite the fact that the vibrations of the organic cations resemble that of a liquid.

6.1.5 Organic cation dynamics in layered hybrid lead iodide perovskites (Paper V)

In order to gain a more complete picture of organic cation dynamics in MHPs, the studies were further expanded to include so-called layered materials, often called "two-dimensional (2D) halide perovskites" [18]. These materials are based on the Ruddlesden-Popper crystal structure with general chemical formula R_2BX_4, where R is an organic cation, B is a metal cation (*e.g.* Pb, Ge, Sn), and X is a halide anion. In this structure, the organic cations need to be relatively large, which also means that there is more versatility in the choice of the organic spacer. In my studies, I focused in particular on two prototypical layered lead iodide perovskites, namely phenethylammonium ($C_6H_5(CH_2)_2NH_3$, PEA) and butylammonium ($CH_3(CH_2)_3NH_3$, BA) lead iodide. BA_2PbI_4 and PEA_2PbI4 are two of the most well-studied and understood in terms of crystal structure and phase transitions [24, 25]. They also represent two different cases of organic cation, which thus provides a way to investigate the effect of the type of organic cation on the dynamics and optical performance of the materials. PEA has a phenyl ring, whilst BA is a linear alkyl chain with an end

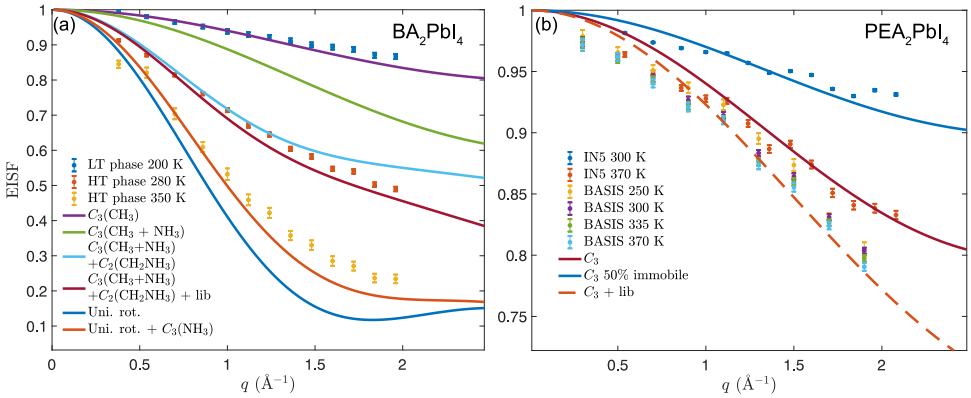

Figure 6.13: EISF of BA_2PbI_4 (left panel) and PEA_2PbI_4 (right panel), together with different jump-diffusion models describing localized dynamics of BA and PEA. The Figure is adapted from Paper V.

ammonia group. Importantly, these two materials also have some differences in their optical and electronic properties, where PEA systems have longer slower electron-hole recombination and longer carrier lifetimes[136, 203, 204], and more than one order of magnitude faster exciton diffusion and longer exciton diffusion lengths [205]. These two materials are thus good model systems for understanding the organic cation dynamics and how it relate to the properties of the materials.

BA_2PbI_4 is featured by a first-order phase transition with a large hysteresis, around 240 K on cooling and 270 K on heating [119, 122], which were found to be significantly coupled with the observed structural dynamics using QENS. In particular, different dynamics were observed in the two different phases of BA_2PbI_4, and the same hysteresis effect was observed in the organic cation dynamics, as is observed using crystallographic techniques [122]. In the low-temperature phase, only the methyl and ammonia group rotations could be observed above $\sim$ 100 K. In the high-temperature phase above 300 K, the BA cations were found to undergo nearly uniaxial rotations around the long molecular axis (Figure 6.13), with almost no preferred orientations of the organic cations around this axis on a timescale longer than a few ps. Importantly, this means that the phase transition in BA_2PbI_4 can be characterized as an order-disorder transition of the BA cations, which is in agreement with x-ray diffraction [122] and recent Raman scattering results [119]. For the case of PEA_2PbI_4, the organic cation dynamics were found to be significantly more restricted in nature. In particular, the only observed dynamics were found to be the C_3 rotations of the ammonia group (Figure 6.13), while the rest of the hydrogen atoms in PEA remain static on the probed timescales ($\tau \gtrsim 400$ ps) for temperatures ≤ 370 K. Going back to the differences in optoelectronic properties in BA_2PbI_4 and PEA_2PbI_4, one may speculate around potential correlations between the observed differences in structural dynamics and in optoelectronic properties. In particular, the less restricted

cation dynamics observed in the high-temperature phase of BA_2PbI_4 may act as an additional scattering source for excitons, potentially decreasing their lifetime and diffusion lengths, in line with what has been observed in comparison to PEA_2PbI_4 [205]. On the other hand, for the case of 3D hybrid perovskites, the organic cation rotations have been hypothesized to induce polar fluctuations, which can potentially create separations of electrons and holes and thus lead to increased charge carrier lifetimes [45, 97]. For the case of $MAPbI_3$, the rotations of MA reorient the dipole moment of the MA cations [27], which arguably could induce these polar fluctuations in the materials. The dynamics observed in BA are mainly concerned with the rotations around the molecular axis, which does not change the molecular dipole moment and could then be argued to have less influence on polar fluctuations. However, it should still give rise to increased scattering of excitons and other charge carriers, and the increased dynamics in BA_2PbI_4 might thus explain the lower exciton lifetimes and diffusion lengths observed in BA_2PbI_4 as compared to PEA_2PbI_4.

6.1.6 Vibrational dynamics in layered hybrid lead iodide (Paper VI)

Both lattice dynamics and rotational dynamics of organic cations are believed to be of importance for the charge carrier recombination rates and exciton properties in metal halide perovskites [10]. In order to get a more complete understanding of what causes the differences in the optoelectronic properties of BA_2PbI_4 and PEA_2PbI_4, their vibrational dynamics were further investigated using INS in Paper VI.

At 10 K, it was found that the INS spectra of both BA_2PbI_4 and PEA_2PbI_4 are featured by a large number of sharp and intense peaks in the spectral regions from about $5 - 60$ meV, which is followed by slightly weaker features that extends all the way to about 400 meV. The modes above 50 meV are most likely internal vibrations of the organic cations. Strong peaks in the spectral range below this are assigned to molecular librations, which are expected to exhibit a high intensity in INS. One may note that the sharp spectral features below 50 meV indicate a well-ordered low-temperature structure of both BA_2PbI_4 and PEA_2PbI_4. This is similar to what has been observed for $MAPbI_3$ [53] and $MAPbBr_3$ [206], but different from $FAPbI_3$ [50] and $FAPbBr_3$ [104], where the low-temperature structure is more disordered [58].

For BA_2PbI_4, we observed a strong dependence for the two different phases of the INS spectra, which is illustrated in Figure 6.14. In the high-temperature phase, there is a continuum of quasielastic scattering and no sharp features in the dynamic response as a function of energy transfer. Upon passing the phase transition to the low-temperature phase, around 230 K, however, there is a drastic change in the spectra, and sharp well-defined peaks appear. Upon cooling, one can notice a pronounced stiffening (shift to higher frequencies) of the sharp mode around 12 meV (at 50 K) and a significant narrowing of the lower energy bands below 100 K. The observed broadening above 100 K might be related to the activation of the CH_3 and

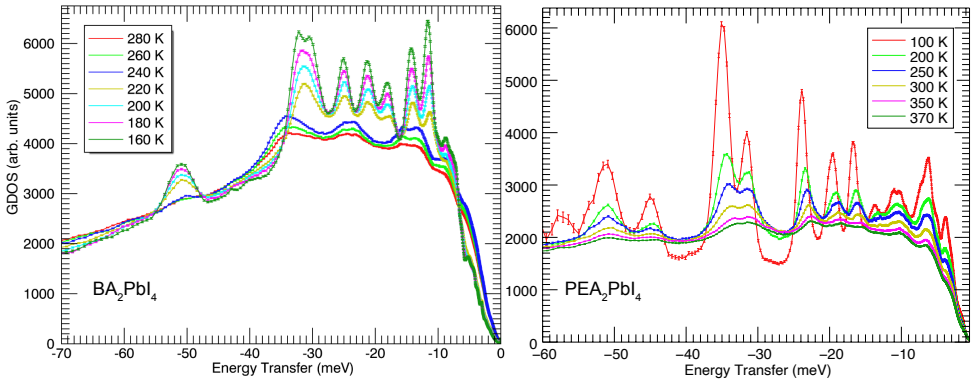

Figure 6.14: GDOS of BA_2PbI_4 (left panel) and PEA_2PbI_4 (right panel) as a function of temperature. For BA_2PbI_4, the phase transition occurs between 220 and 240 K. The data were obtained on IN5 using an incident neutron wavelength of 5 Å. The Figure is adapted from Paper VI.

NH_3 group rotations, which rotate on a timescale on the order of 0.1 ns at around 100 K. In the low-temperature phase, the GDOS of BA_2PbI_4 is featured by several sharp peaks, which can be assigned to molecular librations, that broaden continuously upon increasing the temperature and becomes extremely broad in the high-temperature phase ($T \geq 240$ K). Accompanied by this, there is a large increase in low-energy scattering, which can be seen as the increase in modes below ~ 10 meV. In the high-temperature phase, one may note that several of the BA librational vibrations ($E \sim 12 - 50$ meV) shift to slightly higher frequencies. In the high-temperature phase, the long molecular axis of the organic cations is more aligned to the crystallographic *c*-axis, and the time-averaged octahedral tilt angle is significantly smaller, although not zero [119]. This could potentially cause larger intermolecular interactions between the BA cations, which could potentially increase the vibrational frequencies of the librational modes.

The temperature response of the INS spectra for PEA_2PbI_4 is shown in Figure 6.14. For PEA_2PbI_4, there are no known phase transitions in the measured temperature range ($10 - 370$ K), and, in accordance with this, a more gradual phonon broadening upon increasing the temperature is observed for PEA_2PbI_4. The sharp mode around ~ 35 meV is assigned to an NH_3 torsional mode, in similarity with $MAPbI_3$ [53]. This mode shows a particularly strong temperature dependence, which is in accordance with the activation of the NH_3 rotations in PEA_2PbI_4 around $\sim 150 - 200$ K.

6.2 Oxyhydride perovskites

This section summarizes and discusses the results on perovskite-type oxyhydrides, which are reported in Papers VII – IX.

6.2.1 Hydride-ion diffusion in $SrVO_2H$ (Paper VII)

The results on hydride-ion diffusion in $SrVO_2H$ are reported in Paper VII [155]. In order to try to understand better the fundamental mechanism of hydride ion diffusion in oxyhydrides, QENS measurements were performed on the oxyhydride $SrVO_2H$. Interestingly, this material is different from the more well-studied systems $ATiO_{3-x}H_x$ (A = Ba, Sr, Ca) [39, 42, 152] in that the hydride ions are fully ordered in the anion substructure, giving rise to a layered tetragonal structure [36], which might affect the diffusional dynamics of hydride ions. Figure 6.15 shows some QENS results from $SrVO_2H$ as measured on the backscattering spectrometer HFBS, probing timescales in the range $\sim$ 50 ps $-$ 2 ns. The q-dependence of the scattering signal indicated translational diffusional dynamics, which could be well modelled using a Chudley-Elliot model [182] describing jump diffusion in the ab-plane of the crystal structure, which is shown in Figure 6.15 (b). It was found that this translational diffusion occurs on the ns timescales and with a diffusion coefficient of about 1×10^{-6} cm^2/s at 430 K. In order to obtain a complete picture of the hydride ion diffusional dynamics in $SrVO_2H$, complementary QENS measurements were also performed on the OSIRIS instrument, which probes faster timescale dynamics, in the range of $\sim 2 - 65$ ps. Interestingly, a faster QENS signal was then also observed. The q-dependence of this QENS signal was in accordance with a localized diffusion process and could be modelled as a dumb-bell motion with a jump distance fixed to the H$-$H distance in the ab-plane, *i.e.* a hydride ion jumping forth and back between two hydride sites. In $SrVO_2H$, the hydride anion substructure is believed to be fully occupied [36], and one may thus expect that there are few vacancies available for diffusion. Hence, after a hydride jumps to a vacant site, the probability of a backwards jump will be significantly increased because the probability of a vacancy at the original site is significantly enhanced [207]. This would mean that there is an increased probability for a backwards jump, and the hydride-ion could be temporally localized around a specific vacancy. Taken altogether, this diffusion mechanism could thus be described as a temporally correlated vacancy-assisted jump diffusion, with an increased rate for backward jumps. It may be noted that such a correlated diffusion mechanism is usually not considered in QENS experiments on ionic conductors in general. The analysis methods applied in Paper VII might thus be of more general use for interpreting QENS data of solid ionic conductors where the concentration of mobile species is high or, equivalently, the vacancy concentration is low. Such a correlated diffusion mechanism is expected to decrease the hydride-ion conductivity because mobile hydride-ions become temporally localized, neighbouring to a particular hydride-ion vacancy. Accordingly, tuning the anion vacancy concentration in $SrVO_2H$ may be a promising way to improve the ionic conductivity.

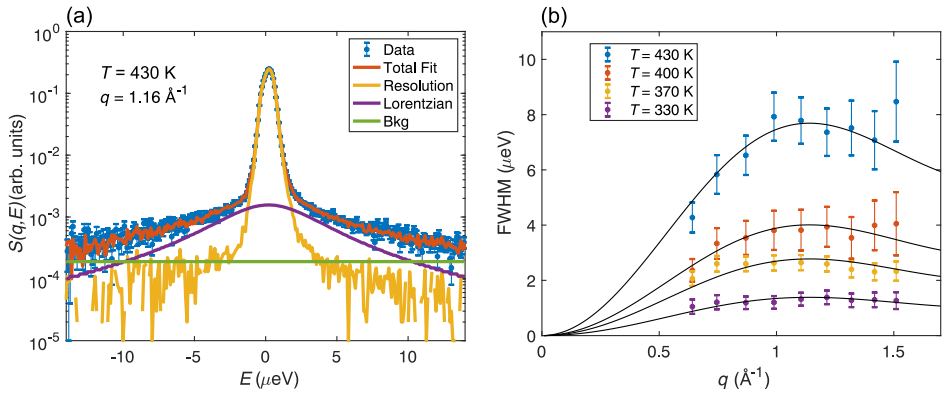

Figure 6.15: (a) QENS spectra of $SrVO_2H$ as measured using neutron backscattering at HFBS for $T = 430$ K, and $q = 1.16$ Å^{-1}. (b) Quasielastic linewidth (FWHM) as a function of q and temperature. The solid lines are fits to a Chudley-Elliot jump-diffusion model with a fixed jump distance of 3.94 Å. Reprinted with permission from Paper VII [155].

In order to confirm if such a correlated jump-diffusion mechanism could give rise to the observed experimental data and for a more quantitative understanding of possible correlated jump diffusion in $SrVO_2H$, the QENS data were evaluated in terms of a simple phenomenological model, which could explain the observed phenomena. To this end, the so-called backward jump model [208], originally developed by Haus and Kehr in 1979, was used. This model introduces *ad hoc* an enhanced probability for a backward (return) jump. In this model, the self-correlation function $G_s(\mathbf{r}, t)$ is separated into components which depend on the previously visited site:

$$G_s(\mathbf{r}, t) = \sum_{i=1}^{z} P(\mathbf{r}, \mathbf{r}_i, t), \tag{6.3}$$

where $P(\mathbf{r}, \mathbf{r}_i, t)$ is the probability that the particle is at site $\mathbf{r}$ at time t after previously being at site $\mathbf{r}_i$ one step before and at $\mathbf{r}_0$ at $t = 0$. Considering only nearest neighbour jumps, z is the number of nearest neighbour sites. The general equation to calculate $P(\mathbf{r}, \mathbf{r}_i, t)$ is then given by [208]

$$\begin{aligned} \frac{\partial}{\partial t} P(\mathbf{r}, \mathbf{r}_i, t) = &- \left(\frac{1}{\tau_1} + (z-1)\frac{1}{\tau_2} \right) P(\mathbf{r}, \mathbf{r}_i, t) + \frac{1}{\tau_1} P(\mathbf{r}_i, \mathbf{r}, t) \\ &+ \frac{1}{\tau_2} \sum_{m=1}^{z} P(\mathbf{r}_i, \mathbf{r}_m, t), \end{aligned} \tag{6.4}$$

where $1/\tau_1$ is the return jump rate, and $1/\tau_2$ is the jump rate to a new site. In the backwards model, $\tau_1 < \tau_2$ so that the jump rate of a backward jump is higher than the jump rate of a forward or sideways jump to a new site. By performing a Fourier

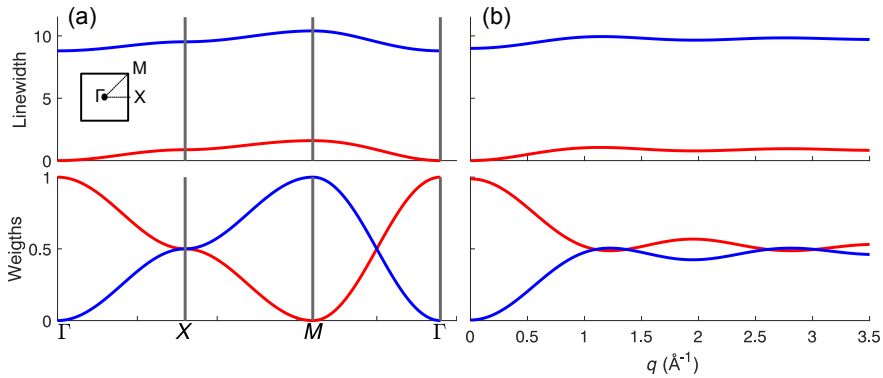

Figure 6.16: (a) Dispersion of the eigenvalues and weights of a simple backward jump model along the high-symmetry directions of the 2D square lattice as indicated in the inset. The values were calculated with $1/\tau_1 = 4$ and $\tau_2 = 8\,\tau_1$. (b) 3D powder average of the corresponding dispersions in (a). Reprinted with permission from Paper VII [155].

transform in space and Laplace transform in time, this equation can be written as a matrix equation [208]

$$(u - \mathbf{D}(\mathbf{q}))\mathbf{P}(\mathbf{q}, u) = 1, \tag{6.5}$$

where u is the Laplace time and $\mathbf{D}(\mathbf{q})$ is the so-called dynamical matrix and $\mathbf{P}(\mathbf{q}, u)$ is the vector with $P(\mathbf{q}, \mathbf{r}_i, u), i = 1, 2, \ldots, z$ as components. The problem is thus reduced to a matrix eigenvalue problem. The self-correlation function in Laplace and Fourier space is given by $P(q, u) = \sum_i (\mathbf{P}(\mathbf{q}, u))_i$ and can be solved as [208]

$$P(\mathbf{q}, u) = \sum_{n=1}^{z} \frac{W_n(\mathbf{q})}{u - u_n(\mathbf{q})/2}, \tag{6.6}$$

where $u_n(\mathbf{q})/2$ are the eigenvalues of $\mathbf{D}(\mathbf{q})$, and the weights $W_n(\mathbf{q})$ are given by $W_n(\mathbf{q}) = \sum_{l,m} T_{ln}(T^{-1})_{nm}$, where T is the matrix constructed by the eigenvectors of $\mathbf{D}(\mathbf{q})$ as columns. The dynamical structure factor $S(\mathbf{q}, E)$ is related to $P(\mathbf{q}, u)$ by the following relation

$$S(\mathbf{q}, E) = \frac{1}{\pi}\mathrm{Re}\left[P(\mathbf{q}, u = \mathrm{i}E)\right] = \frac{1}{\pi}\sum_{n=1}^{z} \frac{u_n(\mathbf{q})}{2} \frac{W_n(\mathbf{q})}{E^2 + (u_n(\mathbf{q})/2)^2}. \tag{6.7}$$

$S(\mathbf{q}, E)$ is thus a sum of Lorentzian functions with FWHMs $u_n(\mathbf{q})$ and relative intensities $W_n(\mathbf{q})$.

In order to directly compare the backwards model to the QENS data of $SrVO_2H$, the eigenvalues and eigenvectors of the backward jump model for diffusion on the 2D square lattice were calculated numerically. There are two non-vanishing modes, one

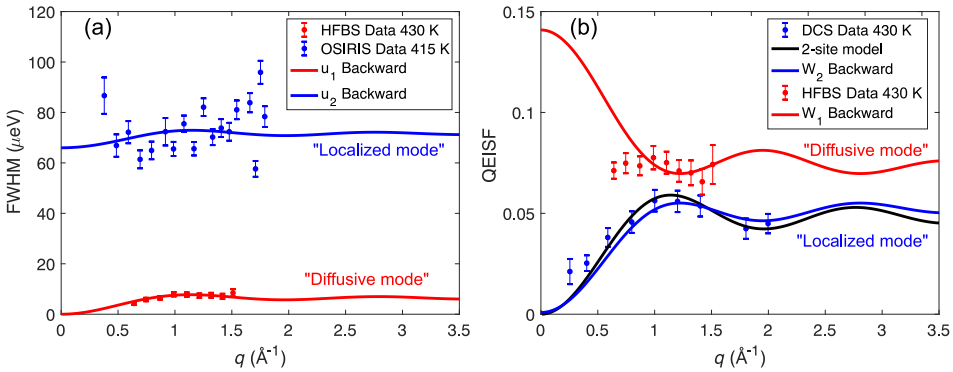

Figure 6.17: (a) QENS linewidth $SrVO_2H$ as measured at HFBS (diffusive mode) and OSIRIS (localized mode), together with fits to the powder averaged backwards jump-diffusion model. (b) Corresponding quasielastic incoherent structure factors (QEISF = 1− EISF). The QEISF are multiplied by a factor $(1-p)$ where p represents the immobile fraction of H atoms on the timescale of the instrument. Reprinted with permission from Paper VII [155].

low-energy diffusive mode and one higher-energy localized mode that emerges due to the increased probability of a backward jump, which is shown in Figure 6.16, and thus supports the interpretation of the two observed QENS signals in the experiments. The predicted FWHM and structure factors (QEISF) (relative intensities of the Lorentzians) of the powder averaged backwards jump model are shown in Figure 6.17, together with the data measured for the diffusive and localized modes (measured on HFBS and OSIRIS, respectively). As can be seen, the experimental data are in good agreement with this model using that $\tau_1 = \tau_2/10$, which supports that the localized diffusion can be interpreted from an increased rate for backward jumps, and in addition, shows that the residence time for backwards jumps is a factor of 10 shorter than for jumps to other sites.

6.2.2 Hydride-ion diffusion in barium titanate oxyhydride (Paper IX)

The hydride-ion diffusion in barium titanate oxyhydride was studied using QENS in Paper IX. We focused on a sample with a relatively large oxygen vacancy concentration and with the chemical composition of $BaTiO_{2.55}H_{0.12}\square_{0.33}$, as determined by a combination of NMR and thermogravimetric analysis, according to the procedure in Ref. [209]. A quasielastic signal was observed for temperatures $\geq$ 250 K, which could be modelled using a single Lorentzian component for all measured temperatures. Analyzing the q-dependence of the QENS signal indicated that the dynamics could be described in terms of a long-range (translational) diffusion process, in agreement with the recent QENS study by Eklöf-Österberg *et al.* [44]. From the fitted parameters of

the q-dependence of the QENS FWHM, the (Einstein) diffusion coefficient could be calculated and was found to be between 0.4×10^{-5} cm^2/s at 250 K, to 1.5×10^{-5} cm^2/s at 550 K. This is about one order of magnitude larger than the corresponding values for $SrVO_2H$, which might be related to a large number of oxygen vacancies in the material. These values are, however, similar to what was reported for $LaSrCoO_3H_{0.7}$ using QENS [43]. One may also note that this value is significantly larger than what has been measured using more macroscopic techniques such as SIMS depth-profiling, which was performed on $SrTiO_{3-x}H_x$ thin films [166]. In such experiments, one probes a diffusion coefficient which will depend on the hydride transport through the whole material, on significantly longer length scales than probed using QENS. In QENS, one should obtain the pure bulk diffusion coefficient, however, one should also note that one only measure relatively short length-scales. The largest length scale probed in QENS can be approximately estimated from the smallest measured q values by $2\pi/q_{\min} \approx 17$ Å, which corresponds to about 4 unit cells. Thus, it's possible that the probed dynamics become more localized at longer length scales than this. Another important thing to point about is that in the QENS experiments, most of the scattering is observed to be purely elastic (resolution limited), and only a few percent of the total scattering signal is quasielastic. This means that most of the hydride ions in the material are static (move too slowly to be observed) on the probed timescale. Thus, in QENS, one probes the diffusion of these few percent of mobile hydrogens, which most likely is related to specific local environments.

6.2.3 Vibrational dynamics and spin-phonon coupling in $SrVO_2H$ (Paper VIII)

In order to gain more insight into the vanadium-hydrogen bonding situation in $SrVO_2H$ and to understand how this is related to the hydride-ion diffusion mechanism, the vibrational dynamics of $SrVO_2H$ were studied by INS and infrared spectroscopy in combination with phonon calculations based on density functional theory. These results are reported in Paper VIII [210]. Figure 6.18 shows the INS spectrum, measured on MAPS at 10 K. The hydride ion vibrational modes were determined to be a degenerate bending mode (motion perpendicular to the H−V−H chain direction) and a stretching mode (along the H−V−H chain direction), with a large phonon dispersion along the z-direction. These modes are schematically illustrated in the inset of Figure 6.18. The H−V bending mode observed around 800 cm^{-1} was found to be clearly split into two components separated by about 50 cm^{-1}. Figure 6.19 compares the IR spectrum (measured at RT) and INS spectrum of $SrVO_2H$. The peaks are marked with their corresponding assigned irreducible representations (at the Γ-point). In IR, only the higher frequency component of the H−V bending mode is observed because the E_g component is IR inactive. Similar is observed for the H−V stretching mode, where the lower frequency component is observed in IR.

Interestingly, by analysing the INS data in combination with DFT phonon calculations, it was found that this splitting occurs due to the doubling of the unit cell from

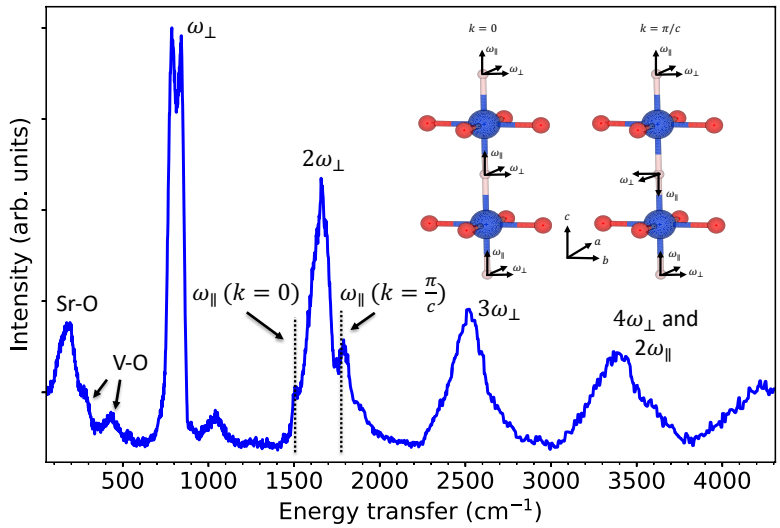

Figure 6.18: INS spectra of $SrVO_2H$, measured at 10 K using the MAPS instrument at ISIS Neutron and Muon Source [210]. The inset shows a schematic sketch of the H−V vibrational modes. Note that there are also contributions from the Al sample cell in the low-energy region at around ≈ 150 and ≈ 290 cm^{-1}. The figure is adapted with permission from Paper VIII [210].

the antiferromagnetic structure. In addition, analysis of the results from the DFT calculated phonon dispersion, in combination with the INS data, reveals unusually large spin-phonon coupling in $SrVO_2H$ This was determined by comparing DFT phonon calculations of the AFM structure with a non-magnetic reference structure and could be seen as blue shifts of the hydride ion vibrational modes by 50−100 cm^{-1}, even though super-exchange coupling via H is relatively small. Similar frequency shifts of the same order of magnitude were also found for the V−O in-plane modes, whereas V−O out-of-plane and lower energy modes involving the Sr ions were found to be essentially unaffected by the magnetic ordering. These results provide direct evidence for the novel and interesting many-body effects that can occur in strontium vanadium oxyhydride phases, where interesting couplings between the magnetism and hydrogen dynamics can occur.

Spin-phonon coupling is a well-known phenomenon and has been examined earlier for various systems [211–216]. Spin-phonon coupling occurs from the magnetic exchange interactions contributing to the harmonic energy of lattice [217]. Assuming a simple Heisenberg Hamiltonian,

$$\mathscr{H} = -\sum_{i \neq j} J_{ij} \mathbf{S}_i \cdot \mathbf{S}_j,$$

the change in force constant is given by [213]

$$\tilde{K}_{\alpha\beta} = K_0 - \sum_{i \neq j} \frac{\partial^2 J_{ij}}{\partial u_\alpha \partial u_\beta} u_\alpha u_\beta \left\langle \mathbf{S}_i \cdot \mathbf{S}_j \right\rangle , \tag{6.8}$$

where K_0 is the force constant without considering the magnetic energy, J_{ij} is the exchange couplings between atom i and j, u_α is the displacement vectors, and $\mathbf{S}_i$ is the spin vector of atom i. Thus, if the second derivative of the exchange couplings with respect to the displacement vectors are non-vanishing, the magnetic ordering will cause a change in the "force constants" and thus also a shift of the phonon frequency, according to

$$\omega = \sqrt{K_{\alpha\beta}/M} = \sqrt{\frac{K_0 - \sum_{i \neq j} \frac{\partial^2 J_{ij}}{\partial u_\alpha \partial u_\beta} u_\alpha u_\beta \left\langle \mathbf{S}_i \cdot \mathbf{S}_j \right\rangle}{M}}, \tag{6.9}$$

where M is some effective mass. Assuming that the frequency shift is small compared to the bare frequency (without any spin-phonon interaction), Eq. (6.9) can be expanded as[1]

$$\omega \approx \omega_0 + \lambda \left\langle \mathbf{S}_i \cdot \mathbf{S}_j \right\rangle , \tag{6.10}$$

where λ describes the strength of the spin-phonon interaction, and $\omega_0 = \sqrt{K_0/M}$ is the bare phonon frequency. From the definition in Eq. (6.10), the coupling constant can be calculated according to

$$\lambda = \frac{1}{2\sqrt{K_0}} \sum_{i \neq j} \frac{\partial^2 J_{ij}}{\partial u_\alpha \partial u_\beta} u_\alpha u_\beta . \tag{6.11}$$

As seen in Eq. (6.10), the frequency shift is proportional to the spin-spin correlation function. Assuming a perfectly ordered antiferromagnetic structure (as in $SrVO_2H$, $S = 1$), one finds that $\langle \mathbf{S}_i \cdot \mathbf{S}_j \rangle = -S^2$. Above the Néel temperature, the spin-spin correlation function $\langle \mathbf{S}_i \cdot \mathbf{S}_j \rangle$ goes to zero, thus meaning that the phonon frequency shift from spin-phonon coupling goes to zero in the paramagnetic phase.
In most cases, the frequency shift from spin-phonon coupling is relatively small, often on the order of $1 - 15$ cm^{-1} [218–225], with the, to the best of knowledge, highest one reported being ≈ 40 cm^{-1} for $NaOsO_3$ [226]. For $SrVO_2H$, it was found that the frequency shifts are much larger, on the order of $50 - 100$ cm^{-1} for both H−V and V−O in-plane modes. However, it is important to point out that the spin-phonon coupling in $SrVO_2H$ was only determined from the DFT calculations by comparing the phonon frequencies for AFM $SrVO_2H$ to that of a non-magnetic reference structure. This comparison is limited because the non-magnetic reference structure is slightly distorted. In addition, the non-magnetic DFT calculation does not consider paramagnetism, which should be present in $SrVO_2H$ even above the Néel temperature. The Néel temperature of $SrVO_2H$ is around 600 K and is accompanied by the partial decomposition of the material. Thus, it was not possible to measure the

[1] Using the expansion $\sqrt{1+x} \approx 1 + \frac{x}{2}$ for $x \ll 1$.

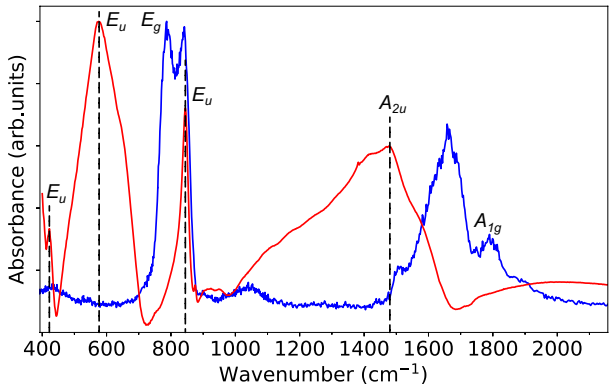

Figure 6.19: INS spectra of $SrVO_2H$, measured at 10 K (blue line) and infrared spectrum measured at RT (red line) [210]. The fundamental peaks are marked with their corresponding irreducible representations. The figure is adapted with permission from Paper VIII [210].

INS spectra through the magnetic phase transition. Future studies on, for example, the related strontium vanadium oxyhydrides Sr_2VO_3H, and $Sr_3V_2O_5H_2$ with lower Néel temperatures (below room temperature) [36], or other magnetic oxyhydrides, would be interesting for further research.

6.2.4 Neutron scattering studies on other transition metal oxyhydrides

6.2.4.1 Quasielastic neutron scattering on $La_xSr_{4-x}NiRuO_4H_4$

In collaboration with the group of Prof. M. Hayward at Oxford University, QENS measurements were also performed on the novel oxyhydride materials $La_xSr_{4-x}NiRuO_4H_4$ with $x = 0.6, 1.0$, and 1.4. In these materials, which are based on the Ruddlesden-Popper structure, the hydride anions occupy the equatorial anion sites, leading to a layered structure of alternating (La/Sr)O and (Ni/Ru)H_2 planes [158, 227]. Figure 6.20 shows the QENS spectra of $LaSr_3NiRuO_4H_4$ as measured on OSIRIS [228] at the ISIS Neutron and Muon Source, which, with the used experimental set-up[2], probes dynamics on the timescales between $\sim 1 - 80$ ps. As can be seen, no quasielastic signal could be observed for the $La_xSr_{4-x}NiRuO_4H_4$ system with $x = 0.6, 1.0,$, and 1.4 which means that no hydride ion diffusion was observed on the probed timescale for temperatures $\leq$ 600 K. This indicates that the hydride ion diffusion in these materials is slower than about 80 ps ($\tau \gtrsim 80$ ps). It is hypothesized that this is due to the lack of vacancies in these materials, as, based on neutron powder diffraction, the anion sites are thought to be fully occupied [158].

[2]We used the PG(002) analyzers which provide an energy resolution of about 25 μeV and an accessible energy transfer range of $\pm$ 0.4 meV.

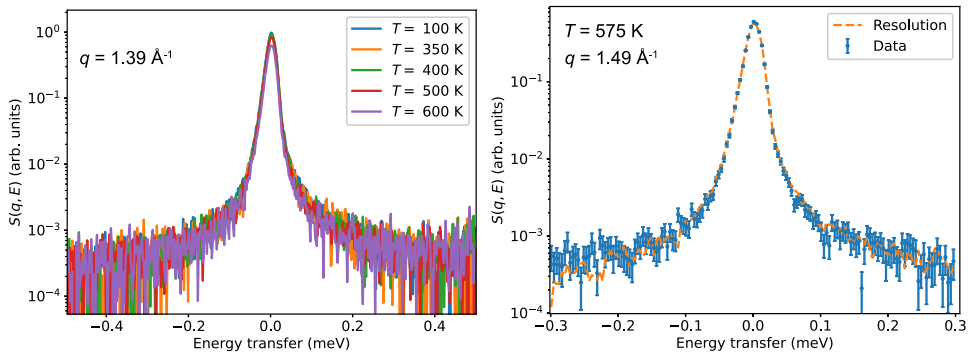

Figure 6.20: (a) QENS spectra for of $LaSr_3NiRuO_4H_4$ for different temperatures at $q = 1.39$ Å^{-1}, as measured on OSIRIS at the ISIS Neutron and Muon Source. (b) Fit to the QENS spectra for $T = 575$ K and $q = 1.49$ Å^{-1}. As can be seen, the spectrum can be fitted to a single delta function convoluted with the instrumental resolution function, meaning that no QENS signal could be observed on the measured timescales of OSIRIS. Further experimental details can be found at [229].

6.2.4.2 Vibrational dynamics in $La_2Sr_2CoRhO_6H_2$ and $LaSr_3MnRhO_6H_2$

In the same collaboration with the group of Prof. M. Hayward at Oxford University, the local structure and vibrational dynamics of hydride ions were investigated in the two related oxyhydrides $La_2Sr_2CoRhO_6H_2$ and $LaSr_3MnRhO_6H_2$, using INS. These two materials are isostructural to the $La_xSr_{4-x}NiRuO_4H_4$, however, there is an anion disorder on the 'equatorial' anion site, which is roughly 50% occupied by H^- and 50% occupied by O^{2-} [159]. Qualitatively, based on studies on similar materials [44, 210, 230], one expect three modes of vibration for the hydride ions, one in each direction of the lattice. Because of the low mass of the hydride ions, these modes will be separated to higher frequencies (energies) than the rest of the vibrational modes. Since the crystal structures of the materials are tetragonal ($I4/mmm$) [159], one further expects three distinct hydride ion vibrational frequencies at the Γ-point, where the motion parallel to the hydrogen transition metal bond should have the highest frequency due to the bond stretching nature of this mode. However, one should note that there is a large chemical disorder in the materials (Rh/Co or Rh/Mn disorder on the transition metal site, La/Sr disorder on the A-site, and H/O disorder in the anion substructure), so one may still expect a wider distribution of frequencies because of the disorder.

Figure 6.21 shows the INS spectra of the $La_2Sr_2CoRhO_6H_2$ and $LaSr_3MnRhO_6H_2$ samples measured at 10 K, using the FANS instrument at the NIST Center For Neutron Research (NCNR), NIST, USA. As can be seen, the peaks in both samples are relatively broad, which is most likely due to the large chemical disorder in the

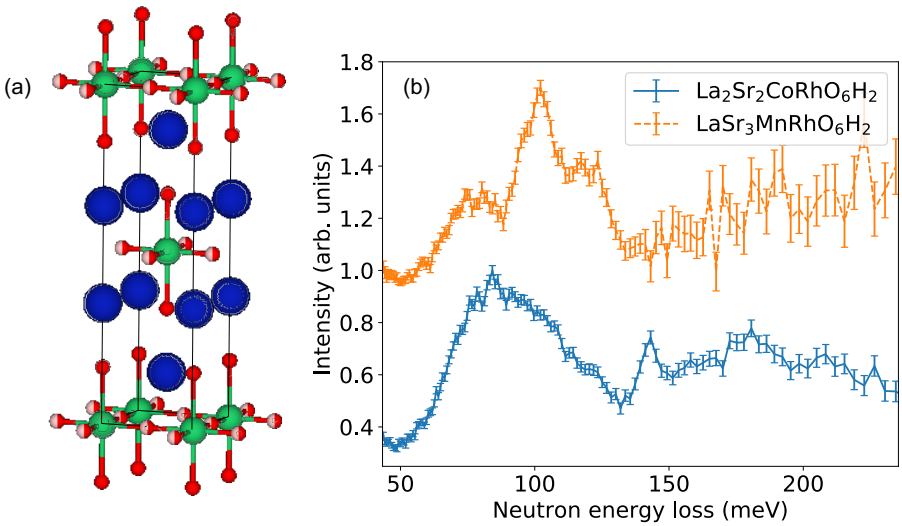

Figure 6.21: (a) Illustration of the Ruddlesden-Popper crystal structure ($I4/mmm$) of $La_2Sr_2CoRhO_6H_2$ and $LaSr_3MnRhO_6H_2$. La/Sr atoms are illustrated as blue spheres, oxygen atoms are illustrated as red spheres, and the transition metals Rh/Co/Mn atoms as green spheres. The hydride ions are incorporated on the 'equatorial' site with an anion disorder ($\sim$ 50% H^- and 50% O^{2-}) illustrated as the half-filled red/pink spheres [159]. (b)INS spectra of $La_2Sr_2CoRhO_6H_2$ and $LaSr_3MnRhO_6H_2$ measured on FANS at NCNR, NIST at 10 K. The spectra are shown offset along the vertical axis for clarity.

systems. In the $La_2Sr_2CoRhO_6H_2$, there is a sharp peak just below 150 meV, which might be related to the Co/Rh−H stretching mode. Below this, there is a broad band, which ranges from about 60 meV to 130 meV. This band likely corresponds to H vibrations in the *ab* plane, which might be very broad due to the chemical and structural disorder. In the bending mode, the hydride moves towards the La/Sr ions, so this mode might be more sensitive to the chemical disorder in the system. For $LaSr_3MnRhO_6H_2$, three relatively broad peaks are observed around 80 meV, 110 meV, and 130 meV, which might be related to hydride vibrations along the three principal axes of the lattice. One may note that the presumed stretching mode, around 130 meV, is significantly lower in energy than in $La_2Sr_2CoRhO_6H_2$, and might reflect the slightly longer transition metal hydrogen bond length in $LaSr_3MnRhO_6H_2$ [159]. A quantitative analysis of the vibrational spectra, however, would require phonon calculations in order to assign and interpret in detail all features of the INS spectra. Such calculations might still be challenging because of the chemical disorder in the system and the possible influence of short-range magnetic order, but they would be interesting for future continuation studies.

Chapter 7

Conclusions and outlook

As summarized in the previous Chapter, this thesis has provided new fundamental understanding of the local structure and dynamics in MHPs and perovskite oxyhydrides. For $FAPbI_3$, the rotational organic cation dynamics were probed and characterized in detail in all three crystal phases using QENS. It was found that the FA cation rotations are nearly isotropic, with almost no preferred orientations in the cubic perovskite phase. In the intermediate temperature tetragonal phase, the FA cation was found to undergo rotational dynamics between preferred orientations, with the main dynamics being rotations around the N$\cdots$N and C$-$H axes. In the low-temperature γ-phase, an even more complex cation dynamics were found, which is due to the formation of an orientational glass of FA [58]. Importantly, it was further found that doping of MA^+ leads to significantly different organic cation dynamics, which was found to be related to the stabilization of the perovskite crystal structure in the mixed-cation systems $FA_{1-x}MA_xPbI_3$. The vibrational dynamics in $FA_{1-x}MA_xPbI_3$ were further studied using variable-temperature INS. A key result is that these materials exhibit completely overdamped vibrational dynamics in their room-temperature cubic perovskite phase. For $MAPbI_3$, it was found that the overdamping of vibrational modes is directly correlated with the onset of rotations of MA at the orthorhombic-to-tetragonal phase transition around 165 K, whilst for $FAPbI_3$, the phonon broadening is more gradual. Crucially, it was further found that such overdamped vibrational dynamics are not limited to the hybrid MHPs, but also are present in the cubic phase of $CsPbI_3$. In $CsPbI_3$, the overdamped dynamics are related to relaxational octahedral tilting dynamics, which are present at specific q points. Lastly, the studies of organic cation dynamics were extended to include the layered lead iodide perovskites PEA_2PbI_4 and BA_2PbI_4. It was found that these two prototypical layered MHPs are featured by significantly different organic cation dynamics, whereas the PEA dynamics are much more restricted in nature.

For the perovskite oxyhydrides, the hydride ion diffusion mechanism was studied in detail in $SrVO_2H$ and $BaTiO_{3-x}H_y$. In $SrVO_2H$, the hydride ion diffusion was found to be restricted to the hydride-ion substructure. The diffusion mechanism could

be described in terms of a correlated jump diffusion mechanism with an increased rate for backward jumps. Such a correlated diffusion is due to the low number of hydride-ion vacancies, which give rise to an increased backward jump rate. It thus temporally localizes a hydride ion to a specific vacancy, which is expected to decrease the long-range diffusion. For $BaTiO_{3-x}H_y$, a faster diffusion (about one magnitude larger diffusion coefficient) was observed, and no correlated diffusion mechanism could be distinguished from the experimental data. This was most likely due to a large number of oxygen vacancies in the studied barium titanate oxyhydride sample, which provides a pathway for faster hydride diffusion. In both cases, however, the results highlighted the importance of the concentration and distribution of anion vacancies in the materials, and a promising way to improve the hydride-ion conductivity in oxyhydrides would be to tune the concentration of hydride ion and concentration and distribution of anion vacancies. The vibrational dynamics were also studied in $SrVO_2H$ using INS. An important result of this study was that the vibrational dynamics were found to be largely influenced by the antiferromagnetic ordering of the material. Thus, this highlights important couplings between the magnetism and hydride ion vibrational dynamics in magnetic oxyhydrides, an area which is virtually unexplored so far.

There are many possibilities to extend the studies presented in this thesis. For the MHPs, an important result was that MA doping of $FAPbI_3$ leads to different organic cation dynamics, which was found to be of importance for the stabilization of the perovskite crystal structure. Interestingly, other dopants, *e.g.*, Cs^+ have also been shown to be able to stabilize the perovskite structure and, in addition, change the phase behaviour of $FAPbI_3$ [15] and disrupt concerted FA cation dynamics in $FAPbBr_3$ [104]. With a view towards the future, I plan to also investigate the effect of Cs-doping on the local structure and dynamics of FA cations in $FA_{1-x}Cs_xPbI_3$, using QENS and INS, in a similar way as the studies presented here for $FA_{1-x}MA_xPbI_3$. Initial QENS experiments have already been performed, and more measurements are planned. The study on lattice dynamics would be interesting to expand to similar materials, such as $CsSnI_3$ [231] and would provide additional insights into the relationship between cation and overdamped fluctuations in MHPs. Another interesting question concerns if similar overdamped dynamics of the octahedral tilting modes, as observed in $CsPbI_3$ and $CsPbBr_3$, are also present in the hybrid perovskites, such as $MAPbI_3$ and $FAPbI_3$. Previous studies have, to the best of my knowledge, been unable to answer this question because, in neutron scattering, the signal is dominated by the organic cations [191], and optical probes (Raman and IR) measure only the phonons at the Γ-point of the Brillouin zone [30]. Inelastic X-ray scattering studies have been performed on $MAPbI_3$, however, the energy resolution is worse than for neutron scattering, making it particularly hard to probe soft phonon modes [56, 232]. A possible way forward could be to use INS with polarization analysis. Then one could separate the incoherent and coherent contributions on the scattering signal and thus remove the large incoherent contribution from the organic cations and focus on the coherent part, which should mainly contain contributions from the Pb-I

substructure. For the layered (2D) MHPs, this thesis only investigated two different materials, and there is a plethora of other materials left to explore. For example, a recent QENS study has shown a correlation between broadband luminescence and organic cation dynamics [135], thus making this an exciting topic for further studies on organic cation dynamics in layered MHPs.

In the case of perovskite-type oxyhydrides, there is much left to understand regarding the hydride ion diffusion mechanism. There are many interesting compounds left to explore, and there are also interesting studies left to do on the more well-studied systems. For example, in the case of barium titanate oxyhydrides, the studies in this thesis only focused on samples with a relatively large number of oxygen vacancies. An interesting follow-up study would be a more systematic approach where one tries to determine the hydride diffusion in a series of samples which differs in their oxygen vacancy and hydride ion concentrations. One difficulty with this is that it's hard to prepare such a series of samples with a systematic variation in oxygen vacancies and hydride ion concentrations; in many cases, the resulting hydride and anion vacancy concentrations appear almost random and thus seem hard to control [209]. However, a recent study by Guo *et al.* [233] showed that a series of samples differing mainly in oxygen vacancy concentration, with almost the same concentration of hydride ions, could be synthesized using reduction with LiH at different temperatures. Thus, this may provide a way forward towards understanding, in a more systematic way, the influence of anion vacancy distribution on the hydride ion diffusion mechanism. For $SrVO_2H$, tuning the number of vacancies and/or hydride ion concentrations might seem even more difficult. However, it has been shown that the hydride-ion concentrations can be tuned in a similar strontium vanadium oxyhydride $Sr_2VO_{4-x}H_x$ [234] using a high-pressure synthesis method. Thus, it's clear that new synthesis methods and novel compounds are also needed in order to advance the understanding of hydride ion dynamics in transition metal oxyhydrides.

An interesting result in this thesis was that the vibrational dynamics in $SrVO_2H$ were largely influenced by the magnetic ordering through the spin-phonon coupling. This is an area which is, to the best of my knowledge, not studied at all for magnetic oxyhydrides. Experimental studies on spin-phonon coupling, using INS and/or IR/Raman spectroscopy, in magnetically ordered oxyhydrides would thus be a very interesting continuation study. Interesting compounds to explore include, for example, $SrCrO_2H$ [153], $LaSrCoO_3H_{0.7}$ [145], and the strontium vanadium oxyhydrides Sr_2VO_3H and $Sr_3V_2O_5H_2$ [36].

Chapter A

Perovskite solar cell principle

This appendix describes, in short, the working principle of a solar cell device based on MHPs.

In a standard photovoltaic (PV) device (solar cell), the operating principle is based on a so-called p-n junction. A p-n junction is the interface boundary between a n-type and a p-type semiconductor. When the p-type and n-type semiconductors come in contact, the Fermi levels of the two materials align, causing band bending near the interface. This further creates a space charge layer, which gives rise to a built-in electric field which can separate light-excited charge carriers in this region [235]. The simplest PV device is thus simply a p-n junction. For example, most silicon solar cells are based on this principle and consist of p-doped and n-doped Si crystals allowing the creation of the PV device.

Metal halide perovskites are intrinsic semiconductors, so the Fermi level lies in between the valence and conduction bands. There are several ways to make a PV device from MHPs. The initial works were made with sensitized solar cells on TiO_2 films [4]. However, in the later years, most work has shifted towards thin film devices, where the MHP is present as a thin film. In a thin film perovskite solar cell device, the MHP acts as the light-absorbing active layer and is typically sandwiched between a p-type and an n-type semiconductor [236], which is illustrated in Figure A.1 (a). It thus functions as a p-i-n (or n-i-p) junction, where the MHP works as the intrinsic (i) semiconductor material. On top and below this construction, there are also electrodes, allowing to conduct the resulting current. Typically, on top of the device, there is a transparent conductive oxide (for example, indium tin oxide or fluorine-doped tin oxide), which also allows the light to pass through. A schematic sketch of the corresponding energy diagram of such a simple device is shown in Figure A.1 (b). The Fermi level aligns to be the same in the materials, creating the band bending near the interfaces and a built-in electric field. Upon light excitation, the photon excites an electron from the valence band to the conduction band, creating an electron-hole

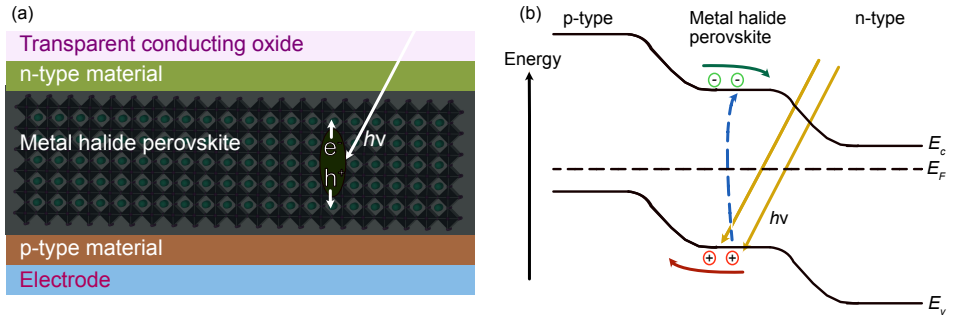

Figure A.1: (a) Schematic sketch of a thin film perovskite PV device. The MHP is sandwiched between an n-type and a p-type material, allowing separation of the light-induced charge carriers. (b) Schematic sketch of the energy diagram of the device in (a). E_F, E_c, and E_v denote the Fermi level, conduction band energy, and valence band energy, respectively. The blue line indicates the excitation of electrons from the valence to the conduction band by light. Note that the relative distances and energies in the figure are just drawn as a sketch and might not be fully realistic.

pair in the MHP. Since the charge carrier diffusion lengths in MHPs are relatively large [7], and the film is relatively thin, the excited charge carriers can diffuse until they reach the built-in electric field, where they will be accelerated by the electric field, inducing an electric current.

Acknowledgements

First of all, I like to thank my main supervisor Maths Karlsson, for all his support and good advice on research over the years and for giving me the opportunity to do my PhD at Chalmers. I would also like to thank my examiner Lars-Gunnar Johansson, my director of studies, Itai Panas, and my assistant supervisor Max Wolff, for all their support and good advice. I would further like to thank Ulrich Häussermann and Lorenzo Malavasi for their great scientific advice and for providing samples. Thank you to Michael Koza, Adrien Perrichon, Mikael Andersson, and Franz Demmel for their help with the experiments and discussion about neutron data analysis. I also like to acknowledge my other collaborators, Kacper Druzbicki, Erik Fransson, Paul Erhart, Markus Appel, Jeff Armstrong, Michael Sannemo, Olga Vekilova, Paulo Carvalho, Masato Matsuura, Garrett Granroth, Fanni Juranyi, Niina Jalarvo, and Stewart Parker.

A big thanks to my past and present colleagues and office friends Aymen, Carin, Elena, Kanming, Laura, Lucas, Mikael, Peng, Reddy, Yuan-Chih, and all other friends and colleagues at the OOMK division.

Lastly, I also like to express my greatest appreciation to my family for all the support. Especially to Petra and Melker for keeping up with me during the time I wrote this thesis.

Bibliography

[1] Jeon, N. J.; Noh, J. H.; Yang, W. S.; Kim, Y. C.; Ryu, S.; Seo, J.; Seok, S. I. Compositional engineering of perovskite materials for high-performance solar cells. *Nature* **2015**, *517*, 476–480.

[2] Weber, D. $CH_3NH_3PbX_3$, ein Pb (II)-system mit kubischer perowskitstruktur/$CH_3NH_3PbX_3$, a Pb (II)-system with cubic perovskite structure. *Z. Naturforsch. B* **1978**, *33*, 1443–1445.

[3] Poglitsch, A.; Weber, D. Dynamic disorder in methylammoniumtrihalogenoplumbates (II) observed by millimeter-wave spectroscopy. *J. Chem. Phys.* **1987**, *87*, 6373–6378.

[4] Kojima, A.; Teshima, K.; Shiral, Y.; Tsutomu, M. Organometal Halide Perovskites as Visible- Light Sensitizers for Photovoltaic Cells. *J. Am. Chem. Soc.* **2009**, *131*, 6050–6051.

[5] Lee, M. M.; Teuscher, J.; Miyasaka, T.; Murakami, T. N.; Snaith, H. J. Efficient Hybrid Solar Cells Based on Meso-Superstructured Organometal Halide Perovskites. *Science* **2012**, *338*, 643–647.

[6] Li, Z.; Klein, T. R.; Kim, D. H.; Yang, M.; Berry, J. J.; van Hest, M. F. A. M.; Zhu, K. Scalable fabrication of perovskite solar cells. *Nat. Rev. Mater.* **2018**, *3*, 18017.

[7] Stranks, S. D.; Stranks, S. D.; Eperon, G. E.; Grancini, G.; Menelaou, C.; Alcocer, M. J. P.; Leijtens, T.; Herz, L. M.; Petrozza, A.; Snaith, H. J. Electron-Hole Diffusion Lengths Exceeding 1 Micrometer in an Organometal Trihalide Perovskite Absorber. *Science (80-.).* **2013**, *342*, 341–344.

[8] National Renewable Energy Laboratory, Best Research-Cell Efficiency Chart. https://www.nrel.gov/pv/cell-efficiency.html, Accessed: 2023-02-21.

[9] Berry, J. et al. Hybrid Organic–Inorganic Perovskites (HOIPs): Opportunities and Challenges. *Adv. Mater.* **2015**, *27*, 5102–5112.

[10] Gallop, N. P.; Selig, O.; Giubertoni, G.; Bakker, H. J.; Rezus, Y. L.; Frost, J. M.; Jansen, T. L.; Lovrincic, R.; Bakulin, A. A. Rotational cation dynamics in metal halide perovskites: Effect on phonons and material properties. *J. Phys. Chem. Lett.* **2018**, *9*, 5987–5997.

[11] Egger, D. A.; Bera, A.; Cahen, D.; Hodes, G.; Kirchartz, T.; Kronik, L.; Lovrincic, R.; Rappe, A. M.; Reichman, D. R.; Yaffe, O. What Remains Unexplained about the Properties of Halide Perovskites? *Adv. Mater.* **2018**, *30*, 1800691.

[12] Kim, J. Y.; Lee, J.-W.; Jung, H. S.; Shin, H.; Park, N.-G. High-Efficiency Perovskite Solar Cells. *Chem. Rev.* **2020**, *120*, 7867–7918.

[13] Weber, O. J.; Charles, B.; Weller, M. T. Phase behaviour and composition in the formamidinium–methylammonium hybrid lead iodide perovskite solid solution. *J. Mater. Chem. A* **2016**, *4*, 15375–15382.

[14] Pisanu, A.; Ferrara, C.; Quadrelli, P.; Guizzetti, G.; Patrini, M.; Milanese, C.; Tealdi, C.; Malavasi, L. The $FA_{1-x}MA_xPbI_3$ System: Correlations among Stoichiometry Control, Crystal Structure, Optical Properties, and Phase Stability. *J. Phys. Chem. C* **2017**, *121*, 8746–8751.

[15] Charles, B.; Weller, M. T.; Rieger, S.; Hatcher, L. E.; Henry, P. F.; Feldmann, J.; Wolverson, D.; Wilson, C. C. Phase behavior and substitution limit of mixed cesium-formamidinium lead triiodide perovskites. *Chem. Mater.* **2020**, *32*, 2282–2291.

[16] Noh, J. H.; Im, S. H.; Heo, J. H.; Mandal, T. N.; Seok, S. I. Chemical management for colorful, efficient, and stable inorganic-organic hybrid nanostructured solar cells. *Nano Lett.* **2013**, *13*, 1764–1769.

[17] Eperon, G. E.; Stranks, S. D.; Menelaou, C.; Johnston, M. B.; Herz, L. M.; Snaith, H. J. Formamidinium lead trihalide: A broadly tunable perovskite for efficient planar heterojunction solar cells. *Energy Environ. Sci.* **2014**, *7*, 982–988.

[18] Grancini, G.; Nazeeruddin, M. K. Dimensional tailoring of hybrid perovskites for photovoltaics. *Nat. Rev. Mater.* **2019**, *4*, 4–22.

[19] Dohner, E. R.; Hoke, E. T.; Karunadasa, H. I. Self-assembly of broadband white-light emitters. *J. Am. Chem. Soc.* **2014**, *136*, 1718–1721.

[20] Dohner, E. R.; Jaffe, A.; Bradshaw, L. R.; Karunadasa, H. I. Intrinsic white-light emission from layered hybrid perovskites. *J. Am. Chem. Soc.* **2014**, *136*, 13154–13157.

[21] Yangui, A.; Garrot, D.; Lauret, J.-S.; Lusson, A.; Bouchez, G.; Deleporte, E.; Pillet, S.; Bendeif, E.-E.; Castro, M.; Triki, S., et al. Optical investigation of broadband white-light emission in self-assembled organic–inorganic perovskite $(C_6H_{11}NH_3)_2PbBr_4$. *J. Phys. Chem. C* **2015**, *119*, 23638–23647.

[22] Smith, M. D.; Jaffe, A.; Dohner, E. R.; Lindenberg, A. M.; Karunadasa, H. I. Structural origins of broadband emission from layered Pb-Br hybrid perovskites. *Chem. Sci.* **2017**, *8*, 4497–4504.

[23] Smith, M. D.; Karunadasa, H. I. White-light emission from layered halide perovskites. *Acc. Chem. Res.* **2018**, *51*, 619–627.

[24] Cho, K. T.; Grancini, G.; Lee, Y.; Oveisi, E.; Ryu, J.; Almora, O.; Tschumi, M.; Schouwink, P. A.; Seo, G.; Heo, S.; Park, J.; Jang, J.; Paek, S.; Garcia-Belmonte, G.; Nazeeruddin, M. K. Selective growth of layered perovskites for stable and efficient photovoltaics. *Energy Environ. Sci.* **2018**, *11*, 952–959.

[25] Koh, T. M.; Shanmugam, V.; Guo, X.; Lim, S. S.; Filonik, O.; Herzig, E. M.; Müller-Buschbaum, P.; Swamy, V.; Chien, S. T.; Mhaisalkar, S. G.; Mathews, N. Enhancing moisture tolerance in efficient hybrid 3D/2D perovskite photovoltaics. *J. Mater. Chem. A* **2018**, *6*, 2122–2128.

[26] Momma, K.; Izumi, F. VESTA 3 for Three-Dimensional Visulazation of Crystal, Volumetric and Morhpology Data. *J. Appl. Crystallogr.* **2011**, *44*, 1272–1276.

[27] Chen, T.; Foley, B. J.; Ipek, B.; Tyagi, M.; Copley, J. R. D.; Brown, C. M.; Choi, J. J.; Lee, S.-H. Rotational dynamics of organic cations in the $CH_3NH_3PbI_3$ perovskite. *Phys. Chem. Chem. Phys.* **2015**, *17*, 31278–31286.

[28] Zhang, D.; Hu, X.; Chen, T.; Abernathy, D. L.; Kajimoto, R.; Nakamura, M.; Kofu, M.; Foley, B. J.; Yoon, M.; Choi, J. J.; Lee, S.-H. Temporally decoherent and spatially coherent vibrations in metal halide perovskites. *Phys. Rev. B* **2020**, *102*, 224310.

[29] Lanigan-Atkins, T.; He, X.; Krogstad, M. J.; Pajerowski, D. M.; Abernathy, D. L.; Xu, G. N. M. N.; Xu, Z.; Chung, D. Y.; Kanatzidis, M. G.; Rosenkranz, S.; Osborn, R.; Delaire, O. Two-dimensional overdamped fluctuations of the soft perovskite lattice in $CsPbBr_3$. *Nat. Mater.* **2021**, *20*, 977–983.

[30] Yaffe, O.; Guo, Y.; Tan, L. Z.; Egger, D. A.; Hull, T.; Stoumpos, C. C.; Zheng, F.; Heinz, T. F.; Kronik, L.; Kanatzidis, M. G.; Owen, J. S.; Rappe, A. M.; Pimenta, M. A.; Brus, L. E. Local Polar Fluctuations in Lead Halide Perovskite Crystals. *Phys. Rev. Lett.* **2017**, *118*, 1–6.

[31] Schilcher, M. J.; Robinson, P. J.; Abramovitch, D. J.; Tan, L. Z.; Rappe, A. M.; Reichman, D. R.; Egger, D. A. The Significance of Polarons and Dynamic Disorder in Halide Perovskites. *ACS Energy Lett.* **2021**, *6*, 2162–2173.

[32] Cannelli, O.; Wiktor, J.; Colonna, N.; Leroy, L.; Puppin, M.; Bacellar, C.; Sadykov, I.; Krieg, F.; Smolentsev, G.; Kovalenko, M. V.; Pasquarello, A.; Chergui, M.; Mancini, G. F. Atomic-Level Description of Thermal Fluctuations in Inorganic Lead Halide Perovskites. *J. Phys. Chem. Lett.* **2022**, *13*, 3382–3391.

[33] Zhu, X. Y.; Podzorov, V. Charge Carriers in Hybrid Organic-Inorganic Lead Halide Perovskites Might Be Protected as Large Polarons. *J. Phys. Chem. Lett.* **2015**, *6*, 4758–4761.

[34] Zhu, H.; Miyata, K.; Fu, Y.; Wang, J.; Joshi, P. P.; Niesner, D.; Williams, K. W.; Jin, S.; Zhu, X.-Y. Screening in crystalline liquids protects energetic carriers in hybrid perovskites. *Science* **2016**, *353*, 1409–1413.

[35] Miyata, K.; Atallah, T. L.; Zhu, X. Y. Lead halide perovskites: Crystal-liquid duality, phonon glass electron crystals, and large polaron formation. *Sci. Adv.* **2017**, *3*, 1–11.

[36] Denis Romero, F.; Leach, A.; Möller, J. S.; Foronda, F.; Blundell, S. J.; Hayward, M. A. Strontium vanadium oxide-hydrides: "square-planar" two-electron phases. *Angew. Chemie - Int. Ed.* **2014**, *53*, 7556–7559.

[37] Yamamoto, T.; Zeng, D.; Kawakami, T.; Arcisauskaite, V.; Yata, K.; Patino, M. A.; Izumo, N.; McGrady, J. E.; Kageyama, H.; Hayward, M. A. The role of π-blocking hydride ligands in a pressure-induced insulator-to-metal phase transition in $SrVO_2H$. *Nat. Commun.* **2017**, *8*, 1217.

[38] Wei, Y.; Gui, H.; Li, X.; Zhao, Z.; Zhao, Y. H.; Xie, W. The effect of hydrogen ordering on the electronic and magnetic properties of the strontium vanadium oxyhydride. *J. Phys. Condens. Matter* **2015**, *27*, 206001.

[39] Kobayashi, Y. et al. An oxyhydride of $BaTiO_3$ exhibiting hydride exchange and electronic conductivity. *Nat. Mater.* **2012**, *11*, 507–511.

[40] Kobayashi, G.; Hinuma, Y.; Matsuoka, S.; Watanabe, A.; Iqbal, M.; Hirayama, M.; Yonemura, M.; Kamiyama, T.; Tanaka, I.; Kanno, R. Pure H^- conduction in oxyhydrides. *Science* **2016**, *351*, 1314–1317.

[41] Toriumi, H.; Kobayashi, G.; Saito, T.; Kamiyama, T.; Sakai, T.; Nomura, T.; Kitano, S.; Habazaki, H.; Aoki, Y. Barium Indate–Zirconate Perovskite Oxyhydride with Enhanced Hydride Ion/Electron Mixed Conductivity. *Chem. Mater.* **2022**, *34*, 7389–7401.

[42] Yajima, T.; Kitada, A.; Kobayashi, Y.; Sakaguchi, T.; Bouilly, G.; Kasahara, S.; Terashima, T.; Takano, M.; Kageyama, H. Epitaxial thin films of $ATiO_{3-x}H_x$ (A = Ba, Sr, Ca) with metallic conductivity. *J. Am. Chem. Soc.* **2012**, *134*, 8782–8785.

[43] Bridges, C. A.; Fernandez-Alonso, F.; Goff, J. P.; Rosseinsky, M. J. Observation of hydride mobility in the transition-metal oxide hydride $LaSrCoO_3H_{0.7}$. *Adv. Mater.* **2006**, *18*, 3304–3308.

[44] Eklöf-Österberg, C.; Nedumkandathil, R.; Häussermann, U.; Jaworski, A.; Pell, A. J.; Tyagi, M.; Jalarvo, N. H.; Frick, B.; Faraone, A.; Karlsson, M. Dynamics of Hydride Ions in Metal Hydride-Reduced $BaTiO_3$ Samples Investigated with Quasielastic Neutron Scattering. *J. Phys. Chem. C* **2019**, *123*, 2019–2030.

[45] Chen, T.; Chen, W. L.; Foley, B. J.; Lee, J.; Ruff, J. P.; Ko, J. Y.; Brown, C. M.; Harriger, L. W.; Zhang, D.; Park, C.; Yoon, M.; Chang, Y. M.; Choi, J. J.; Lee, S. H. Origin of long lifetime of band-edge charge carriers in organic–inorganic lead iodide perovskites. *Proc. Natl. Acad. Sci. U. S. A.* **2017**, *114*, 7519–7524.

[46] Correa-Baena, J. P.; Abate, A.; Saliba, M.; Tress, W.; Jesper Jacobsson, T.; Grätzel, M.; Hagfeldt, A. The rapid evolution of highly efficient perovskite solar cells. *Energy Environ. Sci.* **2017**, *10*, 710–727.

[47] Yang, W. S.; Jun Hong Noh, N. J. J.; Kim, Y. C.; Ryu, S.; Seo, J.; Seok, S. I. High-performance photovoltaic perovskite layers fabricated through intramolecular exchange. *Science (80-.).* **2015**, *348*, 2013–2017.

[48] Ke, W.; Kanatzidis, M. G. Prospects for low-toxicity lead-free perovskite solar cells. *Nat. Commun.* **2019**, *10*, 965.

[49] Marronnier, A.; Roma, G.; Boyer-Richard, S.; Pedesseau, L.; Jancu, J.-M.; Bonnassieux, Y.; Katan, C.; Stoumpos, C. C.; Kanatzidis, M. G.; Even, J. Anharmonicity and Disorder in the Black Phases of Cesium Lead Iodide Used for Stable Inorganic Perovskite Solar Cells. *ACS Nano* **2018**, *12*, 3477–3486.

[50] Drużbicki, K.; Lavén, R.; Armstrong, J.; Malavasi, L.; Fernandez-Alonso, F.; Karlsson, M. Cation Dynamics and Structural Stabilization in Formamidinium Lead Iodide Perovskites. *J. Phys. Chem. Lett.* **2021**, *12*, 3503–3508.

[51] Baikie, T.; Fang, Y.; Kadro, J. M.; Schreyer, M.; Wei, F.; Mhaisalkar, S. G.; Graetzel, M.; White, T. J. Synthesis and crystal chemistry of the hybrid perovskite $(CH_3NH_3)PbI_3$ for solid-state sensitised solar cell applications. *J. Mater. Chem. A* **2013**, *1*, 5628–5641.

[52] Weller, M. T.; Weber, O. J.; Henry, P. F.; Di Pumpo, A. M.; Hansen, T. C. Complete structure and cation orientation in the perovskite photovoltaic methylammonium lead iodide between 100 and 352 K. *Chem. Commun.* **2015**, *51*, 4180–4183.

[53] Druzbicki, K.; Pinna, R. S.; Rudić, S.; Jura, M.; Gorini, G.; Fernandez-Alonso, F. Unexpected Cation Dynamics in the Low-Temperature Phase of Methylammonium Lead Iodide: The Need for Improved Models. *J. Phys. Chem. Lett.* **2016**, *7*, 4701–4709.

[54] Rakita, Y.; Bar-Elli, O.; Meirzadeh, E.; Kaslasi, H.; Peleg, Y.; Hodes, G.; Lubomirsky, I.; Oron, D.; Ehre, D.; Cahen, D. Tetragonal $CH_3NH_3PbI_3$ is ferroelectric. *Proc. Natl. Acad. Sci. U. S. A.* **2017**, *114*, E5504–E5512.

[55] Breternitz, J.; Lehmann, F.; Barnett, S. A.; Nowell, H.; Schorr, S. Role of the Iodide–Methylammonium Interaction in the Ferroelectricity of $CH_3NH_3PbI_3$. *Angew. Chemie - Int. Ed.* **2020**, *59*, 424–428.

[56] Beecher, A. N.; Semonin, O. E.; Skelton, J. M.; Frost, J. M.; Terban, M. W.; Zhai, H.; Alatas, A.; Owen, J. S.; Walsh, A.; Billinge, S. J. L. Direct Observation of Dynamic Symmetry Breaking above Room Temperature in Methylammonium Lead Iodide Perovskite. *ACS Energy Lett.* **2016**, *1*, 880–887.

[57] Weadock, N. J.; Gehring, P. M.; Gold-Parker, A.; Smith, I. C.; Karunadasa, H. I.; Toney, M. F. Test of the Dynamic-Domain and Critical Scattering Hypotheses in Cubic Methylammonium Lead Triiodide. *Phys. Rev. Lett.* **2020**, *125*, 075701.

[58] Weber, O. J.; Ghosh, D.; Gaines, S.; Henry, P. F.; Walker, A. B.; Islam, M. S.; Weller, M. T. Phase Behavior and Polymorphism of Formamidinium Lead Iodide. *Chem. Mater.* **2018**, *30*, 3768–3778.

[59] Stoumpos, C. C.; Malliakas, C. D.; Kanatzidis, M. G. Semiconducting tin and lead iodide perovskites with organic cations: Phase transitions, high mobilities, and near-infrared photoluminescent properties. *Inorg. Chem.* **2013**, *52*, 9019–9038.

[60] Han, Q.; Bae, S. H.; Sun, P.; Hsieh, Y. T.; Yang, Y.; Rim, Y. S.; Zhao, H.; Chen, Q.; Shi, W.; Li, G.; Yeng, Y. Single Crystal Formamidinium Lead Iodide ($FAPbI_3$): Insight into the Structural, Optical, and Electrical Properties. *Adv. Mater.* **2016**, *28*, 2253–2258.

[61] Chen, T.; Foley, B. J.; Park, C.; Brown, C. M.; Harriger, L. W.; Lee, J.; Ruff, J.; Yoon, M.; Choi, J. J.; Lee, S.-H. Entropy-driven structural transition and kinetic trapping in formamidinium lead iodide perovskite. *Sci. Adv.* **2016**, *2*, e1601650.

[62] Weller, M. T.; Weber, O. J.; Frost, J. M.; Walsh, A. Cubic Perovskite Structure of Black Formamidinium Lead Iodide, α-$[HC(NH_2)_2]PbI_3$, at 298 K. *J. Phys. Chem. Lett.* **2015**, *6*, 3209–3212.

[63] Fabini, D. H.; Stoumpos, C. C.; Laurita, G.; Kaltzoglou, A.; Kontos, A. G.; Falaras, P.; Kanatzidis, M. G.; Seshadri, R. Reentrant Structural and Optical Properties and Large Positive Thermal Expansion in Perovskite Formamidinium Lead Iodide. *Angew. Chemie - Int. Ed.* **2016**, *55*, 15392–15396.

[64] Sun, S.; Deng, Z.; Wu, Y.; Wei, F.; Halis Isikgor, F.; Brivio, F.; Gaultois, M. W.; Ouyang, J.; Bristowe, P. D.; Cheetham, A. K.; Kieslich, G. Variable temperature and high-pressure crystal chemistry of perovskite formamidinium lead iodide: A single crystal X-ray diffraction and computational study. *Chem. Commun.* **2017**, *53*, 7537–7540.

[65] Fabini, D. H.; Hogan, T.; Evans, H. A.; Stoumpos, C. C.; Kanatzidis, M. G.; Seshadri, R. Dielectric and Thermodynamic Signatures of Low-Temperature Glassy Dynamics in the Hybrid Perovskites $CH_3NH_3PbI_3$ and $HC(NH_2)_2PbI_3$. *J. Phys. Chem. Lett.* **2016**, *7*, 376–381.

[66] Fabini, D. H.; Siaw, T. A.; Stoumpos, C. C.; Laurita, G.; Olds, D.; Page, K.; Hu, J. G.; Kanatzidis, M. G.; Han, S.; Seshadri, R. Universal Dynamics of Molecular Reorientation in Hybrid Lead Iodide Perovskites. *J. Am. Chem. Soc.* **2017**, *139*, 16875–16884.

[67] Lee, J. W.; Seol, D. J.; Cho, A. N.; Park, N. G. High-efficiency perovskite solar cells based on the black polymorph of $HC(NH_2)_2PbI_3$. *Adv. Mater.* **2014**, *26*, 4991–4998.

[68] Jesper Jacobsson, T.; Correa-Baena, J. P.; Pazoki, M.; Saliba, M.; Schenk, K.; Grätzel, M.; Hagfeldt, A. Exploration of the compositional space for mixed lead halogen perovskites for high efficiency solar cells. *Energy Environ. Sci.* **2016**, *9*, 1706–1724.

[69] Francisco-López, A.; Charles, B.; Alonso, M. I.; Garriga, M.; Campoy-Quiles, M.; Weller, M. T.; Goñi, A. R. Phase Diagram of Methylammonium/Formamidinium Lead Iodide Perovskite Solid Solutions from Temperature-Dependent Photoluminescence and Raman Spectroscopies. *J. Phys. Chem. C* **2020**, *124*, 3448–3458.

[70] Page, K.; Siewenie, J. E.; Quadrelli, P.; Malavasi, L. Short-Range Order of Methylammonium and Persistence of Distortion at the Local Scale in $MAPbBr_3$ Hybrid Perovskite. *Angew. Chemie - Int. Ed.* **2016**, *55*, 14320–14324.

[71] Morana, M.; Wiktor, J.; Coduri, M.; Chiara, R.; Giacobbe, C.; Bright, E. L.; Ambrosio, F.; De Angelis, F.; Malavasi, L. Cubic or Not Cubic? Combined Experimental and Computational Investigation of the Short-Range Order of Tin Halide Perovskites. *J. Phys. Chem. Lett.* **2023**, *14*, 2178–2186.

[72] Wells, H. L. Über die cäsium-und kalium-bleihalogenide. *Zeit. Anorg. Chem.* **1893**, *3*, 195–210.

[73] Møller, C. K. Crystal Structure and Photoconductivity of Cæsium Plumbohalides. *Nature* **1958**, *182*, 1436–1436.

[74] Møller, C. K. *The structure of cæsium plumbo iodide CsPbI3*; Munksgaard, 1959; Vol. 32.

[75] Goldschmidt, V. M. Die Gesetze der Krystallochemie. *Naturwissenschaften* **1926**, *14*, 477–485.

[76] Yang, R. X.; Skelton, J. M.; da Silva, E. L.; Frost, J. M.; Walsh, A. Assessment of dynamic structural instabilities across 24 cubic inorganic halide perovskites. *J. Chem. Phys.* **2020**, *152*, 024703.

[77] Sutton, R. J.; Filip, M. R.; Haghighirad, A. A.; Sakai, N.; Wenger, B.; Giustino, F.; Snaith, H. J. Cubic or orthorhombic? Revealing the crystal structure of metastable black-phase $CsPbI_3$ by theory and experiment. *ACS Energy Lett.* **2018**, *3*, 1787–1794.

[78] Trots, D.; Myagkota, S. High-temperature structural evolution of caesium and rubidium triiodoplumbates. *J. Phys. Chem. Solids* **2008**, *69*, 2520–2526.

[79] Dastidar, S.; Hawley, C. J.; Dillon, A. D.; Gutierrez-Perez, A. D.; Spanier, J. E.; Fafarman, A. T. Quantitative Phase-Change Thermodynamics and Metastability of Perovskite-Phase Cesium Lead Iodide. *J. Phys. Chem. Lett.* **2017**, *8*, 1278–1282.

[80] Liu, J.; Phillips, A. E.; Keen, D. A.; Dove, M. T. Thermal Disorder and Bond Anharmonicity in Cesium Lead Iodide Studied by Neutron Total Scattering and the Reverse Monte Carlo Method. *J. Phys. Chem. C* **2019**, *123*, 14934–14940.

[81] Straus, D. B.; Guo, S.; Cava, R. J. Kinetically Stable Single Crystals of Perovskite-Phase $CsPbI_3$. *J. Am. Chem. Soc.* **2019**, *141*, 11435–11439.

[82] Leguy, A. M.; Frost, J. M.; McMahon, A. P.; Sakai, V. G.; Kochelmann, W.; Law, C.; Li, X.; Foglia, F.; Walsh, A.; O'Regan, B. C.; Nelson, J.; Cabral, J. T.; Barnes, P. R. The dynamics of methylammonium ions in hybrid organic-inorganic perovskite solar cells. *Nat. Commun.* **2015**, *6*, 7124.

[83] Li, B.; Kawakita, Y.; Liu, Y.; Wang, M.; Matsuura, M.; Shibata, K.; Ohira-Kawamura, S.; Yamada, T.; Lin, S.; Nakajima, K.; Liu, S. F. Polar rotor scattering as atomic-level origin of low mobility and thermal conductivity of perovskite $CH_3NH_3PbI_3$. *Nat. Commun.* **2017**, *8*, 16086.

[84] Kubicki, D. J.; Prochowicz, D.; Hofstetter, A.; Péchy, P.; Zakeeruddin, S. M.; Grätzel, M.; Emsley, L. Cation Dynamics in Mixed-Cation $(MA)_x(FA)_{1-x}PbI_3$ Hybrid Perovskites from Solid-State NMR. *J. Am. Chem. Soc.* **2017**, *139*, 10055–10061.

[85] Taylor, V. C. A.; Tiwari, D.; Duchi, M.; Donaldson, P. M.; Clark, I. P.; Fermin, D. J.; Oliver, T. A. A. Investigating the Role of the Organic Cation in Formamidinium Lead Iodide Perovskite Using Ultrafast Spectroscopy. *J. Phys. Chem. Lett.* **2018**, *9*, 895–901.

[86] Mattoni, A.; Filippetti, A.; Saba, M. I.; Delugas, P. Methylammonium Rotational Dynamics in Lead Halide Perovskite by Classical Molecular Dynamics: The Role of Temperature. *J. Phys. Chem. C* **2015**, *119*, 17421–17428.

[87] Li, J.; Bouchard, M.; Reiss, P.; Aldakov, D.; Pouget, S.; Demadrille, R.; Aumaitre, C.; Frick, B.; Djurado, D.; Rossi, M.; Rinke, P. Activation Energy of Organic Cation Rotation in $CH_3NH_3PbI_3$ and $CD_3NH_3PbI_3$: Quasi-Elastic Neutron Scattering Measurements and First-Principles Analysis Including Nuclear Quantum Effects. *J. Phys. Chem. Lett.* **2018**, 3969–3977.

[88] Swainson, I. P.; Stock, C.; Parker, S. F.; Van Eijck, L.; Russina, M.; Taylor, J. W. From soft harmonic phonons to fast relaxational dynamics in $CH_3NH_3PbBr_3$. *Phys. Rev. B* **2015**, *92*, 2–6.

[89] Bakulin, A. A.; Selig, O.; Bakker, H. J.; Rezus, Y. L.; Müller, C.; Glaser, T.; Lovrincic, R.; Sun, Z.; Chen, Z.; Walsh, A.; Frost, J. M.; Jansen, T. L. Real-Time Observation of Organic Cation Reorientation in Methylammonium Lead Iodide Perovskites. *J. Phys. Chem. Lett.* **2015**, *6*, 3663–3669.

[90] Mozur, E. M.; Maughan, A. E.; Cheng, Y.; Huq, A.; Jalarvo, N.; Daemen, L. L.; Neilson, J. R. Orientational Glass Formation in Substituted Hybrid Perovskites. *Chem. Mater.* **2017**, *29*, 10168–10177.

[91] Bernard, G. M.; Wasylishen, R. E.; Ratcliffe, C. I.; Terskikh, V.; Wu, Q.; Buriak, J. M.; Hauger, T. Methylammonium Cation Dynamics in Methylammonium Lead Halide Perovskites: A Solid-State NMR Perspective. *J. Phys. Chem. A* **2018**, *122*, 1560–1573.

[92] Johnston, A.; Walters, G.; Saidaminov, M. I.; Huang, Z.; Bertens, K.; Jalarvo, N.; Sargent, E. H. Bromine Incorporation and Suppressed Cation Rotation in Mixed-Halide Perovskites. *ACS Nano* **2020**, *14*, 15107–15118.

[93] Munson, K. T.; Swartzfager, J. R.; Gan, J.; Asbury, J. B. Does Dipolar Motion of Organic Cations Affect Polaron Dynamics and Bimolecular Recombination in Halide Perovskites? *J. Phys. Chem. Lett.* **2020**, *11*, 3166–3172.

[94] Munson, K. T.; Asbury, J. B. Influence of Dynamic Disorder and Charge–Lattice Interactions on Optoelectronic Properties of Halide Perovskites. *J. Phys. Chem. C* **2021**, *125*, 5427–5435.

[95] Ma, J.; Wang, L.-W. Nanoscale charge localization induced by random orientations of organic molecules in hybrid perovskite $CH_3NH_3PbI_3$. *Nano Lett.* **2015**, *15*, 248–253.

[96] Quarti, C.; Mosconi, E.; De Angelis, F. Structural and electronic properties of organo-halide hybrid perovskites from ab initio molecular dynamics. *Phys. Chem. Chem. Phys.* **2015**, *17*, 9394–9409.

[97] Koda, A.; Okabe, H.; Hiraishi, M.; Kadono, R.; Dagnall, K. A.; Choi, J. J.; Lee, S.-H. Organic molecular dynamics and charge-carrier lifetime in lead iodide perovskite $MAPbI_3$. *Proc. Natl. Acad. Sci. U. S. A.* **2022**, *119*, e2115812119.

[98] Brown, K. L.; Parker, S. F.; García, I. R.; Mukhopadhyay, S.; Sakai, V. G.; Stock, C. Molecular orientational melting within a lead-halide octahedron framework: The order-disorder transition in $CH_3NH_3PbBr_3$. *Phys. Rev. B* **2017**, *96*, 1–10.

[99] Schuck, G.; Lehmann, F.; Ollivier, J.; Mutka, H.; Schorr, S. Influence of Chloride Substitution on the Rotational Dynamics of Methylammonium in $MAPbI_{3-x}Cl_x$ Perovskites. *J. Phys. Chem. C* **2019**, *123*, 11436–11446.

[100] Songvilay, M.; Wang, Z.; Sakai, V. G.; Guidi, T.; Bari, M.; Ye, Z.-G.; Xu, G.; Brown, K. L.; Gehring, P. M.; Stock, C. Decoupled molecular and inorganic framework dynamics in $CH_3NH_3PbCl_3$. *Phys. Rev. Materials* **2019**, *3*, 125406.

[101] Sharma, V. K.; Mukhopadhyay, R.; Mohanty, A.; Tyagi, M.; Embs, J. P.; Sarma, D. D. Contrasting Behaviors of FA and MA Cations in APbBr$_3$. *J. Phys. Chem. Lett.* **2020**, *11*, 9669–9679.

[102] Lavén, R.; Koza, M. M.; Malavasi, L.; Perrichon, A.; Appel, M.; Karlsson, M. Rotational Dynamics of Organic Cations in Formamidinium Lead Iodide Perovskites. *J. Phys. Chem. Lett.* **2023**, *14*, 2784–2791.

[103] Mozur, E. M.; Trowbridge, J. C.; Maughan, A. E.; Gorman, M. J.; Brown, C. M.; Prisk, T. R.; Neilson, J. R. Dynamical Phase Transitions and Cation Orientation-Dependent Photoconductivity in $CH(NH_2)_2PbBr_3$. *ACS Materials Lett.* **2019**, *1*, 260–264.

[104] Mozur, E. M.; Hope, M. A.; Trowbridge, J. C.; Halat, D. M.; Daemen, L. L.; Maughan, A. E.; Prisk, T. R.; Grey, C. P.; Neilson, J. R. Cesium Substitution Disrupts Concerted Cation Dynamics in Formamidinium Hybrid Perovskites. *Chem. Mater.* **2020**, *32*, 6266–6277.

[105] Taylor, V. C. A.; Tiwari, D.; Duchi, M.; Donaldson, P. M.; Clark, I. P.; Fermin, D. J.; Oliver, T. A. A. Investigating the Role of the Organic Cation in Formamidinium Lead Iodide Perovskite Using Ultrafast Spectroscopy. *J. Phys. Chem. Lett.* **2018**, *9*, 895–901.

[106] Fisicaro, G.; La Magna, A.; Alberti, A.; Smecca, E.; Mannino, G.; Deretzis, I. Local Order and Rotational Dynamics in Mixed A-Cation Lead Iodide Perovskites. *J. Phys. Chem. Lett.* **2020**, *11*, 1068–1074.

[107] Mishra, A.; Hope, M. A.; Grätzel, M.; Emsley, L. A Complete Picture of Cation Dynamics in Hybrid Perovskite Materials from Solid-State NMR Spectroscopy. *J. Am. Chem. Soc.* **2023**, *145*, 978–990.

[108] Shapiro, S. M.; Axe, J. D.; Shirane, G.; Riste, T. Critical Neutron Scattering in $SrTiO_3$ and $KMnF_3$. *Phys. Rev. B* **1972**, *6*, 4332–4341.

[109] Fleury, P. A.; Scott, J. F.; Worlock, J. M. Soft Phonon Modes and the 110°K Phase Transition in $SrTiO_3$. *Phys. Rev. Lett.* **1968**, *21*, 16–19.

[110] Fujii, Y.; Hoshino, S.; Yamada, Y.; Shirane, G. Neutron-scattering study on phase transitions of $CsPbCl_3$. *Phys. Rev. B* **1974**, *9*, 4549–4559.

[111] Fransson, E.; Rosander, P.; Eriksson, F.; Rahm, J. M.; Tadano, T.; Erhart, P. Probing the limits of the phonon quasi-particle picture: The transition from underdamped to overdamped dynamics in $CsPbBr_3$. *arXiv preprint arXiv:2211.08197* **2022**,

[112] Wiktor, J.; Fransson, E.; Kubicki, D.; Erhart, P. Quantifying Dynamic Tilting in Halide Perovskites: Chemical Trends and Local Correlations. *arXiv preprint arXiv:2304.07402* **2023**,

[113] Baldwin, W.; Liang, X.; Klarbring, J.; Dubajic, M.; Dell'Angelo, D.; Sutton, C.; Caddeo, C.; Stranks, S. D.; Mattoni, A.; Walsh, A., et al. Dynamic Local Structure in Caesium Lead Iodide: Spatial Correlation and Transient Domains. *arXiv preprint arXiv:2304.04714* **2023**,

[114] Liu, J.; Du, J.; Phillips, A. E.; Wyatt, P. B.; Keen, D. A.; Dove, M. T. Neutron powder diffraction study of the phase transitions in deuterated methylammonium lead iodide. *J. Phys.: Condens. Matter* **2022**, *34*, 145401.

[115] Hehlen, B.; Bourges, P.; Rufflé, B.; Clément, S.; Vialla, R.; Ferreira, A. C.; Ecolivet, C.; Paofai, S.; Cordier, S.; Katan, C.; Létoublon, A.; Even, J. Pseudospin-phonon pretransitional dynamics in lead halide hybrid perovskites. *Phys. Rev. B* **2022**, *105*, 024306.

[116] Calabrese, J.; Jones, N. L.; Harlow, R. L.; Herron, N.; Thorn, D. L.; Wang, Y. Preparation and Characterization of Layered Lead Halide Compounds. *J. Am. Chem. Soc.* **1991**, *113*, 2328–2330.

[117] Straus, D. B.; Iotov, N.; Gau, M. R.; Zhao, Q.; Carroll, P. J.; Kagan, C. R. Longer Cations Increase Energetic Disorder in Excitonic 2D Hybrid Perovskites. *J. Phys. Chem. Lett.* **2019**, *10*, 1198–1205.

[118] Du, K.-z.; Tu, Q.; Zhang, X.; Han, Q.; Liu, J.; Zauscher, S.; Mitzi, D. B. Two-dimensional lead (II) halide-based hybrid perovskites templated by acene alkylamines: crystal structures, optical properties, and piezoelectricity. *Inorg. Chem.* **2017**, *56*, 9291–9302.

[119] Menahem, M.; Dai, Z.; Aharon, S.; Sharma, R.; Asher, M.; Diskin-Posner, Y.; Korobko, R.; Rappe, A. M.; Yaffe, O. Strongly Anharmonic Octahedral Tilting in Two-Dimensional Hybrid Halide Perovskites. *ACS Nano* **2021**, *15*, 10153–10162.

[120] Febriansyah, B.; Koh, T. M.; Lekina, Y.; Jamaludin, N. F.; Bruno, A.; Ganguly, R.; Shen, Z. X.; Mhaisalkar, S. G.; England, J. Improved photovoltaic efficiency and amplified photocurrent generation in mesoporous n= 1 two-dimensional lead–iodide perovskite solar cells. *Chem. Mater.* **2019**, *31*, 890–898.

[121] Song, J.; Dang, Y.; Liu, X. L.; Tao, X. Layered hybrid lead perovskite single crystals: phase transformations and tunable optical properties. *CrystEngComm* **2020**, *22*, 6310–6315.

[122] Billing, D. G.; Lemmerer, A. Synthesis, characterization and phase transitions in the inorganic-organic layered perovskite-type hybrids $[(C_nH_{2n+1}NH_3)_2PbI_4]$, $n = 4$, 5 and 6. *Acta Crystallogr. Sect. B Struct. Sci.* **2007**, *63*, 735–747.

[123] Thouin, F.; Valverde-Chávez, D. A.; Quarti, C.; Cortecchia, D.; Bargigia, I.; Beljonne, D.; Petrozza, A.; Silva, C.; Srimath Kandada, A. R. Phonon coherences reveal the polaronic character of excitons in two-dimensional lead halide perovskites. *Nat. Mater.* **2019**, *18*, 349–356.

[124] Esmaielpour, H.; Whiteside, V. R.; Sourabh, S.; Eperon, G. E.; Precht, J. T.; Beard, M. C.; Lu, H.; Durant, B. K.; Sellers, I. R. Role of Exciton Binding Energy on LO Phonon Broadening and Polaron Formation in $(BA)_2PbI_4$ Ruddlesden-Popper Films. *J. Phys. Chem. C* **2020**, *124*, 9496–9505.

[125] Mauck, C. M.; France-Lanord, A.; Hernandez Oendra, A. C.; Dahod, N. S.; Grossman, J. C.; Tisdale, W. A. Inorganic Cage Motion Dominates Excited-State Dynamics in 2D-Layered Perovskites $(C_xH_{2x+1}NH_3)_2PbI_4$ (x = 4-9). *J. Phys. Chem. C* **2019**, *123*, 27904–27916.

[126] Thouin, F.; Srimath Kandada, A. R.; Valverde-Chávez, D. A.; Cortecchia, D.; Bargigia, I.; Petrozza, A.; Yang, X.; Bittner, E. R.; Silva, C. Electron-Phonon Couplings Inherent in Polarons Drive Exciton Dynamics in Two-Dimensional Metal-Halide Perovskites. *Chem. Mater.* **2019**, *31*, 7085–7091.

[127] Gong, X.; Voznyy, O.; Jain, A.; Liu, W.; Sabatini, R.; Piontkowski, Z.; Walters, G.; Bappi, G.; Nokhrin, S.; Bushuyev, O.; Yuan, M.; Comin, R.; McCamant, D.; Kelley, S. O.; Sargent, E. H. Electron-phonon interaction in efficient perovskite blue emitters. *Nat. Mater.* **2018**, *17*, 550–556.

[128] Urban, J. M.; Chehade, G.; Dyksik, M.; Menahem, M.; Surrente, A.; Trippé-Allard, G.; Maude, D. K.; Garrot, D.; Yaffe, O.; Deleporte, E.; Plochocka, P.; Baranowski, M. Revealing Excitonic Phonon Coupling in $(PEA)_2(MA)_{n-1}PbnI_{3n+1}$ 2D Layered Perovskites. *J. Phys. Chem. Lett.* **2020**, *11*, 5830–5835.

[129] Srimath Kandada, A. R.; Silva, C. Exciton Polarons in Two-Dimensional Hybrid Metal-Halide Perovskites. *J. Phys. Chem. Lett.* **2020**, *11*, 3173–3184.

[130] Thouin, F.; Neutzner, S.; Cortecchia, D.; Dragomir, V. A.; Soci, C.; Salim, T.; Lam, Y. M.; Leonelli, R.; Petrozza, A.; Kandada, A. R. S.; Silva, C. Stable biexcitons in two-dimensional metal-halide perovskites with strong dynamic lattice disorder. *Phys. Rev. Mater.* **2018**, *2*, 1–10.

[131] Blancon, J. C.; Even, J.; Stoumpos, C. C.; Kanatzidis, M. G.; Mohite, A. D. Semiconductor physics of organic–inorganic 2D halide perovskites. *Nat. Nanotechnol.* **2020**, *15*, 969–985.

[132] Dahod, N. S.; Paritmongkol, W.; Stollmann, A.; Settens, C.; Zheng, S. L.; Tisdale, W. A. Melting Transitions of the Organic Subphase in Layered Two-Dimensional Halide Perovskites. *J. Phys. Chem. Lett.* **2019**, *10*, 2924–2930.

[133] Nishida, J.; Breen, J. P.; Lindquist, K. P.; Umeyama, D.; Karunadasa, H. I.; Fayer, M. D. Dynamically Disordered Lattice in a Layered Pb-I-SCN Perovskite Thin Film Probed by Two-Dimensional Infrared Spectroscopy. *J. Am. Chem. Soc.* **2018**, *140*, 9882–9890.

[134] Kang, J.; Wang, L. W. Dynamic Disorder and Potential Fluctuation in Two-Dimensional Perovskite. *J. Phys. Chem. Lett.* **2017**, *8*, 3875–3880.

[135] Koegel, A. A.; Mozur, E. M.; Oswald, I. W.; Jalarvo, N. H.; Prisk, T. R.; Tyagi, M.; Neilson, J. R. Correlating Broadband Photoluminescence with Structural Dynamics in Layered Hybrid Halide Perovskites. *J. Am. Chem. Soc.* **2022**, *144*, 1313–1322.

[136] Ghosh, D.; Neukirch, A. J.; Tretiak, S. Optoelectronic Properties of Two-Dimensional Bromide Perovskites: Influences of Spacer Cations. *J. Phys. Chem. Lett.* **2020**, *11*, 2955–2964.

[137] Dahlman, C. J.; Kennard, R. M.; Paluch, P.; Venkatesan, N. R.; Chabinyc, M. L.; Manjunatha Reddy, G. N. Dynamic Motion of Organic Spacer Cations in Ruddlesden-Popper Lead Iodide Perovskites Probed by Solid-State NMR Spectroscopy. *Chem. Mater.* **2021**, *33*, 642–656.

[138] Hu, X.; Zhang, D.; Chen, T.; Chen, A. Z.; Holmgren, E. N.; Zhang, Q.; Pajerowski, D. M.; Yoon, M.; Xu, G.; Choi, J. J.; Lee, S. H. Crystal structures and rotational dynamics of a two-dimensional metal halide perovskite $(OA)_2PbI_4$. *J. Chem. Phys.* **2020**, *152*, 014703.

[139] Sanni, A. M.; Lavan, S. N.; Rury, A. S. Anharmonic Molecular Vibrational Probes of Dynamical Organic-Inorganic Interactions in Two-Dimensional Hybrid Lead Iodide Perovskites. *J. Phys. Chem. C* **2020**, *124*, 13942–13955.

[140] Ueda, T.; Shimizu, K.; Ohki, H.; Okuda, T. 13C CP/MAS NMR study of the layered compounds $[C_6H_5CH_2CH_2NH_3]_2[CH_3NH_3]_{n-1}Pb_nI_{3n+1}$ ($n = 1, 2$). *Z. Naturforsch. A* **1996**, *51*, 910–914.

[141] Lyu, F.; Zheng, X.; Li, Z.; Chen, Z.; Shi, R.; Wang, Z.; Liu, H.; Lin, B. L. Spatiodynamics, Photodynamics, and Their Correlation in Hybrid Perovskites. *Chem. Mater.* **2021**, *33*, 3524–3533.

[142] Lekina, Y.; Dintakurti, S. S.; Febriansyah, B.; Bradley, D.; Yan, J.; Shi, X.; England, J.; White, T.; Hanna, J. V.; Shen, Z. X. The effect of organic cation dynamics on the optical properties in $(PEA)_2(MA)[Pb_2I_7]$ perovskite dimorphs. *J. Mater. Chem. C* **2021**, *9*, 17050–17060.

[143] Lin, C. C.; Huang, S. J.; Wu, P. H.; Chen, T. P.; Huang, C. Y.; Wang, Y. C.; Chen, P. T.; Radeva, D.; Petrov, O.; Gelev, V. M.; Sankar, R.; Chen, C. C.; Chen, C. W.; Yu, T. Y. Direct investigation of the reorientational dynamics of A-site cations in 2D organic-inorganic hybrid perovskite by solid-state NMR. *Nat. Commun.* **2022**, *13*, 1–10.

[144] Hayward, M. A.; Cussen, E. J.; Claridge, J. B.; Bieringer, M.; Rosseinsky, M. J.; Kiely, C. J.; Blundell, S. J.; Marshall, I. M.; Pratt, F. L. The hydride anion in an extended transition metal oxide array: $LaSrCoO_3H_{0.7}$. *Science* **2002**, *295*, 1882–1884.

[145] Bridges, C. A.; Darling, G. R.; Hayward, M. A.; Rosseinsky, M. J. Electronic Structure, Magnetic Ordering, and Formation Pathway of the Transition Metal Oxide Hydride $LaSrCoO_3H_{0.7}$. *J. Am. Chem. Soc.* **2005**, *127*, 5996–6011.

[146] Helps, R. M.; Rees, N. H.; Hayward, M. A. $Sr_3Co_2O_{4.33}H_{0.84}$: an extended transition metal oxide-hydride. *Inorg. Chem.* **2010**, *49*, 11062–11068.

[147] Bowman, A.; Claridge, J.; Rosseinsky, M. Anion composition control and magnetic short-and long-range order in transition metal oxide hydrides. *Chem. Mater.* **2006**, *18*, 3046–3056.

[148] Hayward, M.; Green, M.; Rosseinsky, M.; Sloan, J. Sodium hydride as a powerful reducing agent for topotactic oxide deintercalation: synthesis and characterization of the nickel (I) oxide $LaNiO_2$. *J. Am. Chem. Soc.* **1999**, *121*, 8843–8854.

[149] Tsujimoto, Y.; Tassel, C.; Hayashi, N.; Watanabe, T.; Kageyama, H.; Yoshimura, K.; Takano, M.; Ceretti, M.; Ritter, C.; Paulus, W. Infinite-layer iron oxide with a square-planar coordination. *Nature* **2007**, *450*, 1062–1065.

[150] Yamamoto, T.; Kageyama, H. Hydride Reductions of Transition Metal Oxides. *Chem. Lett.* **2013**, *42*, 946–953.

[151] Kageyama, H.; Yajima, T.; Tsujimoto, Y.; Yamamoto, T.; Tassel, C.; Kobayashi, Y. Exploring Structures and Properties through Anion Chemistry. *Bull. Chem. Soc. Jpn.* **2019**, *92*, 1349–1357.

[152] Sakaguchi, T. et al. Oxyhydrides of (Ca,Sr,Ba)TiO_3 Perovskite Solid Solutions. *Inorg. Chem.* **2012**, *51*, 11371–11376.

[153] Tassel, C.; Goto, Y.; Kuno, Y.; Hester, J.; Green, M.; Kobayashi, Y.; Kageyama, H. Direct synthesis of chromium perovskite oxyhydride with a high magnetic-transition temperature. *Angew. Chemie - Int. Ed.* **2014**, *53*, 10377–10380.

[154] Ochi, M.; Kuroki, K. Quantifying the stability of the anion ordering in $SrVO_2H$. *Phys. Rev. B* **2020**, *102*, 134108.

[155] Lavén, R.; Häussermann, U.; Perrichon, A.; Andersson, M. S.; Targama, M. S.; Demmel, F.; Karlsson, M. Diffusional Dynamics of Hydride Ions in the Layered Oxyhydride $SrVO_2H$. *Chem. Mater.* **2021**, *33*, 2967–2975.

[156] Kobayashi, Y.; Hernandez, O.; Tassel, C.; Kageyama, H. New chemistry of transition metal oxyhydrides. *Sci. Technol. Adv. Mater.* **2017**, *18*, 905–918.

[157] Liu, S.; Wang, L.; Lin, W. C.; Sucharitakul, S.; Burda, C.; Gao, X. P. Imaging the Long Transport Lengths of Photo-generated Carriers in Oriented Perovskite Films. *Nano Lett.* **2016**, *16*, 7925–7929.

[158] Jin, L.; Lane, M.; Zeng, D.; Kirschner, F. K.; Lang, F.; Manuel, P.; Blundell, S. J.; McGrady, J. E.; Hayward, M. A. $LaSr_3NiRuO_4H_4$: A 4d Transition-Metal Oxide–Hydride Containing Metal Hydride Sheets. *Angew. Chemie - Int. Ed.* **2018**, *57*, 5025–5028.

[159] Jin, L.; Hayward, M. A. Rhodium-containing oxide-hydrides: covalently stabilized mixed-anion solids. *Chem. Commun.* **2019**, *55*, 4861–4864.

[160] Tassel, C.; Goto, Y.; Watabe, D.; Tang, Y.; Lu, H.; Kuno, Y.; Takeiri, F.; Yamamoto, T.; Brown, C. M.; Hester, J.; Kobayashi, Y.; Kageyama, H. High-Pressure Synthesis of Manganese Oxyhydride with Partial Anion Order. *Angew. Chemie - Int. Ed.* **2016**, *55*, 9667–9670.

[161] Masuda, N.; Kobayashi, Y.; Hernandez, O.; Bataille, T.; Paofai, S.; Suzuki, H.; Ritter, C.; Ichijo, N.; Noda, Y.; Takegoshi, K.; Tassel, C.; Yamamoto, T.; Kageyama, H. Hydride in $BaTiO_{2.5}H_{0.5}$: A Labile Ligand in Solid State Chemistry. *J. Am. Chem. Soc.* **2015**, *137*, 15315–15321.

[162] Yajima, T.; Takeiri, F.; Aidzu, K.; Akamatsu, H.; Fujita, K.; Yoshimune, W.; Ohkura, M.; Lei, S.; Gopalan, V.; Tanaka, K.; Brown, C. M.; Green, M. A.; Yamamoto, T.; Kobayashi, Y.; Kageyama, H. A labile hydride strategy for the synthesis of heavily nitridized $BaTiO_3$. *Nat. Chem.* **2015**, *7*, 1017–1023.

[163] Zhang, J.; Gou, G.; Pan, B. Study of phase stability and hydride diffusion mechanism of $BaTiO_3$ oxyhydride from first-principles. *J. Phys. Chem. C* **2014**, *118*, 17254–17259.

[164] Tang, Y.; Kobayashi, Y.; Shitara, K.; Konishi, A.; Kuwabara, A.; Nakashima, T.; Tassel, C.; Yamamoto, T.; Kageyama, H. On Hydride Diffusion in Transition Metal Perovskite Oxyhydrides Investigated via Deuterium Exchange. *Chem. Mater.* **2017**, *29*, 8187–8194.

[165] Liu, X.; Bjørheim, T. S.; Haugsrud, R. Formation and migration of hydride ions in $BaTiO_{3-x}H_x$ oxyhydride. *J. Mater. Chem. A* **2017**, *5*, 1050–1056.

[166] Liu, X.; Bjørheim, T. S.; Vines, L.; Fjellvåg, Ø. S.; Granerød, C.; Prytz, Ø.; Yamamoto, T.; Kageyama, H.; Norby, T.; Haugsrud, R. Highly Correlated Hydride Ion Tracer Diffusion in $SrTiO_{3-x}H_x$ Oxyhydrides. *J. Am. Chem. Soc.* **2019**, *141*, 4653–4659.

[167] Yamaguchi, S. Large, soft, and polarizable hydride ions sneak around in an oxyhydride. *Science* **2016**, *351*, 1262–1263.

[168] Takeiri, F. et al. Hydride-ion-conducting K_2NiF_4-type Ba–Li oxyhydride solid electrolyte. *Nat. Mater.* **2022**, *21*, 325–330.

[169] Squires, G. L. *Introduction to the Theory of Thermal Neutron Scattering*; Cambridge University Press, 1978.

[170] Lovesey, S. W. *Theory of Neutron Scattering from Condensed Matter Vol. I.*; Clarendon Press, 1984.

[171] Hempelmann, R. *Quasielastic Neutron Scattering and Solid State Diffusion*; Oxford University Press, 2000.

[172] Demmel, F. Quasielastic neutron scattering. https://www.isis.stfc.ac.uk/Pages/quasi-elastic-neutron-scattering13583.pdf, 2013; Accessed: 2021-05-23.

[173] Van Hove, L. Correlations in Space and Time and Born Approximation Scattering in Systems of Interacting Particles. *Phys. Rev.* **1954**, *95*, 249–262.

[174] Mitchell, P. C. H.; Parker, S. F.; Ramirez-Cuezta, A. J.; Tomkinson, J. *Vibrational Spectroscopy with Neutrons*; Word Scientific, 2005.

[175] Furrer, A.; Mesot, J.; Strässle, T. *Neutron Scattering in Condensed Matter Physics*; World Scientific, 2009.

[176] Chazallon, B.; Itoh, H.; Koza, M.; Kuhs, W. F.; Schober, H. Anharmonicity and guest-host coupling in clathrate hydrates. *Phys. Chem. Chem. Phys.* **2002**, *4*, 4809–4816.

[177] Togo, A. Phonon Database at Kyoto University. http://phonondb.mtl.kyoto-u.ac.jp, Accessed: 2022-05-23.

[178] Cheng, Y.; Daemen, L. L.; Kolesnikov, A. I.; Ramirez-Cuesta, A. J. Simulation of inelastic neutron scattering spectra using OCLIMAX. *J. Chem. Theory Comput.* **2019**, *15*, 1974–1982.

[179] Fåk, B.; Dorner, B. Phonon line shapes and excitation energies. *Physica B Condens. Matter* **1997**, *234*, 1107–1108.

[180] Fransson, E.; Slabanja, M.; Erhart, P.; Wahnström, G. dynasor—A Tool for Extracting Dynamical Structure Factors and Current Correlation Functions from Molecular Dynamics Simulations. *Adv. Theory Simul.* **2021**, *4*, 2000240.

[181] Bée, M. *Quasielastic Neutron Scattering: Principles and Applications in Solid State Chemistry, Biology and Materials Science*; Adam Hilger, 1988.

[182] Chudley, C. T.; Elliot, R. J. Neutron Scattering From a Liquid on a Jump Diffusion Model. *Proc. Phys. Soc.* **1961**, *77*, 353–361.

[183] IN5, Institut Laue Langevin. https://www.ill.eu/users/instruments/instruments-list/in5/description/instrument-layout, Accessed: 2023-04-26.

[184] Richard, D.; Ferrand, M.; Kearley, G. J. Analysis and visualisation of neutron-scattering data. *J. Neutron Res.* **1996**, *4*, 33–39.

[185] Web Site for Neutron Backscattering Spectroscopy. https://ah-backscattering.pagesperso-orange.fr, Accessed: 2021-05-22.

[186] Frick, B.; Mamontov, E.; van Eijck, L.; Seydel, T. Recent Backscattering Instrument Developments at the ILL and SNS. *Z. Phys. Chem.* **2010**, *224*, 33–60.

[187] IN16B, Institut Laue Langevin. https://www.ill.eu/users/instruments/instruments-list/in16b/description/instrument-layout, Accessed: 2021-05-21.

[188] Frick, B.; Combet, J.; van Eijck, L. New possibilities with inelastic fixed window scans and linear motor Doppler drives on high resolution neutron backscattering spectrometers. *Nuclear Inst. and Methods in Physics Research, A* **2012**, *669*, 7–13.

[189] Alsalloum, A. Y.; Turedi, B.; Almasabi, K.; Zheng, X.; Naphade, R.; Stranks, S. D.; Mohammed, O. F.; Bakr, O. M. 22.8%-Efficient single-crystal mixed-cation inverted perovskite solar cells with a near-optimal bandgap. *Energy Environ. Sci.* **2021**, *14*, 2263–2268.

[190] Pinna, R. S.; Rudić, S.; Parker, S. F.; Armstrong, J.; Zanetti, M.; Škoro, G.; Waller, S. P.; Zacek, D.; Smith, C. A.; Capstick, M. J.; McPhail, D. J.; Pooley, D. E.; Howells, G. D.; Gorini, G.; Fernandez-Alonso, F. The neutron guide upgrade of the TOSCA spectrometer. *Nuclear Inst. and Methods in Physics Research, A* **2018**, *896*, 68–74.

[191] Ferreira, A. C.; Paofai, S.; Létoublon, A.; Ollivier, J.; Raymond, S.; Hehlen, B.; Rufflé, B.; Cordier, S.; Katan, C.; Even, J.; Bourges, P. Direct evidence of weakly dispersed and strongly anharmonic optical phonons in hybrid perovskites. *Commun. Phys.* **2020**, *3*, 48.

[192] Chumakov, A.; Monaco, G.; Monaco, A.; Crichton, W.; Bosak, A.; Rüffer, R.; Meyer, A.; Kargl, F.; Comez, L.; Fioretto, D., et al. Equivalence of the boson peak in glasses to the transverse acoustic van hove singularity in crystals. *Phys. Rev. Lett* **2011**, *106*, 225501.

[193] Zaccone, A.; Baggioli, M. Universal law for the vibrational density of states of liquids. *Proc. Natl. Acad. Sci. U.S.A.* **2021**, *118*, e2022303118.

[194] Miyata, K.; Zhu, X. Y. Ferroelectric large polarons. *Nat. Mater.* **2018**, *17*, 379–381.

[195] Songvilay, M.; Giles-Donovan, N.; Bari, M.; Ye, Z.-G.; Minns, J. L.; Green, M. A.; Xu, G.; Gehring, P. M.; Schmalzl, K.; Ratcliff, W. D.; Brown, C. M.; Chernyshov, D.; van Beek, W.; Cochran, S.; Stock, C. Common acoustic phonon lifetimes in inorganic and hybrid lead halide perovskites. *Phys. Rev. Materials* **2019**, *3*, 093602.

[196] Sharma, R.; Dai, Z.; Gao, L.; Brenner, T. M.; Yadgarov, L.; Zhang, J.; Rakita, Y.; Korobko, R.; Rappe, A. M.; Yaffe, O. Elucidating the atomistic origin of anharmonicity in tetragonal $CH_3NH_3PbI_3$ with Raman scattering. *Phys. Rev. Materials* **2020**, *4*, 092401.

[197] Ishioka, K.; Tadano, T.; Yanagida, M.; Shirai, Y.; Miyano, K. Anharmonic organic cation vibrations in the hybrid lead halide perovskite $CH_3NH_3PbI_3$. *Phys. Rev. Materials* **2021**, *5*, 105402.

[198] La Nave, E.; Scala, A.; Starr, F. W.; Sciortino, F.; Stanley, H. E. Instantaneous Normal Mode Analysis of Supercooled Water. *Phys. Rev. Lett.* **2000**, *84*, 4605–4608.

[199] Stamper, C.; Cortie, D.; Yue, Z.; Wang, X.; Yu, D. Experimental Confirmation of the Universal Law for the Vibrational Density of States of Liquids. *J. Phys. Chem. Lett.* **2022**, *13*, 3105–3111.

[200] Wang, F.; Fu, Y.; Ziffer, M. E.; Dai, Y.; Maehrlein, S. F.; Zhu, X.-Y. Solvated Electrons in Solids—Ferroelectric Large Polarons in Lead Halide Perovskites. *J. Am. Chem. Soc.* **2021**, *143*, 5–16.

[201] Gold-Parker, A.; Gehring, P. M.; Skelton, J. M.; Smith, I. C.; Parshall, D.; Frost, J. M.; Karunadasa, H. I.; Walsh, A.; Toney, M. F. Acoustic phonon lifetimes limit thermal transport in methylammonium lead iodide. *Proc. Natl. Acad. Sci. U.S.A.* **2018**, *115*, 11905–11910.

[202] Ferreira, A. C.; Létoublon, A.; Paofai, S.; Raymond, S.; Ecolivet, C.; Rufflé, B.; Cordier, S.; Katan, C.; Saidaminov, M. I.; Zhumekenov, A. A.; Bakr, O. M.; Even, J.; Bourges, P. Elastic Softness of Hybrid Lead Halide Perovskites. *Phys. Rev. Lett.* **2018**, *121*, 1–12.

[203] Yuan, Y.; Liu, X.-F.; Ma, X.; Wang, X.; Li, X.; Xiao, J.; Li, X.; Zhang, H.-L.; Wang, L. Large band gap narrowing and prolonged carrier lifetime of $(C_4H_9NH_3)_2PbI_4$ under high pressure. *Adv. Sci.* **2019**, *6*, 1900240.

[204] Fang, H.-H.; Yang, J.; Adjokatse, S.; Tekelenburg, E.; Kamminga, M. E.; Duim, H.; Ye, J.; Blake, G. R.; Even, J.; Loi, M. A. Band-edge exciton fine structure and exciton recombination dynamics in single crystals of layered hybrid perovskites. *Adv. Funct. Mater.* **2020**, *30*, 1907979.

[205] Seitz, M.; Magdaleno, A. J.; Alcázar-Cano, N.; Meléndez, M.; Lubbers, T. J.; Walraven, S. W.; Pakdel, S.; Prada, E.; Delgado-Buscalioni, R.; Prins, F. Exciton diffusion in two-dimensional metal-halide perovskites. *Nat. Commun.* **2020**, *11*, 2035.

[206] Kieslich, G.; Skelton, J. M.; Armstrong, J.; Wu, Y.; Wei, F.; Svane, K. L.; Walsh, A.; Butler, K. T. Hydrogen Bonding versus Entropy: Revealing the Underlying Thermodynamics of the Hybrid Organic-Inorganic Perovskite $[CH_3NH_3]PbBr_3$. *Chem. Mater.* **2018**,

[207] Altorfer, F.; Buhrer, W.; Anderson, I.; Scharpf, O.; Bill, H.; Carron, P. L. Fast ionic diffusion in Li_2S investigated by quasielastic neutron scattering. *J. Phys. Condens. Matter* **1994**, *6*, 9937–9947.

[208] Haus, J. W.; Kehr, K. W. Random Walk Model With Correlated Jumps: Self-Correlation Function And Frequency-Dependent Diffusion Coefficient. *J. Phys. Chem. Solids* **1979**, *40*, 1019–1025.

[209] Nedumkandathil, R.; Jaworski, A.; Grins, J.; Bernin, D.; Karlsson, M.; Eklöf-Österberg, C.; Neagu, A.; Tai, C. W.; Pell, A. J.; Häussermann, U. Hydride Reduction of $BaTiO_3$ – Oxyhydride Versus O Vacancy Formation. *ACS Omega* **2018**, *3*, 11426–11438.

[210] Lavén, R.; Moraes, P. I. R.; Sannemo Targama, M.; Karlsson, M.; Leitão, A. A.; Brant Carvalho, P. H. B.; Parker, S. F.; Häussermann, U.; Vekilova, O. Y. Vibrational properties of $SrVO_2H$ with large spin-phonon coupling. *Phys. Rev. Materials* **2022**, *6*, 024409.

[211] García-Flores, A. F.; Moreira, A. F. L.; Kaneko, U. F.; Ardito, F. M.; Terashita, H.; Orlando, M. T. D.; Gopalakrishnan, J.; Ramesha, K.; Granado, E. Spin-Electron-Phonon Excitation in Re-based Half-Metallic Double Perovskites. *Phys. Rev. Lett.* **2012**, *108*, 177202.

[212] Fennie, C. J.; Rabe, K. M. Magnetically Induced Phonon Anisotropy in $ZnCr_2O_4$ from First Principles. *Phys. Rev. Lett.* **2006**, *96*, 205505.

[213] Lee, J. H.; Rabe, K. M. Large spin-phonon coupling and magnetically induced phonon anisotropy in $SrMO_3$ perovskites (M=V,Cr,Mn,Fe,Co). *Phys. Rev. B* **2011**, *84*, 1–6.

[214] Kant, C.; Schmidt, M.; Wang, Z.; Mayr, F.; Tsurkan, V.; Deisenhofer, J.; Loidl, A. Universal Exchange-Driven Phonon Splitting in Antiferromagnets. *Phys. Rev. Lett.* **2012**, *108*, 177203.

[215] Massidda, S.; Posternak, M.; Baldereschi, A.; Resta, R. Noncubic Behavior of Antiferromagnetic Transition-Metal Monoxides with the Rocksalt Structure. *Phys. Rev. Lett.* **1999**, *82*, 430–433.

[216] Toulouse, C.; Martin, C.; Measson, M. A.; Gallais, Y.; Sacuto, A.; Cazayous, M. Magnetic transitions in $CaMn_7O_{12}$: Raman observation of spin-phonon couplings. *Phys. Rev. B* **2019**, *99*, 1–6.

[217] Baltensperger, W.; Helman, J. S. Influence of magnetic order in insulators on the optical phonon frequency. *Helv. Phys. Acta* **1968**, *41*, 668–673.

[218] Hemberger, J.; Rudolf, T.; Krug von Nidda, H.-A.; Mayr, F.; Pimenov, A.; Tsurkan, V.; Loidl, A. Spin-Driven Phonon Splitting in Bond-Frustrated $ZnCr_2S_4$. *Phys. Rev. Lett.* **2006**, *97*, 087204.

[219] Hsu, H. C.; Chou, F. C.; Koyama, K.; Watanabe, K.; Liu, H. L. Spin-phonon coupling in antiferromagnetic $Bi_2Sr_2CoO_{6+\delta}$: An infrared reflectance study. *Phys. Rev. B* **2009**, *79*, 155109.

[220] Araújo, B.; Arévalo-López, A.; Santos, C.; Attfield, J. P.; Paschoal, C.; Ayala, A. Spin-phonon coupling in the incommensurate magnetic ordered phase of orthorhombic $TmMnO_3$. *J. Phys. Chem. Solids* **2021**, *154*, 110044.

[221] Mahana, S.; Rakshit, B.; Basu, R.; Dhara, S.; Joseph, B.; Manju, U.; Mahanti, S. D.; Topwal, D. Local inversion symmetry breaking and spin-phonon coupling in the perovskite $GdCrO_3$. *Phys. Rev. B* **2017**, *96*, 104106.

[222] Rudolf, T.; Kant, C.; Mayr, F.; Loidl, A. Magnetic-order induced phonon splitting in MnO from far-infrared spectroscopy. *Phys. Rev. B* **2008**, *77*, 024421.

[223] Aytan, E.; Debnath, B.; Kargar, F.; Barlas, Y.; Lacerda, M.; Li, J.; Lake, R.; Shi, J.; Balandin, A. Spin-phonon coupling in antiferromagnetic nickel oxide. *Appl. Phys. Lett.* **2017**, *111*, 252402.

[224] Kamba, S.; Goian, V.; Skoromets, V.; Hejtmánek, J.; Bovtun, V.; Kempa, M.; Borodavka, F.; Vaněk, P.; Belik, A. A.; Lee, J. H.; Pacherová, O.; Rabe, K. M. Strong spin-phonon coupling in infrared and Raman spectra of $SrMnO_3$. *Phys. Rev. B* **2014**, *89*, 1–7.

[225] Chen, X. K.; Irwin, J. C.; Franck, J. P. Evidence for a strong spin-phonon interaction in cupric oxide. *Phys. Rev. B* **1995**, *52*, R13130–R13133.

[226] Calder, S.; Lee, J. H.; Stone, M. B.; Lumsden, M. D.; Lang, J. C.; Feygenson, M.; Zhao, Z.; Yan, J. Q.; Shi, Y. G.; Sun, Y. S.; Tsujimoto, Y.; Yamaura, K.; Christianson, A. D. Enhanced spin-phonon-electronic coupling in a 5d oxide. *Nat. Commun.* **2015**, *6*, 1–6.

[227] Jin, L.; Hayward, M. A. Hole and Electron Doping of the 4d Transition-Metal Oxyhydride $LaSr_3NiRuO_4H_4$. *Angew. Chemie - Int. Ed.* **2020**, *132*, 2092–2095.

[228] OSIRIS. https://www.isis.stfc.ac.uk/Pages/osiris.aspx, Accessed: 2020-05-12.

[229] Karlsson et al., M. Mechanism of hydride-ion mobility in a novel oxide-hydride, STFC ISIS Neutron and Muon Source. 2019; doi.org/10.5286/ISIS.E.RB1920398.

[230] Fjellvåg, Ø. S.; Armstrong, J.; Vajeeston, P.; Sjåstad, A. O. New Insights into Hydride Bonding, Dynamics, and Migration in La_2LiHO_3 Oxyhydride. *J. Phys. Chem. Lett.* **2018**, *9*, 353–358.

[231] Chung, I.; Song, J.-H.; Im, J.; Androulakis, J.; Malliakas, C. D.; Li, H.; Freeman, A. J.; Kenney, J. T.; Kanatzidis, M. G. $CsSnI_3$: Semiconductor or Metal? High Electrical Conductivity and Strong Near-Infrared Photoluminescence from a Single Material. High Hole Mobility and Phase-Transitions. *J. Am. Chem. Soc.* **2012**, *134*, 8579–8587.

[232] Comin, R.; Crawford, M. K.; Said, A. H.; Herron, N.; Guise, W. E.; Wang, X.; Whitfield, P. S.; Jain, A.; Gong, X.; McGaughey, A. J. H.; Sargent, E. H. Lattice dynamics and the nature of structural transitions in organolead halide perovskites. *Phys. Rev. B* **2016**, *94*, 094301.

[233] Guo, H.; Jaworski, A.; Ma, Z.; Slabon, A.; Bacsik, Z.; Nedumkandathil, R.; Häussermann, U. Trapping of different stages of $BaTiO_3$ reduction with LiH. *RSC Adv.* **2020**, *10*, 35356–35365.

[234] Bang, J.; Matsuishi, S.; Hiraka, H.; Fujisaki, F.; Otomo, T.; Maki, S.; Yamaura, J. I.; Kumai, R.; Murakami, Y.; Hosono, H. Hydrogen ordering and new polymorph of layered perovskite oxyhydrides: $Sr_2VO_{4-x}H_x$. *J. Am. Chem. Soc.* **2014**, *136*, 7221–7224.

[235] Marder, M. P. *Condensed Matter Physics*; John Wiley & Sons, 2010.

[236] Jena, A. K.; Kulkarni, A.; Miyasaka, T. Halide Perovskite Photovoltaics: Background, Status, and Future Prospects. *Chem. Rev.* **2019**, *119*, 3036–3103.